A STUDY OF PROGRESSIVE DAMAGE DETECTION IN THIN-WALLED COMPOSITE STRUCTURES USING AN EMBEDDED FIBER BRAGG GRATING – ACOUSTIC EMISSION HYBRID SYSTEM

MOHD HAFIZI BIN ZOHARI

MAHADZIR BIN ISHAK @ MUHAMMAD

NURAZIMA BINTI ISMAIL

LIM KOK SING

JANUAR PARLAUNGAN SIREGAR

SAIFUL ANWAR BIN CHE GHANI

RESEARCH VOTE NO:

RDU160136

Faculty of Mechanical Engineering

Universiti Malaysia Pahang

AUGUST 2019

ACKNOWLEDGEMENTS

"All roads that lead to success have to pass through hard work boulevard at some point", a self-encouraging and motivational quote by Eric Thomas that has always thrilled me, and filled me with enthusiasm in completing this research study, even though it was full of various worrying and uncertain matter. The great success of this research study is based on a great number of helping hands of whom I would like to express my sincere acknowledgement and appreciation deep from my heart.

ABSTRACT

Fiber Reinforced Polymer (FRP) composites are widely used in critical engineering applications due to the advantage of higher specific strength and stiffness compared to other conventional materials. However, in FRP composites, unexpected damages can develop and propagate slowly from inside the composite layers (e.g. matrix cracks, delamination and matrix-fibre debonding). Therefore, there is a significant need of an embedded monitoring system for providing continuous real-time information on the progressive damages in composite structures under critical loading. The project is intended to quantify such damage from static; and dynamic measurements of acoustic emission from fiber Bragg grating (FBG) sensor network on a model of thin walled structure. This research aims to investigate the capability of FBG system in acquiring dynamic signal up to kilohertz range therefore sufficient to be research aims to investigate the capability of FBG system in acquiring dynamic signal up to kilohertz range therefore sufficient to be used as an acoustic emission sensor. In this work, the FBG-FPI (Fiber Bragg Brating with Fabry–Pérot Interferometer) has been applied for the FBG dynamic system, for sufficient sensitivity and less noises. Finally, a signal processing algorithm was developed to locate flaws / damages and also identify the condition of a thin composite structures. The algorithm was named as cross-correlation with linear source location technique (CC-LSL) impact detection algorithm.

TABLE OF CONTENT

LIST OF TABLES

LIST OF FIGURES

CHAPTER 1

INTRODUCTION

1.1 Introduction

The Fiber Bragg Grating (FBG) sensor is one of the most suitable sensors for the SHM of aircraft FRP structures (Di Sante, 2015). The FBG sensors can be embedded in FRP composites during the manufacture of the composite part with no effect on the strength of the part as the sensor is diminutive. This sensor is also suitable for networking because it has a narrow-band response with a wide wavelength operating range, hence can be highly multiplexed. This non-conductive sensor can also operate in electromagnetically noisy environments without any interference.

The FBG sensor is made up of glass which is more environmentally stable and with a long life time compared with FRP composites. Because of its low transmission loss, sensor signals can be monitored from longer distances making the FBG sensor suitable for remote sensing. Its capability to detect stress gradients along its length can be used to identify the stress variations in FRP composites by means of chirp in the reflected spectra of the FBG sensor. This phenomenon can be used to detect damage in the composite structures. But, it has been reported that the chirp of the FBG spectrum is not limited to stress concentrations caused by damage (Y. Wang et al., 2008). There are other causes of chirp and it is necessary to eliminate such effects to identify damage origin accurately. Using only distortion or chirp to the FBG response in order to identify damage in composites, is questionable. For reliable operation of the SHM system, it is desirable to have at least two independent techniques which can be used to verify each result.

Nowadays, Acoustic Emission (AE) becomes one of the most popular non-destructive (NDT) techniques. This technique became popular today, owing to its ability to reveal in advance any impending failure of composite structures, but more than that, it

be used for real-time monitoring. AE is also well known as highly sensitive technique for detection of various types of damage using a small number of sensors, thus is very attractive for SHM. In composites, researchers were interested to study the AE parameters that can be correlated to composite's early failure such as fibre breakage, fibre-matrix debonding, delamination, matrix cracking (Zohari et al., 2013) and etc.

Recently, by using modal acoustic emission (recent AE analysis approach) Scholey et al (Scholey et al., 2010) have found that matrix cracking and delamination growth can be distinguished by the mode of wave propagation; and S_0 (symmetric) and A_0 (asymmetric) mode, respectively. By combining all the information from previous studies, a pattern recognition technique can be used to well correlate AE data with any of composites failure (Gutkin et al., 2011). On the other hand, the use of FBG sensors for dynamic sensing is relatively new and several numbers of research works were published during the last decade. This approach has been shown to work in many applications, such as composites health monitoring (Fernando et al., 2017; Z. M. Hafizi et al., 2015) and for Non-destructive evaluation (NDE) purpose (Wild et al., 2007; Zohari et al., 2015).

Implementing two completely different systems for SHM of composite structure makes the system complicated. It is difficult to have two types of sensor networks in the same structure. Therefore, it is desirable to use the same sensor network for SHM with two independent techniques. The excellent sensitivity of FBG sensors make it possible to use them as dynamic acoustic sensors (Z. Hafizi et al., 2015) while sensing the static strain distribution (gradient) (Fedorov et al., 2015). In this research study the use of FBG sensors for damage detection using strain gradient and AE is explored.

1.2   FBG sensors for defect detection and the AE applications

Fibre Bragg Gratings (FBGs) are formed by constructing periodic changes in the index of refraction in the core of a single mode optical fibre. This periodic change in index of refraction is typically created by exposing the fibre core to an intense interference pattern of UV radiation. The FBG sensors have been using for the SHM of composite materials efficiently for more than two decades. Recent advances in FBG sensor technologies have provided great opportunities to develop more sophisticated in-situ SHM systems. There have been a large number of research efforts on the health monitoring of composite structures using FBG sensors.

The ability to embed inside FRP material in between different layers provides the closer look upon defects. The attractive properties such as small size, immunity to electromagnetic fields, and multiplexing ability are some of the advantages of FBG sensors. The lifetime of an FBG sensor is well above the lifetime of the FRP structures and so it also allows the measuring of multiple parameters such as load/strain, AE, vibration and temperature.

The FBG sensors are fabricated in the core region of specially fabricated single mode low-loss germanium doped silicate optical fibers. The grating is the laser-inscribed region which has a periodically varying refractive index. This region reflects only a narrow band of light corresponding to the Bragg wavelength λ_B (further information in the next chapters). In the layered FRP composite structure, it is difficult to use surface or external sensors to monitor inside damage effectively. The ability to embed FBG sensors inside FRP sandwich panels between different layers provides a closer look at defects such as delaminations and cracks. The FBG sensor is sensitive to stress gradients along the gauge length of the sensor and displays it as a chirp (or distortion) from its response spectra.

The majority of research works on FBG sensors in SHM of composite structures have focused on the investigation of the spectrum of FBG sensors embedded in the vicinity of damage. Observations of the distorted sensor spectrum, due to stress concentrations caused by delaminations and cracks, have been used to estimate the damage conditions. Many researchers have investigated purposely damaged axially loaded specimens, and the changes of FBG spectra were attributed to the damage and successfully identified the damage. In real life situations, the applied loads are not limited to uni-axial loads and hence the performance of FBGs in multi-axial loading situation need to be investigated for a complete understanding of damage status. The FBG spectral response is significantly complicated under multi-axial loading conditions. The distortion of FBG spectra not only depends on the consequences of accumulated damage, but also the loading types. Recently, it has been shown that embedding FBGs in between non parallel fiber layers and the application of torque has caused substantial distortions to the FBG spectra (Fernando et al., 2017). The pressure load applied on the FBG sensor by the outer glass fiber layers, can distort the circular-cross section of FBG to an oval shape. Since the FBG sensor is placed in between non-parallel fiber layers, micro-bending of the

sensor is also possible. Due to the large diameter of the FBG sensor, compared to the diameter of glass fibers, there are additional transverse forces on the FBG sensors which lead to a micro bending. Both these effects will lead to a variation of the refractive index of the core material, causing the distorted spectrum.

From the observations, it is clear that the multiple causes lead to distortion to the FBG response spectra. Most of the effects, such as embedment of FBG sensor only in between parallel fiber laminates, parallel to the fiber orientation, and multi-directional loading on FBG sensor, cannot be eliminated in advanced aerospace applications. In order to identify damage from the distortions to the FBG response spectra, the individual effect from each effect needs to be identified and eliminated. To identify the pure effects from the damage, distinguished from the other effects, extensive computational power is required for post-processing of the spectral data.

As a consequence, in the laboratory environment it is possible to discuss and interrelate the FBG response spectra with the damage by creating artificial damage and observing spectrum of an FBG which is embedded closer to the damage location (G C. Kahandawa et al., 2012; Gayan C Kahandawa et al., 2010). But, in the real application, if such spectrum is observed, it is very difficult to interpret the spectrum in order to identify the damage. The one directional accuracy, which is if there is a known damage in the structure, response spectra (distortion) of embedded FBG can be explained, but if distorted response spectrum is observed, it is not possible to identify it as a presence of damage. This incongruity disappointed and discouraged some SHM researchers.

There was a huge demand for an out-of-the-box approach to overcome the discrepancy. To overcome the complications mentioned above, a hybrid approach for damage detection can be used. By using the sensitivity of FBG sensors to AE, it is possible to use same FBG sensor for detection of the AE signal. The AE signal has been used by many researchers to detect damagers successfully. The AE method can be called a s a passive ultrasonic method, where the ultrasonic wave; which can be continuous or burst signals, released from any source (e.g. flaws, cracks) travel in medium of solid materials (e.g. concrete, metals, composites) and can be easily captured by the AE sensory systems. The AE signal is generally found in the frequency range of 20 kHz to 2000 kHz. The AE transducer (usually piezoelectric) is like a human ear; where it collects all acoustic data from the surroundings; as example, the acoustic signals from a material's

flaws. All the information then will be transformed into electrical signals and submitted to the brain (computer) for interpretation.

In the early years of Acoustic Emission (AE) implementation, it was common for researchers to obtain a large amount of data and use the statistical figures to explain the material failures qualitatively. Many studies had successfully predicted material properties and classified the failure mechanisms of composite materials by analyzing AE signals (Eaton et al., 2012). In several researches, the related features of AE signals were extracted and matched with the failure mechanism accordingly, instead of only qualitatively looking at the statistical data (Trojanová et al., 2011) [15]. In this case, an artificial neural network was applied to predict the possible occurrence of the next failure with new AE data. The results were promising; however, the data clustering or 'features matching' between the AE signals and failure mechanisms still need to be improved to get an accurate prediction. It is true for the case of multiple types of failures such as in the mechanical testing of composite materials; e.g. static tensile testing, double cantilever and compression test. For feature matching purposes, some researchers defined the range of some AE parameters such as amplitude or peak frequency that can be referred to the occurrence of a particular failure or failure modes.

1.3   Problem statement

With the complex failure modes of FRP composites, SHM becomes vital. Impact, vibration, and loading can cause damage to the FRP composite structures, such as delamination and matrix cracking. Moreover, the internal material damage can be invisible to the human eye, making inspection of the structures for damage and clear insight into the structural integrity difficult using currently available evaluation methods.

The SHM system developed to monitor aircraft and space structures must be capable of identifying multiple failure criteria of FRP composites (Di Sante, 2015). Since the behavior of composites is anisotropic, multiple numbers of sensors must be in service to monitor these structures under multi-directional complex loading conditions. The layered structure of the composites makes it difficult to predict the structural behavior by using surface mounted sensors only.

To address this issue embedded sensors must be used and they must possess a sufficiently long lifespan as it is not possible to replace embedded sensors after fabrication of the parts. At present, the use of piezoelectric sensors (PZT) for SHM couldn't solve the problem since it cannot offer a sufficient capability to be embedded inside the composite layers, due to its physical size. Therefore, PZT is only suitable for surface mounted application. The introduction of FBG sensor will solve the issue, however an extensive study need to be done to characterize the signals from FBG sensor and correlate with the growth of internal damages in thin-walled composite structures.

1.4   Objectives of the research

In general, the project aims to characterize the optical signal from embedded FBG sensors and the electrical signals from FBG-AE system; and correlate with the progressive damage in thin walled composite structures. In details;

i.   To investigate the matrix cracking and delamination growth inside a thin-walled composite structure.

ii.   To correlate the progressive damages progress with the signals from the FBG spectra and AE signal parameters.

iii.   To construct a signal processing algorithm for monitoring damages/flaws inside thin walled composite structures combined with appropriate FBG sensor network.

1.5   Significant/Contribution of Study

The outcome of the project can be applied in the structural health monitoring of thin laminated composite structures, e.g. civil structures and wind turbines, whereby in line with the National Key Economics Area (NKEA). Besides, it also can be used for pipe leak monitoring in oil and gas industries whereby a long distance monitoring is necessary. Note that oil and gas is also listed in NKEA.

The developed optical-based monitoring system can improve the structural health monitoring of any infrastructures, not only during services, but also during the construction phase. With the recent issues of the catastrophic event of structures under construction (in Malaysia), the development of proper monitoring system is in a significant need.

1.6 Brief on the chapters in report

This report was arranged according to the important topics and all results from this project. In chapter 1, introduction, problem and objectives has been highlighted as above. Meanwhile, chapter 2 to chapter 6 present the main content of the project. At the end, chapter 7 will concludes all findings in this project.

1.6.1 Abstract for Chapter 2: Lamb Wave Actuation Techniques for SHM System - A Review

Lamb waves-based structural health monitoring (SHM) system has gained significant consideration because of good balance between desirable precision and versatile accessibility. This paper is specifically reviews the employed actuation techniques applied in the SHM system for diagnostic analysis using Lamb waves method. It is axiomatic that appropriate signal actuation is of vital necessity and importance for a reliable SHM system. Multimodal and dispersive characteristics of the Lamb waves are the main factors for the variety of applied techniques. Multiple Lamb modes synchronously exist, and their dispersive properties are not identical which lead to extremely superimposed signals. The scholars invented many techniques for the single mode generation in order to reduce the complication of the received responses. Generally, the applied strategies can be clustered to frequency tuning, actuator configuration and angle of incidence. The findings showed that the applied approaches were successfully generating pure mode for further analysis. All these studies have shown the evolution of Lamb waves-based SHM system for controlling and monitoring the condition of the structure.

1.6.2 Abstract for Chapter 3: FBGs Real-Time Impact Damage Monitoring System of GFRP Beam Based On CC-LSL Algorithm

Glass-fibre reinforced polymer (GFRP) composite materials truly have an undisputed dominance over conventional metallic materials. However, susceptibility to barely visible or invisible internal damage due to impact has increased the demand for these composite materials in robust real-time structural health monitoring (SHM) system since they are capable to localise the source of impact. Thus, in this paper, an in-situ FBG sensor was embedded in a GFRP beam, providing an online real-time monitoring system and with the knowledge of cross-correlation linear source location (CC-LSL) algorithm, the impact

location was capable of being determined in a split second. The consistency of cross-correlation function in providing repeatable results for all trials estimated a consistent time difference for all the impact points. The CC-LSL algorithm also revealed that the highest percentage of error was only 4.21% away from the actual hit. In the meantime, FBGs also showed good results as a dynamic strain measuring device in capturing frequency response at certain orientations compared to the AE sensor.

1.6.3 Abstract for Chapter 4: Damage Detection of the Composite Plate Using Matched Filtering of Centre of Energy

With the advantage of superior strength-to-weight ratio, fiber reinforced polymer (FRP) composites are widely used in many heavy and critical industries such as aircraft, automotive and rail transport. However, unexpected damages such as delamination can develop and slowly propagated from inside composites due to its layered structure. This phenomenon will affect the durability of the FRP structures. Therefore there is a significant need of using an embedded sensor, called as fiber Bragg grating (FBG) for structural health monitoring system (SHM) of the structures. Recently, researchers detect damage phenomenon in the composites layer by using FBG response spectra. This approach gives less detail about the pure damage since the data is a mixture with the initial condition of the FBG. Consequently, an algorithm based on the matched filtering of center of energy (MFCE) was developed to solve the above problems. This algorithm will detect flaws in the composites structure by using time of arrival indicator. Condition of the FRP composite can be evaluated quantitatively.

1.6.4 Abstract for Chapter 5: Interactions of Lamb Waves with Defects in A Thin Metallic Plate

A Lamb waves-based technique for damage detection is one of the promising diagnostic tool due to their ease of excitation and detection along with their ability to travel long distances. The dynamic finite element analysis is performed in this study in order to understand their behaviour when interacting with defects for a successful implementation of this technique in Structural Health Monitoring system. FEA analysis was implemented to simulate propagation of Lamb waves in healthy and defective aluminium plate. The sensors are placed based on the configuration of pulse-echo and pitch-catch method. It is noticed that there is an additional wave packet for the detected signals for defective plate

based on pulse-echo method whereas there is a significant delay in signal arrival for the pitch-catch method. This simulation study shows a significant feature extraction for the interactions of Lamb waves with defects. It is helpful for a good understanding before applying this technique for a real implementation.

1.6.5 Abstract for Chapter 6: Fiber Bragg Grating Based Fabry - Perot Interferometer Sensor for The Detection of Damage in Thin Aluminium Plate

Structural Health Monitoring of engineering structures become an essential measure for the prevention of catastrophic failures. This study presents a feasibility study of Fiber Bragg Grating-based Fabry-perot interferometer (FBG-FPI) sensor for damage detection on aluminum plate, in acoustic pulse-echo lamb wave technique. FBG-FPI has shown a good sensitivity for dynamic strain sensing, together with its superiority over the conventional sensor in term of immunity to electromagnetic interference and multiplexing ability. Two FBG-FPI sensors was surface attached to the plate, at several distance from piezoelectric actuator. Meanwhile, a damage slot was introduced to the plate, 15 cm from the actuator. The detection of the damage was done by analysing the time domain signals and time-frequency analysis. The Short Time Fourier Transform of the reflected signals due to damage, has indicated an additional wave packet, which was also visible in the time-domain signals, compared to intact plate. Further analysis shows that the excited additional wave packet share identical frequency with the direct wave from piezo actuator. The obtained results validate the applicability of the FBG-FPI sensor for damage detection in thin-walled metallic structure.

CHAPTER 2

LAMB WAVE ACTUATION TECHNIQUES FOR SHM SYSTEM- A REVIEW

2.1   Introduction

Damage detection has received increasing attention especially in mechanical, civil and aerospace engineering. Variation of damage detection methods have been invented throughout the years such as visual inspection, infrared thermography (Ramlogun et al., 2005), laser ultrasound (F. Chen et al., 2010), laser shearography (Gregory, 2001) and X-ray radiography (J. Zhang et al., 2002). Most of these techniques are time-consuming, expensive and disassembly of the part is required before performing the testing. The most important fact that they are not utilized for real time monitoring is the main motivation for the development of new and improved way of Nondestructive evaluation (NDE) called Structural Health Monitoring (SHM).

A typical SHM involves the utilising of sensor networks for information gathering and a database unit for data processing and decision making. (Abdo, 2014) Sensors and actuators are permanently located on the structure and this allows for continuous safety and durability evaluation. Worden, Farrar, and Manson (2007) explicitly stated the axioms of the SHM. The paper was addressed the first three level of SHM system which is detection, location and severity assessment. This note gave new researchers in the field a starting point that alleviates the need to review the vast amounts of SHM literature. Active and passive approaches are the possible strategies for SHM system. The active approach needs actuation of monitored structures and passive approach do not involve any actuation. (Staszewski et al., 2009) Among the SHM based techniques, Lamb Waves (LW) methods are promising and have been successfully employed in many application areas because of their advantages. LW were used as a means for the internal and surface

damage detection due to their special characteristics that are able to propagate throughout the entire thickness of the plate. (Alleyne et al., 1992) Thus the valuable information related with structural integrity can be extracted from the propagated waves. They also have the ability to reduce signal processing time for damage information extraction. This is because this method does not require continuous monitoring during its service compared with other methods. (Y.-H. Kim et al., 2007) Other than that, its ability to perform inspection for a large structure from limited access helps this technique to grow rapidly. (Joseph, 2011) Generally, the basic parameters that are used as an indicator for the diagnostic parameters are wave amplitude, phase, dispersion and time of flight. This is based on the basic knowledge behind LW propagation that interacts differently with different types of damages. (Jha et al., 2010) The propagating waves carry comprehensive information as they transverse through the structure. Figure 2.1 depicts the propagated waveforms measured from two different conditions.

(a)   (b)
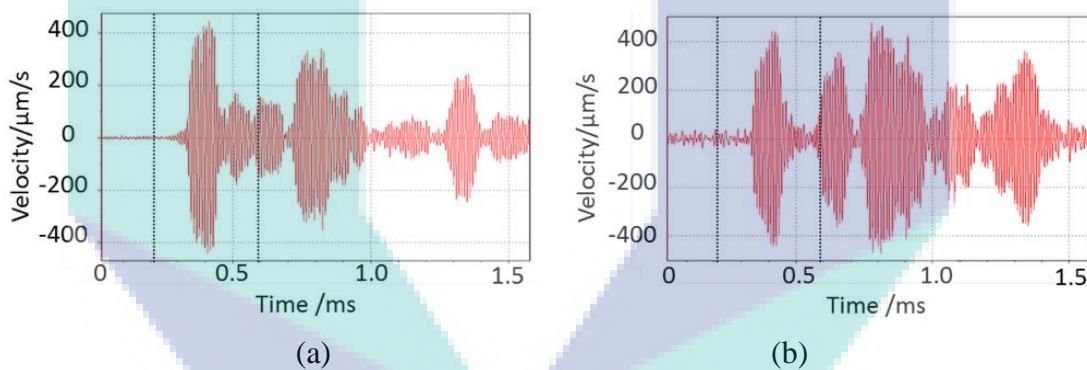
Figure 2.1   The waveforms from a: a) healthy panel; b) disbonded panel.

Source: Marks et al. (2016)

However, the multimode and dispersive nature of the measured LW leads to difficulty during data analyzing and interpretation. This phenomenon gives a major challenge when employing LW for SHM which affect the signal's integrity. Many researchers have intensively developing strategies to solve the dispersive behavior problem to ensure that the acquired waveform is reliable for the SHM system by providing the correct data to be analyzed. Thus, the intention of this paper is to summarize the applied actuation and signal processing method in a proper way for a good understanding of other researchers. It is strongly believed that this article will help and guide the other researchers to design their LW-based SHM system set up by deciding

which method is suitable and related to their case studies. This paper may be a starting point that alleviates the need to review the vast amounts of literature in this field.

2.2   Theory of Lamb Waves

A Horace Lamb (Horace Lamb, 1917) first described the fundamental theory of LW and other alternatives references of the fundamentals related to LW can be found in textbooks by Royer et al. (2000), Joseph L. Rose (2014), and Viktorov (1967). LW are elastic waves which exist in thin plate structures with free boundaries. Their motion of propagation can be symmetrical or anti-symmetrical with respect to the neutral axis of the plate as depicted in Figure 2.2. Symmetric modes show the longitudinal motion in the centerline and have identical strains at both the top and bottom surfaces. Meanwhile, anti-symmetric modes exhibit a transverse motion in the middle plane and have opposite strains at the top and bottom.

Propagation direction

(a)   (b)
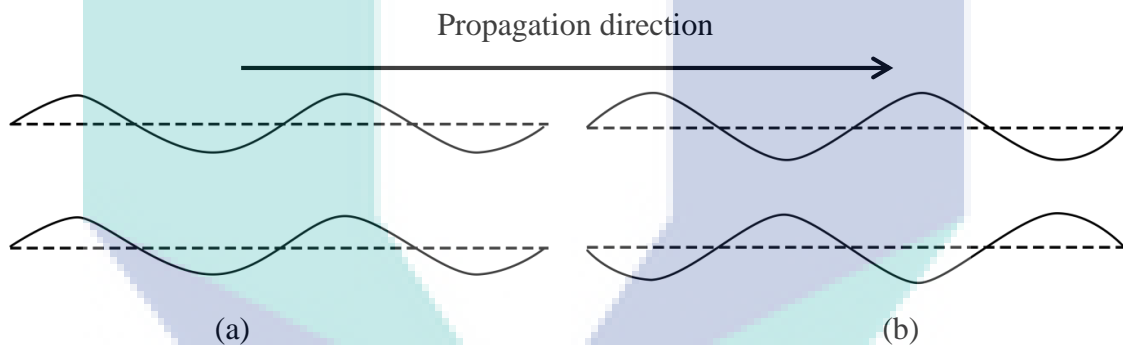
Figure 2.2   Types of LW modes. (a) Anti-symmetric; (b) symmetric LW.

Helmholtz decomposition was implemented to solve the LW equation in a thin isotropic medium.(Joseph L. Rose, 2014) 3D-displacement vectors are decomposed into multiple curl-free and divergence-free vector components which can be described using two equations. The curl-free vector component can be described as the longitudinal wave whereas divergence-free vector component is a transverse wave. The combination of longitudinal and transverse waves contributes to two distinct waves, as mentioned earlier which are symmetric and the anti-symmetric LW and can be described using the following equations:

$$\frac{\tan(qh)}{\tan(ph)} = -\frac{4k^2 qp}{\left(k^2 - q^2\right)^2} \tag{1}$$

$$\frac{\tan(qh)}{\tan(ph)} = -\frac{\left(k^2 - q^2\right)^2}{4k^2 qp} \tag{2}$$

where $\quad p^2 = \dfrac{\omega^2}{c_L^2} - k^2 \qquad\qquad q^2 = \dfrac{\omega^2}{c_T^2} - k^2 \qquad\qquad k = \dfrac{\omega}{c_p}$

where k, h, c_L, c_T, c_p and ω are the wavenumber, plate thickness, velocities of longitudinal and transverse modes, phase velocity and wave circular frequency, respectively. Equations (1) and (2) clearly indicate that the propagation velocity is dependent on its frequency values. This situation implies that LW are dispersive, regardless of modes. (Zhongqing Su et al., 2006)

2.3   Dispersion of the Lamb Waves

Dispersion is a phenomenon in which the group or phase velocities vary with the product of frequency and plate thickness. This characteristic leads to the spreading of wave-packet in space and time as it transverses through a structure. This property affects the spatial and temporal resolutions and this can potentially compromise the receiver detectability. (Wilcox et al., 2001) As an example, a plate structure was actuated at a center frequency of 300 kHz as illustrated in Figure 2.3. The result of frequency domain analysis using the measured LW signal will display the peak occurring at 293kHz for symmetric and 332kHz for an anti-symmetric mode. This obviously indicates the dispersion phenomenon since the measured center frequency is not identical to the original center frequency. (Y.-H. Kim et al., 2007) The shift in the center frequency is a proof of wave dispersion.

Dispersion curves are used to predict and describe the relationship between phase or group velocity against frequency and thickness product. Figure 2.4 displays the example of the dispersion curve of the aluminum plate. There are two important information can be extracted from the dispersion curve. First is the LW dispersion information, showed by the steepness slope of the curve. Higher dispersion indicated by a larger slope of the curves. Second is the number of existing mode at a given *fd* value. It

was specified by the number of curves that exist at that given *fd* value. Tendency of LW to distort is very large as they propagate in high dispersive region, and many modes of LW are detected in the region with many curves. (Hayashi et al., 2003) Both information is very crucial for the LW-based SHM system. Researchers are using this information to devise their experimental set up in order to minimize the number of generated modes for the ease of post-processing analysis. Thus, it is proven that the dispersive behavior of the LW makes the signal interpretation difficult and complicated with existing of many modes at same given excitation frequency.
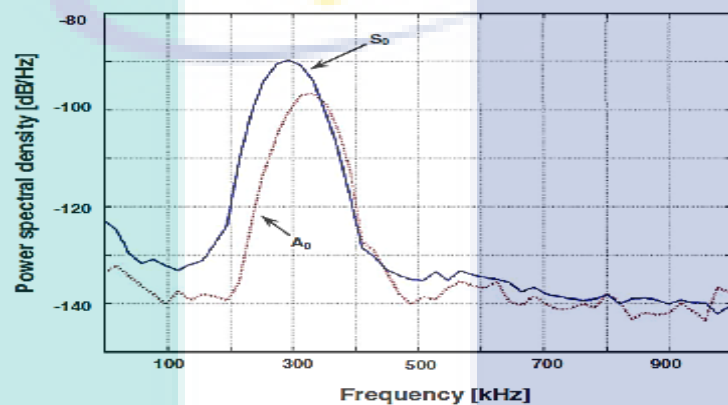
Figure 2.3   Frequency domain features of the fundamental symmetric (S_o) and anti-symmetric (A_o) at original excitation frequency of 300 kHz.

Source: Y.-H. Kim et al. (2007)
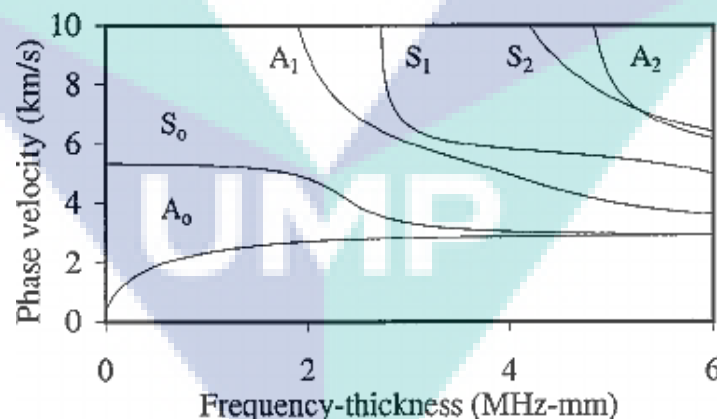
Figure 2.4   The dispersion curve of the aluminum.

Source: H Díaz Valdés et al. (2002)

2.4   Lamb waves-based SHM system

As mentioned earlier, the multimodal and dispersive nature of the LW affects the signal interpretation for SHM system. From this perspective, the authors extracted the applied

LW methods information from past researchers and summarized the details for beginner references. The complexity of the signal contributes to the serious difficulties during signal interpretations. Thus, different researchers performed different methods based on applicability and suitability of their applications. The next section explains in details about the approaches that have been applied by the researchers in SHM system using LW approach.

2.5   Generation of single Lamb mode

LW can be efficiently activated by various methods for the in situ SHM system. Theoretically, any excitation frequency generates a minimum of two modes, which lead to the complexity of the received responses. Thus, researcher invented and developed variety of techniques in order to generate pure modes for a reliable and successful SHM system. This section is divided into several subsections, which explain in details about the excitation approaches for the pure mode generation.

2.6   Mode tuning

For this kind of approach, several parameters are taken into consideration to generate the selectively desirable modes. One of them is actuation parameters including frequency, number of cycles, pulse shape and amplitude to be sent during each pulse period. (Seth et al., 2002) Among the stated parameters, frequency or center frequency contributes most to the actuation of the desired modes which is based on fact that the behavior of the LW propagation through a solid medium is determined by the frequency-thickness product (Joseph L. Rose, 2014). Most of the researchers called this procedure as the mode tuning method which is aim to identify the frequency points where single mode LW can be tuned into. The actuator is placed on top surface of the structure and the mode tuning process is proceeded. Generally, Giurgiutiu (2005) identified two combination factors that must be considered during the mode tuning process, i.e., wavelength tuning and amplitude tuning. Theoretically, maximum amplitude of one mode can be achieved when the transducer lengths $2a$ are an odd multiple of the half wavelength λ and is given as

$$2a = (2n-1)\frac{\lambda}{2}, n = 1,2,3.....$$ (3)

Minimum amplitudes can be achieved when the lengths are an even multiple of the wavelengths. This theory had been proved experimentally in (Giurgiutiu, 2014) and (Xu et al., 2007). A tone-burst excitation signal was swept at a certain range of interested frequency to perform the mode tuning process. The frequency point that produces highest amplitude mode was then used as the excitation frequency for generation of pure LW mode.

On the other hand, in a simple way, the researcher referred to the theoretical dispersion curve to determine the appropriate frequency point for the single mode generation. Thus, a prior knowledge of the dispersion curve is required before performing the mode tuning. The selected center frequency is based on the minimum number of modes that exist at that given excitation frequency and in the less dispersive frequency region. (Hoon et al., 2004)

Santoni et al. (2007) derived the LW mode tuning curves analytically. The curves indicate the frequencies that exist at which the A_0 mode or the S_0 mode can be either suppressed or enhanced. Verification of these tuning curves were extensively performed using experimental tests and the obtained results showed an agreement with each other. The findings were then implemented for monitoring the large area from a single location using tuned S_0 mode and the concept of PWAS phased array.

On the other hand, Zhai et al. (2010) have established the excitation equation for choosing a reasonable operating point (excitation frequency) to generate a single mode of electromagnetic ultrasonic LW using electromagnetic acoustic transducers (EMAT). The EMAT consists of the coil, the permanent magnet or electromagnet and the specimen as depicted in Figure 2.5. The finding stated that the excitation of Lamb waves based on EMATs is determined by the meander-line coil spacing interval L, the exciting-current frequency f, and the thickness of specimen d for single mode generation. Z. Guo et al. (1997) also utilizes EMAT for single mode generation. The L size was selected to be twice the interested mode wavelength λ. The authors were successfully generated the pure A_0 mode to study its interaction with the crack-like notch. The successfully single mode generation using EMAT also can be found in (Murayama et al., 2002; SongSong et al., 2010).

On the other hand, Monkhouse et al. (1997) designed a flexible interdigital polyvinylidene fluoride (PVDF) transducers for the generation of the selected LW modes. The finding shows that the pure modes can be excited when the designed transducer was operating at fine-tuning frequency. The basic principle for the construction of this PVDF is based on the electrode finger spacing as illustrated in Figure 2.6. Specific wavelength can be excited by adjusting the electrode finger spacing.

J. Li et al. (2001) built a multi-channel time-delay system in order to conduct the mode tuning procedure to solve the problems related with the conventional transducer array for the generation of individual wave modes. The schematic diagram of the built system is shown in Figure 2.7. In principle, the wavelength of the interested modes should be identical to the element spacing and all elements should work in phase in order to perform frequency tuning. Automatic time delay algorithm was an added value for the real practice implementations.

T. Liu et al. (2002) developed a numerical simulation tool to investigate the acoustic wave field excited by piezoceramic transducer arrays or IDT in composite plates as shown in Figure 2.8. The developed tool was capable of performing the mode isolation based on certain factors such as the apodisation, number of array elements, thickness and width of the elements. The thickness and materials of possible backings should also be considered. For this purpose, the frequency tuning was applied by choosing half wavelength of the targeted mode as the spatial distance between two adjacent elements at the centre frequency of the excitation pulse. On the other hand, Schmidt et al. (2013) designed an IDT with apodisation as shown in Figure 2.9 to enhance A_0 mode and attenuate S_0 mode dedicated for the CFRP laminates. Modification of the frequency function response was used to determine the particular frequency range that generated the lowest order of symmetric and anti-symmetric modes. The study by Michał et al. (2013) and Mańka et al. (2013) also reported about the single mode excitation using IDT.
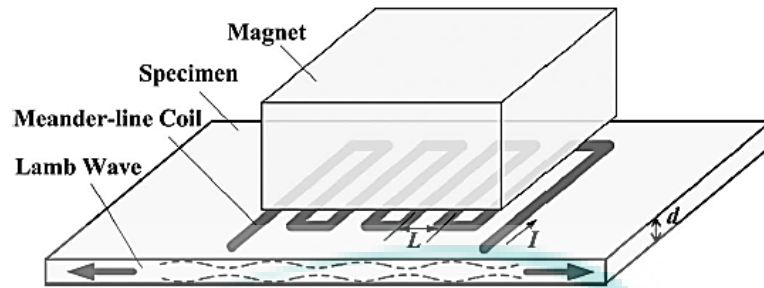
Figure 2.5   LW generation using EMAT.

Source: Zhai et al. (2010)
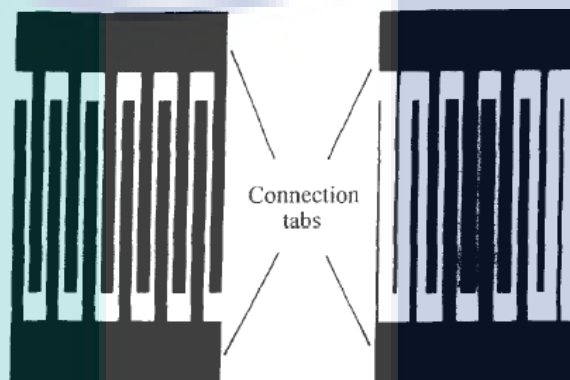
Figure 2.6   Finger electrode pattern. (a) plain; (b) apodised.

Source: Monkhouse et al. (1997)
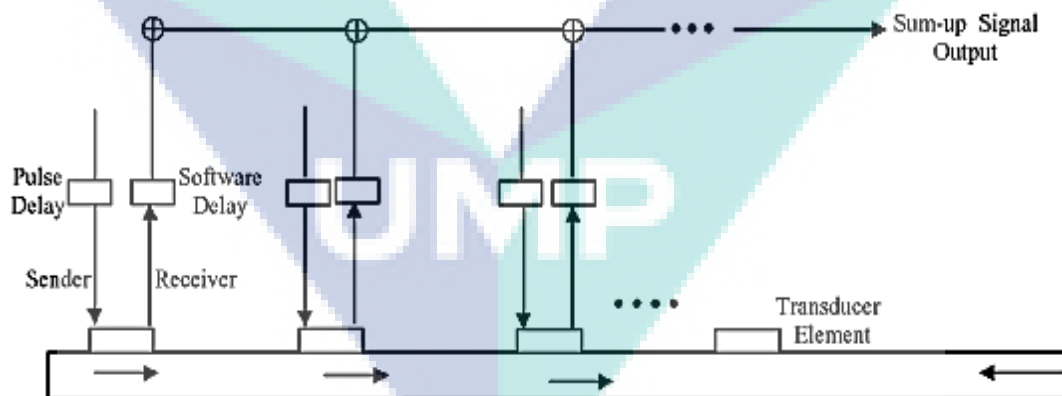
Figure 2.7   A multi-channel time-delay system built by J. Li et al. (2001)

Source: J. Li et al. (2001)
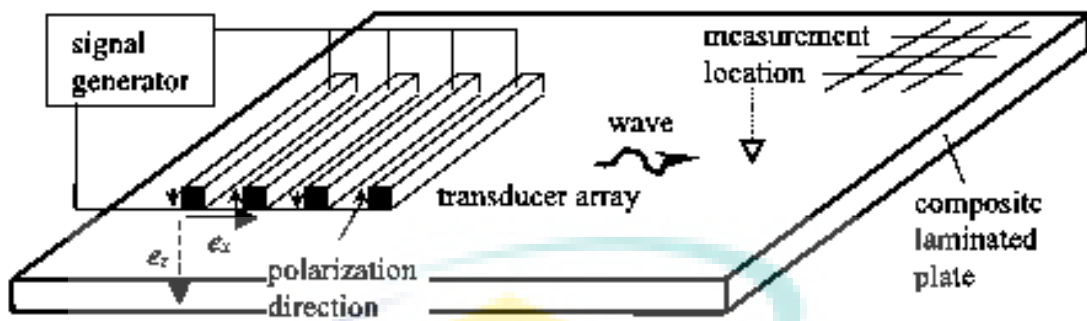
Figure 2.8   Schematic diagram of IDT surface mounted to a composites plate for the single mode generation

Source: T. Liu et al. (2002)

Many other reports (Hiroshi et al., 2004; Hoon et al., 2004; Moulin et al., 1997; Murat, 2015; J. L. Rose et al., 1997; Tsuda, 2006; X. Wang et al., 2008; Yu et al., 2008) can be referred for the individual incident modes excitation utilizing the mode tuning method using LW method.
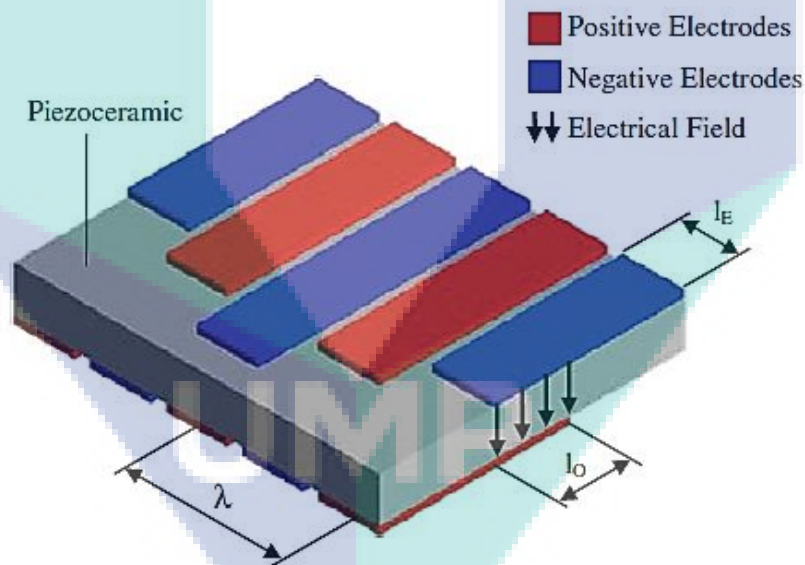
Figure 2.9   IDT with apodization designed by Schmidt et al. (2013) for the mode selectivity

Source: Schmidt et al. (2013)

Simulation works also gained attention from the researcher due to the costs of experimental measurement and equipment. Ahmad (2011) reported in his thesis the implementation of Semi-Analytical Finite Element (SAFE) Method to calculate the tuned frequency for isotropic and anisotropic plates.

2.7 Double side excitation

Another factor that was considered for the single-mode generation is the actuator configuration. Utilization of the double side actuation has shown its outstanding ability for pure modes generation. Symmetric and anti-symmetric modes were excited by in phase and out of phase voltages application. Two actuators were utilized to implement this phase cancellation method. Lin et al. (2001) and H.-Y. Zhang et al. (2011) have explained in detail about this principle in their reports. They performed the analytical study for the generation of the individual Lamb modes. A pair of the PZT actuators was symmetrically attached on the upper and lower surfaces (double side actuation) of a structure as shown in Figure 2.10. Meanwhile Hu et al. (2008) and Z Su et al. (2004) performed the experimental study utilising this strategy for damage detection. This kind of excitation shows a good agreement with the simulation works and it is a promising tool for damage detection. In contrast, Yoji et al. (2010) applied the double side actuation method using macrofibre composite (MFC) actuators as shown in Figure 2.11. The anti-symmetric mode was individually excited in this research for the delamination detection. The mode was converted to different modes depending on the delamination length. Other than that, S. Liu et al. (2017) employed this techniques by utilising EMAT transducer for the single mode generation. The EMAT was symmetrically mounted on the upper and lower surfaces of the aluminum for the generation of the pure anti-symmetric and symmetric.
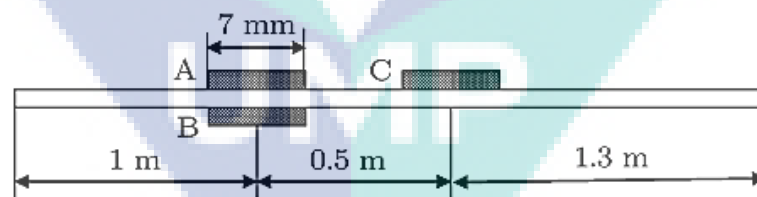
Figure 2.10   Schematic diagram of the double side actuation techniques applied by H.-Y. Zhang et al. (2011) for the analytical study verification (A and B are actuators and C is sensor).

Source: H.-Y. Zhang et al. (2011)

2.8 Opposite side excitation

On the other hand, Grondel et al. (2002) performed the excitation strategies using a pair of transducers which were surface-bonded opposite to each other (opposite side actuation)

to generate a single-LW mode. The method is known as dual-element transducer setup as shown in Figure 2.12. In this method, two actuators were placed opposite of each other at an optimised distance of 17 mm and were excited in-phase to dominantly generate the desired A_0 modes. The distance between two PZT elements is the main contributory aspect for the excitation of modes of interest. Y.-H. Kim et al. (2007) also demonstrated the same approach for the symmetric and anti-symmetric modes separation in the damage assessment of layered composites.

Despite the promising result from the method in the single mode generation, the requirements for such an experimental system should be taken into consideration. The system demands double transducer numbers and higher hardware requirement if compared with the single side excitation method. (H.-Y. Zhang et al., 2011)
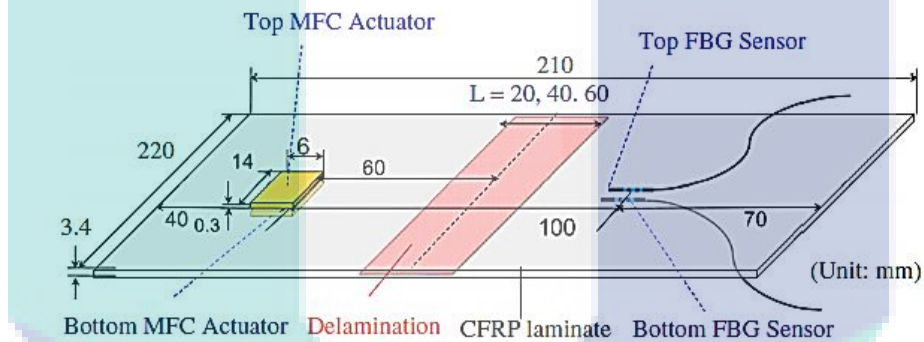
Figure 2.11   Double side actuation method applied by Yoji et al. (2010) for the delamination detection of the CFRP composite

Source: Yoji et al. (2010)
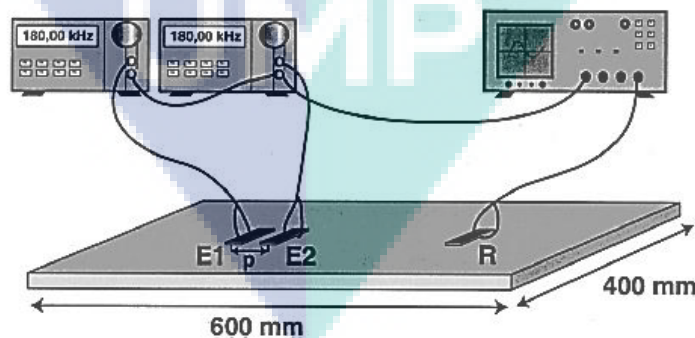
Figure 2.12   Dual-element transducer (E1 and E2) setup by Grondel et al. (2002)

Source: Grondel et al. (2002)

33

S. Liu et al. (2017) stimulated single-mode LW and eliminated the extra modes by employing the double EMATs. Their simulation findings can be used as a theoretical basis for the double transducer excitation system design.

2.9   Angled transducer

Another practice that is applied by researchers to generate pure Lamb mode is by conducting the transducer angle adjustment. The principle used in this technique is based on Snell's law. Depending on the elasticity and acoustic properties of the medium, the desired phase velocity of the excited Lamb mode at a specific frequency can be controlled by adjusting the incident angle. K. S. Tan et al. (1995), N. Guo et al. (1993a) and N. Guo et al. (1993b) adjusted the angle probe to excite the selected mode for the delamination detection on the carbon/epoxy prepreg laminates. The general experimental setup for this type of techniques is illustrated in Figure 2.13. It is noticed from the finding that the adjustment of the actuator angle is a useful method for single mode generation. This work was proved by Alleyne et al. (1992), Khalili et al. (2016) and Jayaraman et al. (2009). According to Z Su et al. (2004) angled transducer methods lead to the flexibility problems for the real practice especially when accessing in-service systems even though showing successfulness in single mode generation.
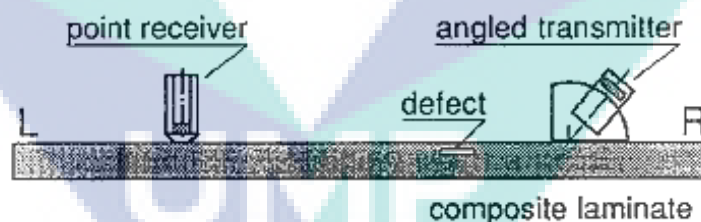
Figure 2.13   The angled transmitter approach for the excitation of the selected LW modes.

Source: N. Guo et al. (1993b)

2.10   Angled Air-coupled transducer

On another case, Castaings et al. (1996) performed the experimental study utilising the angled air-coupled transducer to generate the mode of interest by setting up the appropriate angle of the transducer as shown in Figure 2.14. This study was performed in order to validate the numerical study of the generation, interaction with defects and

detection of the selected LW modes. Hosten et al. (2001) implemented this technique to identify the elastic properties of the fibre glass materials. The A_o, S_o and A_1 modes were successfully generated and the obtained results were in good agreement with the numerical study.
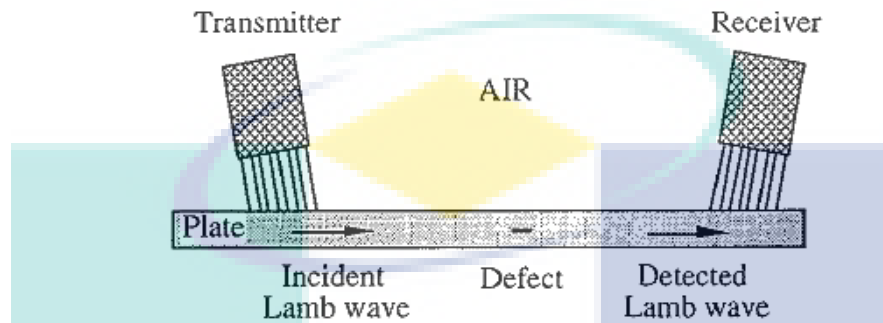
Figure 2.14   The experimental setup for the angled air-coupled transducer performed by Castaings et al. (1996)

Source: Castaings et al. (1996)

2.11   Angled fluid-coupled transducer

Meanwhile, Ghosh et al. (1998) conducted the fluid-coupled transducer setup to excite the individual modes for the internal defect detections as can be seen in Figure 2.15. Transmitter and the receiver were positioned at angle of 17° and 26° from the vertical axis in two small pools of water and it was directly placed over the plate specimen. The findings show that transducer with larger angles projection produces better LW result. This claim also be supported by similar research done by Jia (1997) . The fluid-coupled transducer arrangement was successfully generating particular LW modes. However, air- or fluid-coupled transducers suffers from a low efficiency due to the large differences in mechanical impedances between the air or fluid and the objects under detection (Z Su et al., 2004).
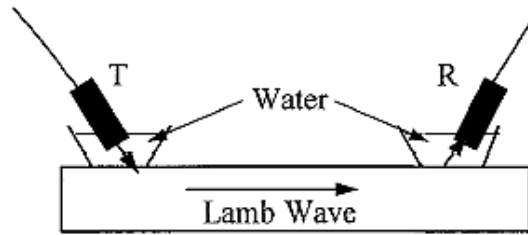
Figure 2.15   Single LW modes generation performed by Ghosh et al. (1998)

Source: Ghosh et al. (1998)

2.12   Actuator embedment

Actuator embedment strategies are other approach that was introduced for the single mode excitation. In recent studies, De Pauw et al. (2017) have demonstrated the use of embedded microstructured optical fibre (MOFBG) based sensors to selectively generate two fundamental LW modes. The excitation of the interested modes was based on the sensor orientation. Its selective sensitivity behaviour to axial and transverse strains allows the generation of preferential modes. The experimental arrangement for this technique can be referred to Figure 2.16. These studies have found similar results with Hailu et al. (1999), which is using embedded piezo-platelet interdigital transducer (IDT) for the single mode excitation. The position of the transducer embedment in the plate thickness defined the generated modes. Symmetric mode was excited if the transducer is embedded exactly at the centre of a plate. However, when the transducer position deviates from the centre, symmetric and antisymmetric will simultaneously generated.
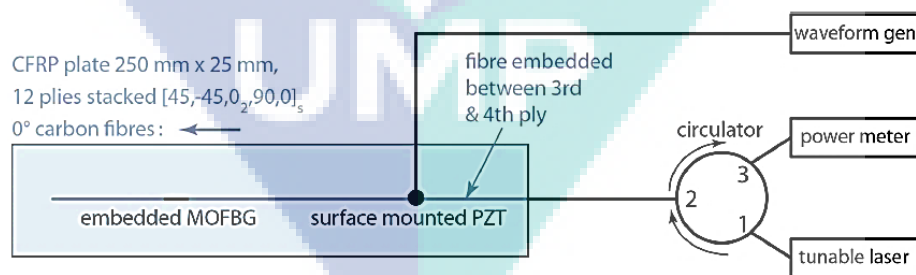
Figure 2.16   The experimental arrangement of MOFBG actuator embedment for the selective generation of LW modes performed by De Pauw et al. (2017)

Source: De Pauw et al. (2017)

Interpretation of the measured LW can be simplified by performing an analysis using a single LW mode. However, these techniques cannot completely suppress the dispersion in recorded responses. Table 2.1 summarises all the information given in the

earlier text about the excitation approaches method for the pure mode generation with their limitations.

Table 2.1   The summarised information about the excitation approaches for the pure mode generation

Method	The procedure to implement this method		Minimum number of actuator used	Limitations
Frequency tuning	The frequency is tuned accordingly for the single mode generation. The value of the optimised tuned frequency value is based on the dispersion curves.		One	1. Time consuming and a tuning frequency may not be available for real practice. 2. System parameters includes the shape of transducer, length and centre frequency, are important consideration in this method.
Double side actuation	A pair of actuator was surface mounted or embedded on the top and bottom of the structure. The in-phase and out-of-phase voltage was exerted to the actuators for the individually mode generation		Two	The higher requirements involving two actuators demanding double transducer numbers, which is increases the hardware requirement compared with the single side excitation method. 2. High consistency in the location of transducer pair is required.
Opposite side actuation	A pair of the actuator was attached in the opposite position to each other on the structure surface. The pure mode generated was depended on the distance between the two actuators (superimposition principle).		Two	
Angle of incidence	Direct techniques	The generation of the selected modes can be obtained by	One	Time consuming and technically challenging for in-service assessment

37

		adjusting the angle of incidence of the actuator.		
	Air-coupled techniques	The angle of transducer was adjusted at appropriate angle to excite the preferential modes.		Suffering from a low efficiency due to the large differences in mechanical impedances between the air or fluid and the objects under detection
	Fluid-coupled techniques			
Actuator embedment	The actuator was embedded at certain thickness of the structure for the separation of the different modes.		one	Symmetric and antisymmetric will simultaneously generated when the transducer position deviates from its original position.

Such selection is believed to be capable of reducing the interference between different wave modes and thus simplifies signal interpretation. All the discussed methods are practically limited, time consuming and tuning frequency may not be available even though it has been proposed as a solution for the single mode generation. Mode conversion phenomenon has converted single modes to the other modes even though a pure mode was excited. Other than that, system parameters, such as the transducer shape, length and centre frequency, must be considered comprehensively when using this technique. (H.-Y. Zhang et al., 2011)

2.13   Chapter conclusions

LW have shown a great potential as a SHM tool due to their advantages. Offering cost-effective evaluation, covering relatively long distances, being highly susceptible to even barely visible internal damage, have made them widely used for structural health monitoring. However, complexity of the captured LW due to their dispersive nature and multimodal characteristics affected the accuracy of the signal interpretation. Consequently, many approaches were introduced by researchers to improve the LW signal interpretation.

Lamb waves excitation method and signal processing approaches are the main solutions that were proposed by researchers. These strategies were applied in order to overcome the effect of multimodal and dispersive problem of the Lamb wave. Some flexible and practical excitation strategies were implemented with the purpose to generate selective pure modes. The mode of interest was decided based on the sensitivity and suitability of the application. It was supposed to ease the following post-processing analysis and provide reliable information during the inspection.

However, these techniques were not completely able to reduce the dispersion effects in the measured signals. Alternatively, signal processing techniques were employed to extract the individual mode. The conventional and newly developed hybrid method was utilised for the mode separation. Each of the proposed method showed their own strength and weaknesses based on their application. It is a continually evolving process for the Lamb wave based SHM system for a better performance. The capability of the developed algorithm to separate the Lamb wave modes is the indicator for the successfulness of the applied approach.

CHAPTER 3

FBGS REAL-TIME IMPACT DAMAGE MONITORING SYSTEM OF GFRP BEAM BASED ON CC-LSL ALGORITHM

3.1   Introduction

Glass-fibre reinforced polymer (GFRP) composite beam has gained its reputation specifically in civil structures over conventional isotropic materials due to its upper hand of having high strength to weight ratio as the main interest. (G C. Kahandawa et al., 2013; Sai et al., 2015) Other dominant aspects such as low cost, ease of fabrication, corrosion resistance, high heat resistance, wear resistance and high specific strength are also the attraction of composite materials. (S. W. Kim et al., 2015; Si et al., 2015) However, anisotropic or orthotropic composite materials are low in toughness where they are often prone to low-velocity dynamic impacts that result in barely visible impact damage (BVID) which is difficult to be analysed through visual inspection. (Baker, 2004) This sudden and total dynamic impact force, F generates more damages due to the act of gravity acceleration, g on the falling object of a constant mass, m governing Newton's law of motion ($F = mg$). This is on the contrary to the static force which acts gradually on the structure over a period of time. Tool drops during service or strikes from a foreign object are the examples of a dynamic impact that propagates into fibre breakage, matrix cracks, and delamination referred to as BVID that makes it possible for degradation of the structural integrity. (Rezayat et al., 2016)

Therefore, structural health monitoring (SHM) that is capable of detecting and localising the impact is crucial in prohibiting the unseen impact damage from growing over time, resulting in fatal destruction. SHM is a process intent in providing precise and in time information regarding the structural condition and performance which involves the observation of a dynamic response from an arrangement of sensors periodically over

time. (G C. Kahandawa et al., 2012) When the impact location is known through an in-situ online real-time monitoring system, the inspection could be made limited to only a certain specific area, thus curtailing the time of inspection and reducing the cost of maintenance. Fibre optic sensor (FOS), specifically fibre Bragg grating (FBG) sensor, has spiked the curiosity of enormous SHM researchers in replacing the conventional Non-destructive testing (NDT) inspections such as ultrasonic testing, (Iacoviello et al., 2016) thermography testing, (Meyendorf et al., 2013) radiographic testing, (K. T. Tan et al., 2011) electromagnetic testing, (Koyama et al., 2013) resistance strain gauge and piezoelectric sensor due to their downsides.

FBGs outperform these traditional sensors by reducing the needs of long distance monitoring cables that could suffer from electromagnetic interference (EMI). Being lightweight and small in physical size enable them to be embedded inside composites and free from damage due to environmental perturbation, sustaining them well above the lifetime of the structures. Embedding an FBG in a composite is also making the sensor to have the same strain as the composite at the related location. Relative signal stability and wavelength multiplexity enable the monitoring of large surface structure. (Allwood et al., 2015; W. Chen et al., 2012; Y. Li et al., 2012; Ren et al., 2014) In civil structures, the beam acts as the backbone that supports the structural element from sudden catastrophic failure. Thus, monitoring of any concentrated mass dropped on the beam can be developed to alert the end user instantly.

Previously, one of our authors has determined the linear impact location on a thin laminated composite plate utilising a linear source location technique through time of arrival (TOA) estimation. (Z. M. Hafizi et al., 2015) However, high-level of uncertain noise due to the indirect sensing nature of the FBG sensor resulted in submerging significant raw impact signal peak spectrum as shown in Figure 3.1, making the time of arrival estimation through peak detection difficult and inaccurate.
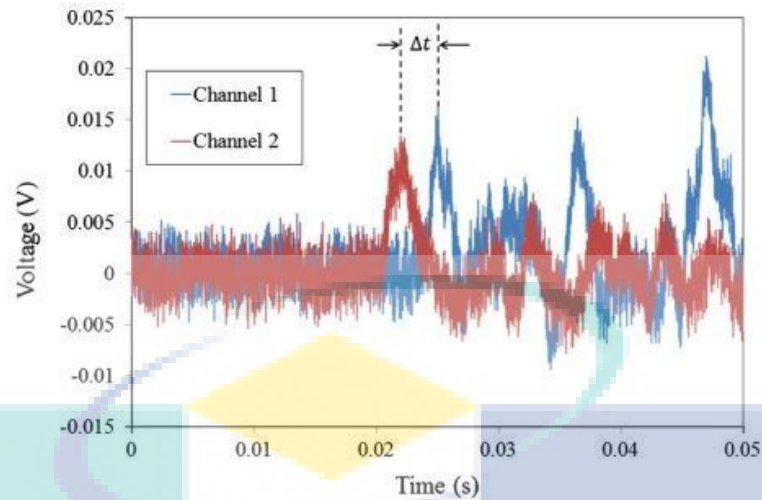
Figure 3.1   High-level of uncertain noise in raw impact signals
Source: Z. M. Hafizi et al. (2015)

Commonly, several algorithms can be utilised in obtaining the time of arrival through peak detection such as autocorrelation algorithm, (Caucheteur et al., 2004) centroid detection algorithm (CDA), (Askins et al., 1995) least square method (LSQ), (Ezbiri et al., 1998) and cross-correlation algorithm. (Huang et al., 2007) Among these algorithms, the cross-correlation approach has demonstrated a good performance in suppressing uncertain noise. (Huang et al., 2014; Qingwen et al., 2011; Wenzhu et al., 2015) Thus, the approach of this paper was to determine the impact location based on time of arrival (TOA) of wave propagation at the sensors where the arrival of time between two sensors was obtained from the cross-correlation algorithm. Once the time difference of both signals was known, the linear source location technique was employed to pinpoint the impact location. The combination of cross-correlation algorithm with the linear source location technique was fully developed in MATLAB graphical user interface (GUI) and functioned entirely in real-time and automatically, which improved the impact localisation. In the meantime, the interest of this experimental work was also to assess the reliability of FBG sensor as a dynamic strain measuring sensor in capturing the natural frequency of a structure. This is due to the failure of a structure which is not merely due to the BVID from a dynamic impact but also can be caused by the excitation frequency approaches and the natural frequency of the structure; (Ling et al., 2006) for instance, the influence of earthquakes on civil structures.

3.2 Theory

This section gives an introduction on the fundamental of the FBG and its working principle. The theoretical explanation is given about wave propagation and also the proposed cross-correlation with the linear source location technique (CC-LSL) impact location algorithm.

3.3 Fundamental of FBG

FBG was made of the standard telecommunication optical fibre consisting of three layers, which are buffer coating, cladding, and core. An intense UV light beam was utilised to inscribe the core region with grating known as Bragg grating which functioned to reflect a specific narrow band of the light source as shown in Figure 3.2. The Bragg wavelength, λ_B can be expressed as: (Park et al., 2003)
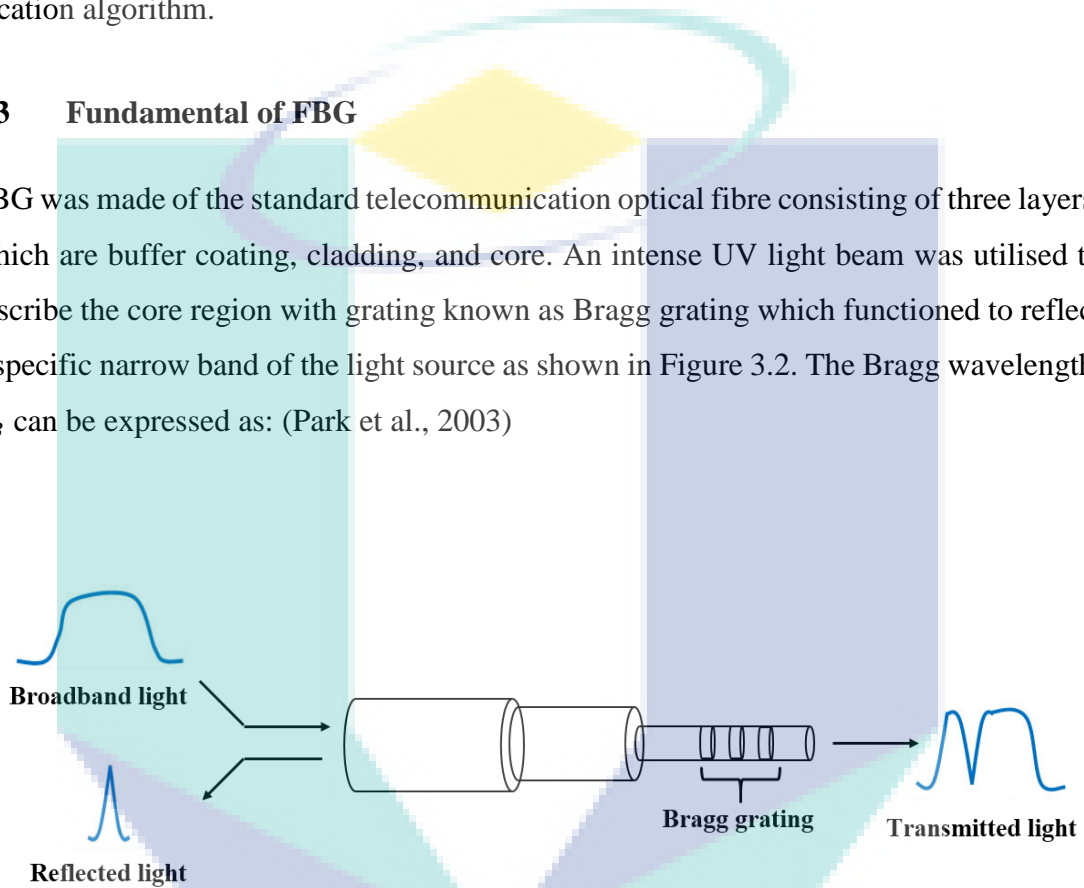
Figure 3.2   The working principle of FBG sensor.

$$\lambda_B = 2\eta_o \Lambda_o / \text{к} \tag{4}$$

where Λ_o is the grating period, к is the grating order and η_o is the initial refractive index before subjected to strain. Expression of Bragg wavelength in terms of the grating refractive index, η_{eff} can be formulated as:

$$\lambda_B = 2\eta_{eff} \Lambda_o \tag{5}$$

The Bragg wavelength shifts are temperature and strain sensitive which can be denoted as: (Majumder et al., 2008; Park et al., 2003)

$$\frac{\Delta\lambda}{\lambda_B} = (\hat{a} + \xi)\Delta T + (1 - p_e)\varepsilon \tag{6}$$

where $\Delta\lambda$ is the change in the wavelength, $\hat{a}$ is the thermal expansion, ξ is the thermo-optic coefficient, ΔT is the change in temperature, p_e is the effective photo-elastic constant of the fibre, and ε is the strain induced. However, this experimental work was carried out in a temperature controlled environment where the change in temperature can be neglected and the expression can be simplified as: (Majumder et al., 2008)

$$\frac{\Delta\lambda}{\lambda_B} = (1 - p_e)\varepsilon \tag{7}$$

3.4 Fundamental of wave propagation

In general, most of the reported work on impact localisation utilised the piezoelectric transducer and pencil lead break to excite the acoustic signal. (Frieden et al., 2012) However, high frequencies are excited through these approaches (Frieden et al., 2012) which are irrational to the cause of low-velocity BVID in which the frequency excitations are mainly low. (Frieden et al., 2012; Haywood et al., 2005) Moreover, recent reported works by researchers in utilising FBGs for impact localisation preferred impact hammer excitation rather than the breaking of a lead pencil and piezoelectric transducer. (Shrestha et al., 2015, 2016; Shrestha et al., 2017) Impact excitation on the structure will generate an ultrasonic guided wave known as the lamb wave.

3.5 Lamb waves

Lamb waves are ultrasonic waves guided between the two parallel traction free surfaces of the structure. (Ambrozinski et al., 2012) Lamb wave propagations have been favourably studied both in metallic and composite materials due to the advantages of long propagation distance with minimal attenuation, making it highly effective in identifying flaws such as delamination and cracks. (Croxford et al., 2007; J. Yang et al., 2016) Lamb waves can be identified as symmetric mode, S and anti-symmetric mode, A according to the motion propagation of the structure. In symmetric mode propagation, the wave motion at the top and bottom surface of the structure is symmetrical to each other. On the other hand, in anti-symmetric mode propagation, the wave motion at the top and bottom surface of the structure is anti-symmetrical to each other. The lamb waves mode propagation can be expressed as (Lam et al., 2009; B. Yang et al., 2017):

For symmetric mode:

$$\frac{\tan(qh)}{\tan(ph)} = \frac{-4k^2pq}{(q^2-k^2)^2} \qquad (8)$$

For anti-symmetric mode:

$$\frac{\tan(qh)}{\tan(ph)} = \frac{-(q^2-k^2)^2}{4k^2pq} \qquad (9)$$

given that:

$$p^2 = \frac{\omega^2}{C_L^2} - k^2 \text{ and } q^2 = \frac{\omega^2}{C_T^2} - k^2 \qquad (10)$$

where $\omega = 2\pi f$ is the angular frequency and $k = \omega/C_p$ is the wave number associated with the lamb wave phase velocity, C_p. C_T and C_L are the propagation velocities for transverse and longitudinal direction, respectively. The thickness of the structure was denoted with h.

3.6 Group velocity

The frequency, ω and structure thickness, h have a significant influence on the phase velocity of the structure that can exhibit the existence of higher order symmetric and anti-symmetric modes. The phase velocity can be formulated as $C_p = \omega/k$ where the wave number, k is related to the wavelength, λ by $k = 2\omega/\lambda$. Governing this relation, the final expression of phase velocity can be formulated as: (Frieden et al., 2012)

$$C_p = \frac{\omega\lambda}{2\pi} \qquad (11)$$

Group velocity, C_g is the overall velocity of the waves propagating through the structure calculated from Equation (11) which can be expressed as:(Frieden et al., 2012)

$$C_g = \frac{\partial\omega}{\partial k} \qquad (12)$$

Since low frequency was excited in this experimental study, the range of frequency-thickness values will not exceed the cut-off frequency(Kundu et al., 2007) of 0.1 MHz calculated for the GFRP beam structure. Thus, other higher order modes were eliminated, leaving only the fundamental symmetric, S_0 and anti-symmetric, A_0 mode. In

addition, the transverse impact introduced in this experimentation will generate and make A_0 mode more significant with a higher amplitude than the S_0.(Frieden et al., 2012) Figure 3.3 shows the dispersion curve of A_0 mode group velocity calculated from the PACshare Dispersion Curves software for the GFRP beam.
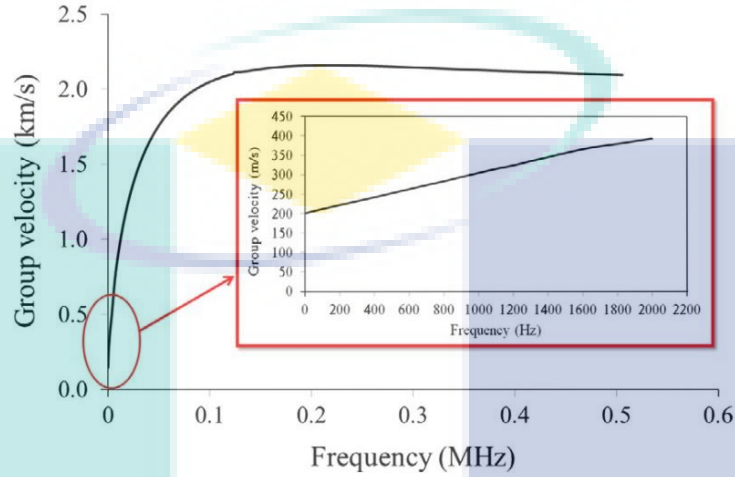
Figure 3.3   The A_0 mode group velocity dispersion curve.

3.7   Cross-correlation with linear source location technique (CC-LSL) impact detection algorithm

Cross-correlation method functions by estimating the time delay of two signals by cross-correlating both the signals and searching for the maximum peak. (Ianniello, 1982; Sun et al., 2016) The signals in terms of samples domain received by both the FBG sensors $x_0(s)$ and $x_1(s)$ can be mathematically modelled as:

$$x_0(s) = z(s) + n_1(s) \tag{13}$$

$$x_1(s) = z(s - D) + n_2(s) \tag{14}$$

where $z(s)$ is the primary signal uncorrelated with noise $n_1(s)$ and $n_2(s)$. The sample delay, D was computed by cross-correlating both the signals with the mathematical expectation, E and over the argument, τ expressed as:

$$R_{x_0 x_1}(\tau) = E[x_0(s)x_1(s - \tau)] \tag{15}$$

In order to estimate the samples differential of the two spectrums, $D(s)$ a windowed cross-correlation was performed which can be expressed as:

$$R_{x_0 x_1}(\tau) = \frac{1}{S-\tau} \int_\tau^S x_0(s) x_1(S-\tau) ds \qquad (16)$$

where S is the observation interval which is the windows size and providing the estimation of $D(s)$ by maximising Equation 15 over τ. Since the delay was obtained in samples difference $D(s)$, the time between two sampling points known as a sampling period, T_s had to be determined which was the inverse of the sampling frequency, F_s expressed as:

$$T_s = \frac{1}{F_s} \qquad (17)$$

Thus, the time difference, Δt in terms of the sampling period, T_s and samples difference, $D(s)$ can be formulated as:

$$T_s = \frac{\Delta t}{D(s)} \qquad (18)$$

where substituting Equation (17) into Equation (18) yielded the time difference, Δt defined as:

$$\Delta t = \frac{D(s)}{F_s} \qquad (19)$$

The linear source location of acoustic emission (AE) technique is a method used to evaluate the time arrival of AE waves received at two sensors where the first arrival or the highest amplitude of the wave is the nearest to the impact induced in a condition in which the impact is restricted between the sensors. (Aljets et al., 2010) The illustration of the linear source location is shown in

Figure 3.4 where the mathematical formulations can be defined as: (Khan et al., 2014)

$$l_2 = \frac{1}{2}(t_1 - t_2).c_g = \frac{1}{2}\Delta t.C_g \qquad (20)$$

$$l_1 = \frac{1}{2}l - l_2 = \frac{1}{2}(l - \Delta t.C_g) \qquad (21)$$

47

where l is the distance between two sensors, l_1 is the distance from the nearest sensor, and C_g is the group velocity of the waves.
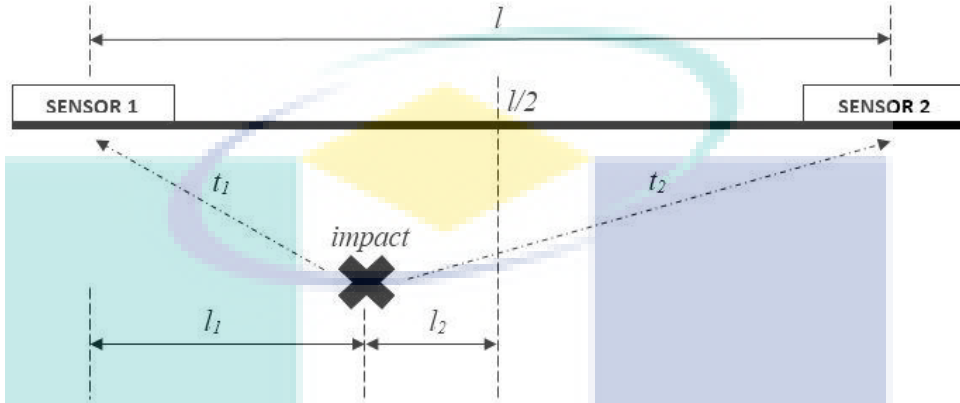
Figure 3.4   Illustration of the linear source location technique. (Khan et al., 2014)

CC-LSL is the combination of cross-correlation and linear source location technique by substituting the time difference obtained in Equation (19) into Equation (21) to determine the impact location, l_1 which gives the finalised algorithm as:

$$l_1 = \frac{1}{2}(l - \frac{D(s)}{F_s} \cdot C_g \qquad (22)$$

The block diagram in Figure 3.5 shows the flow of the CC-LSL algorithm where the signals received by the sensors are denoted as x_i for $i = 0,1$. The signal received by one of the sensors was delayed, depending on the impact distance. Both of the spectrums were then cross-correlated and maximised over τ for peak correlation. The results of both the cross-correlated spectrums were integrated and squared for sample shifts until the peak was detected. The sample difference obtained due to peak correlation was divided with the sampling frequency, F_s to convert to the time difference in the unit of second. Finally, the time difference was fed into linear source location algorithm for impact location detection.
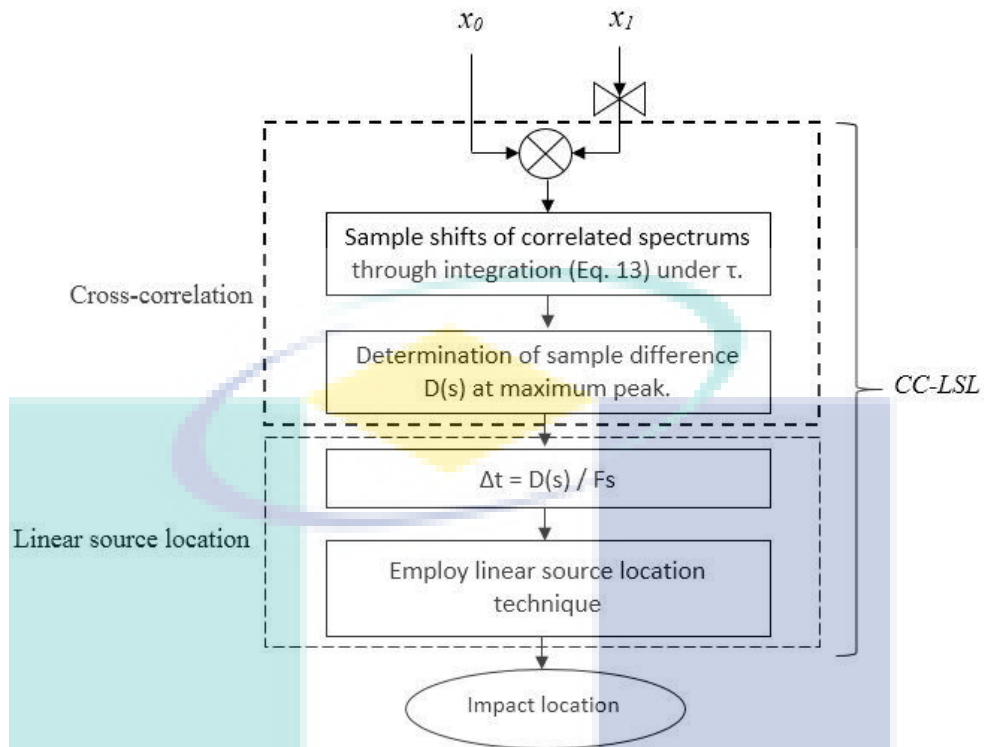
Figure 3.5   The block diagram of the CC-LSL algorithm

3.8   Experimental set-up

An industrial GFRP rectangular beam with the dimension obtained from Zhengzhou Yalong Pultrex Composites Co., Ltd. (en.ylfrp.com) was fabricated by using woven fibreglass with the method of hand lay-up and cured by applying glycidyl (GL) epoxy and hardener as resin. The physical and mechanical properties (Vorathin et al., 2016) of the beam are as in Table 3.1.

Table 3.1   Physical and mechanical properties of GFRP beam

Physical properties		Mechanical properties	
Mass	1158.5 g	$E_{xx} = E_{yy}$	60500 Mpa
Width	65 mm	E_{zz}	62356 Mpa
Height	31 mm	$V_{yx} = V_{xy}$	0.075
Thickness	4 mm	$V_{yz} = V_{xz}$	0.4693
Length	1000 mm	G_{xy}	3900 Mpa

FBG 1, Filter 1 wavelength	1550.441 nm, 1550.423 nm	$G_{yz} = G_{zx}$	1700 Mpa
FBG 2, Filter 2 wavelength	1550.219 nm, 1549.202 nm	ρ	1100 kg/m^3

FBG 1 with the wavelength of 1550.441 nm was embedded inside the composites at the top of the beam, 19.5 cm away from the edge of the beam. FBG 2 with the wavelength of 1550.219 nm was embedded inside the composites at the bottom of the beam, 30 cm away from FBG 1. This top and bottom embedment of FBG was done to evaluate the capability and effectiveness of the cross-correlation peak detection in contrasting wave propagation. Figure 3.6 shows the schematic illustration of the whole experimental system.
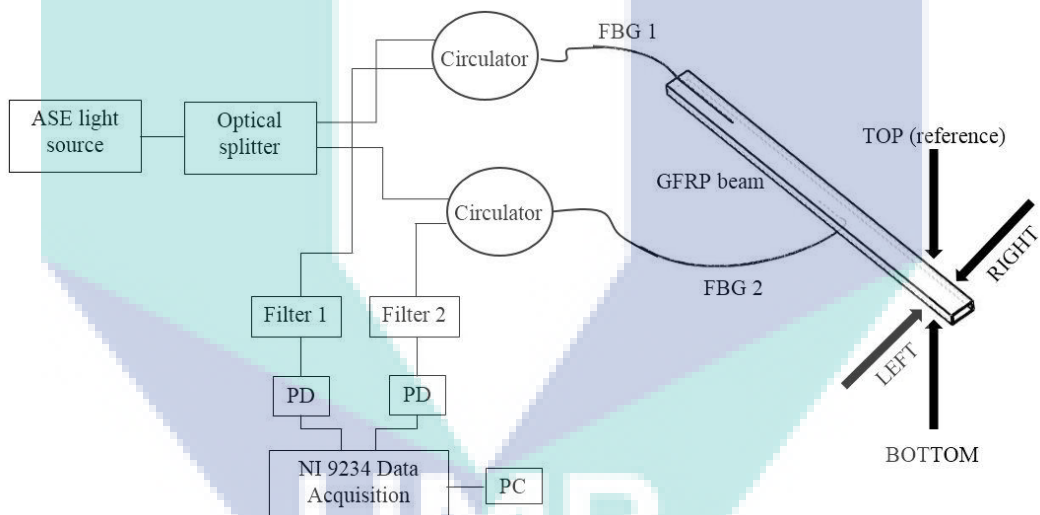
Figure 3.6   The schematic illustration of the whole system

Low-cost edge filter interrogation system was used to eliminate the adoption of expensive signal precision devices such as high-speed interrogation system and oscilloscope. 1431 nm to 1631 nm wavelengths of amplified spontaneous emission (ASE) light source were used to illuminate the sensing and reference FBGs circulating through the optical circulator. 1:8 intensity ratio optical splitter was utilised to split the light signal into two channels and both the reflected spectrums from sensing FBGs which were FBG 1 and FBG 2 were filtered by the reference FBGs which were Filter 1 and Filter 2, resulting in intensity demodulation. Two photodetectors (PD) were used to transform the intensity demodulation into an electrical voltage signal to be read by the National

Instruments NI-9234, demonstrating that the low-cost interrogation system is applicable to any electronic devices such as NI-DAQ or programmable logic controller (PLC) that gives the plug and play fashion.

The beam was clamped and fixed at two ends between two fixtures. In order to demonstrate the accuracy of the proposed method, all four sides of the surface of the beam were assigned with several impact points as illustrated in Figure 3.7. Due to the top and bottom embedment of the sensors, FBG 1 was first assigned as the reference sensor, making it the top surface of the beam. Points A, B and C for the top surface of the beam were induced with a set of impact for 30 trials by using a hard flat chisel. The left and right sides of the beam were induced with impacts as well at points D, E, F, G, H and I, respectively. Next, the beam was inverted, making FBG 2 as the reference sensor. Points J, K and L at the bottom surface were induced with a set of impact. Impact for points at left and right sides of the beam remained unchanged. For better illustration, Table 3.2 summarised the impact points induced on the beam.

Table 3.2   The summarisation of the impact points induced on the beam

Reference sensor	Surface	Impact localisation point	Frequency determination point
FBG 1	Top	A, B	C
	Left	D, E	F
	Right	G, H	I
FBG 2	Bottom	J, K	L
	Left	D, E	F
	Right	G, H	I

Impact at points A, B and C was done 28.5 cm, 46.5 cm and 77 cm away, measured from the edge of the beam. This impact distance was maintained constant for points at the left (D, E, F), right (G, H, I), and bottom (J, K, L) sides of the beam. For impact localisation, the impact points must be executed within the embedment of the two sensors. This was to develop a disparate TOA between the two captured signals. Thus, point A was hit 9 cm close to the right of FBG 1 and point B was hit 3 cm close to the left of FBG 2. Points D, E, G, H, J, and K were hit at the same location within the two

sensors. For better illustration, Figure 3.7 shows the impact locations induced on the beam.
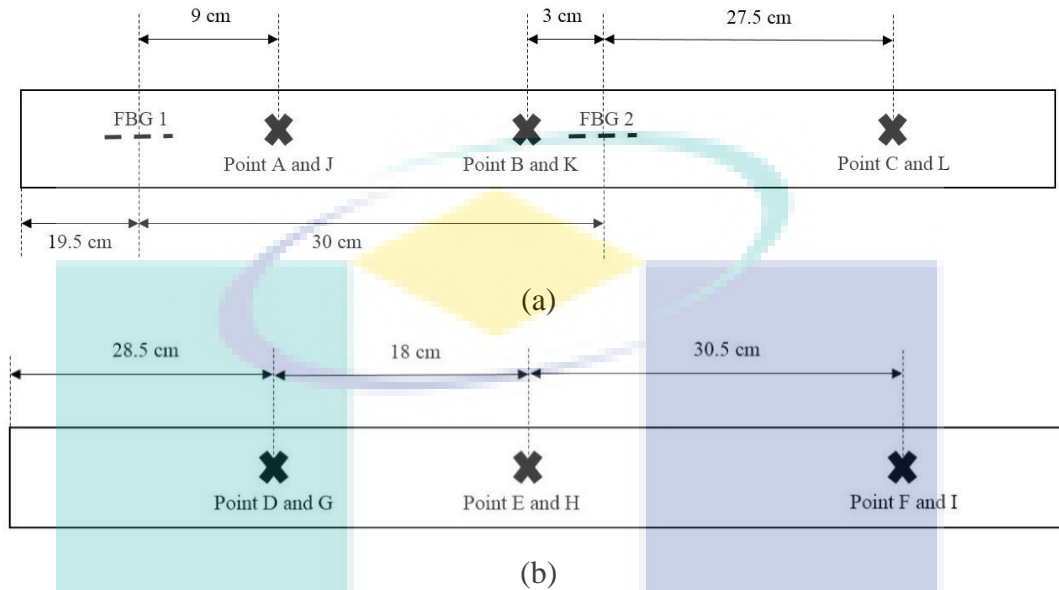
Figure 3.7   The impact locations for: (a) Top [A, B, C] and bottom [J, K, L] (b) Left [D, E, F] and right [G, H, I] sides of the beam.

The frequency determination points (C, F, I, and L) were hit far away from both the sensors' placement. This was to evaluate the capability of the embedded sensor in capturing a frequency spectrum that was far away from the source. FBG 1 was assigned to capture the natural frequency spectrum. For validation, a commercial AE sensor was surface mounted on the beam at the same position with FBG 1 as illustrated in Figure 3.8. In addition, the experimental frequency values were also validated with a theoretical FEA simulation. Here, Abaqus analysis with the boundary conditions fixed at two ends of the beam and mechanical properties as shown in Table 3.1. The maximum frequency to be obtained was set at 1000 Hz. The frequency determination was also done to interpolate the dispersion curve and obtain the C_g.
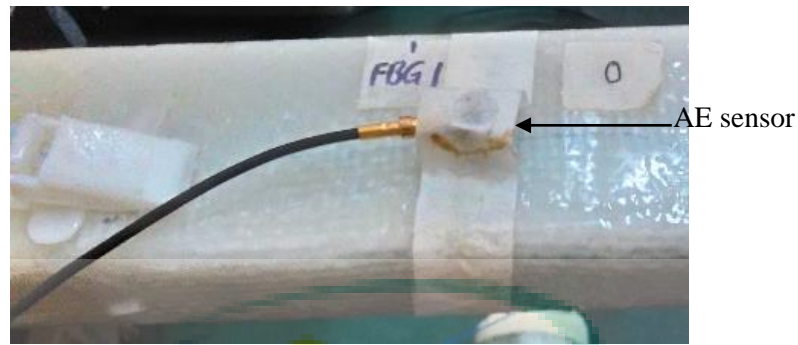
Figure 3.8   The attachment of the AE sensor for frequency spectrum validation

In MATLAB GUI, F_s of 5000 Hz and a window size of 2000 samples were computed for the cross-correlation algorithm. Fast Fourier Transform (FFT) function was split into two windows where the first window was set with F_s of 1000 Hz and the second window was set with F_s of 2000 Hz. This was to preserve the resolution of all the natural frequencies of the structure, specifically for the first mode of the natural frequency. The FFT function was coded in MATLAB GUI to retrieve the natural frequency instantaneously.

3.9   Results and discussion

The cross-correlation approach exhibited a different performance at different signal to noise ratio (SNR) values. Thus, an adequate designation of the SNR's decibel (dB) has to be appointed in order to maintain the precision of the peak detection. Figure 3.9 shows the comparison of the raw impact signals and their cross-correlation performance for particular SNR values where the sampling point was 2000 and the sampling frequency was 5000 Hz. When there was no significant impact peak from the raw impact signal, the cross-correlation approach will not perform the peak correlation for the time delay. This can be seen at SNR = 0 dB where the cross-correlation function did not reflect any sharpness of peak. As the values of the SNR were increasing, the sharpness of cross-correlation function peak started to emerge. The sharpness of the peak indicated the accuracy of the function. At the maximum of 50 dB, the side lobe has been reduced to suppress the noise, resulting in a sharp and pointed peak for a good accuracy in time delay estimation. Thus, SNR of 50 dB was an adequate setting for the peak detection in this experimental work.

SNR = 0 dB

SNR = 10 dB

SNR = 20 dB

SNR = 30 dB

SNR = 40 dB

SNR = 50 dB
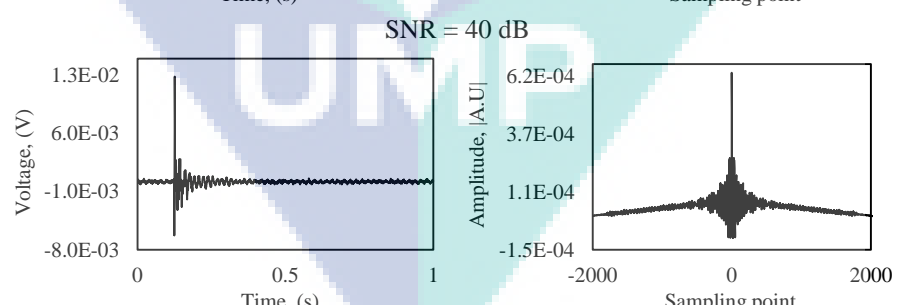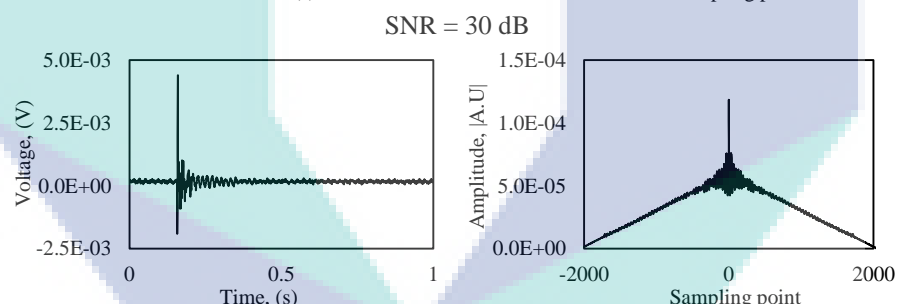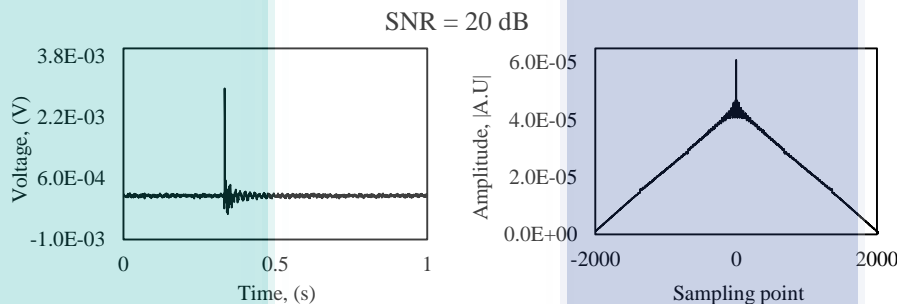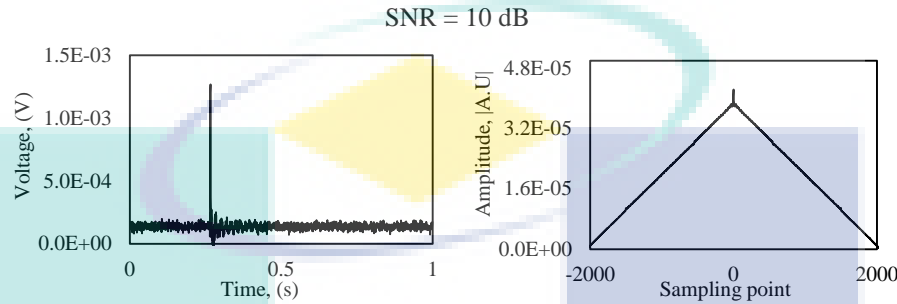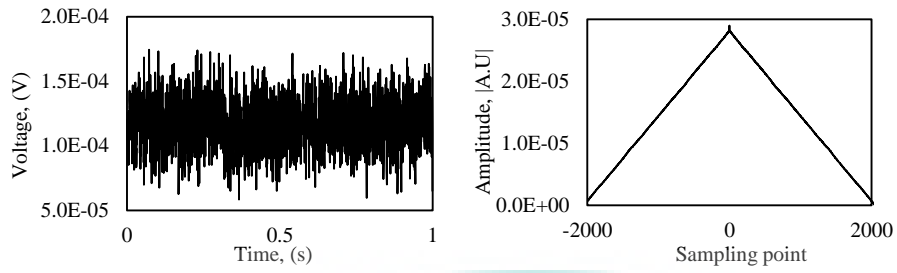
Figure 3.9   The comparison of raw impact signal (left) and the performance of cross-correlation (right) for 0 dB to 50 dB SNR values

Figure 3.10 illustrates the response of raw impact signal against the sampling point when the impact was induced at points A and B, respectively. A clear TOA between the signal from FBG 1 and FBG 2 can be observed when the impact was made close to one of the sensors. Impact at point A was hit 9 cm adjacent to FBG 1 and 21 cm away from FBG 2. Thus, the dispersion of impact signal was early received by the nearest sensor to the impact source which was FBG 1, followed by FBG 2 and on the contrary when the impact was hit at point B.

Indication:
Solid line = FBG 1 signal
Dashed line = FBG 2 signal   (a)   (b)
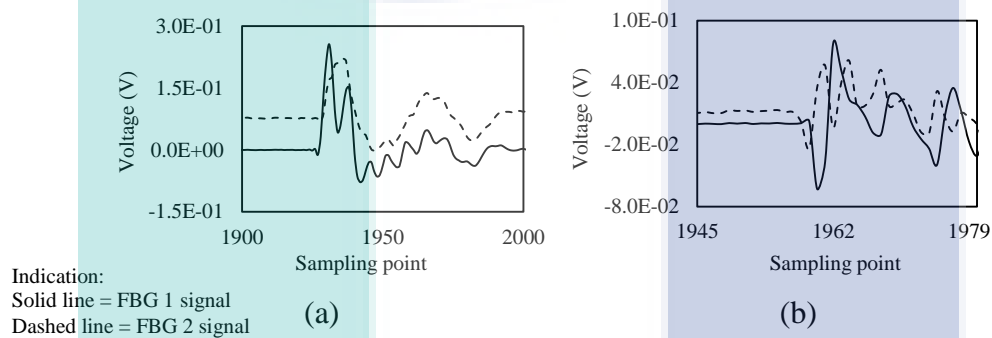
Figure 3.10   The response of raw impact signal for impact at: (a) Point A (b) Point B

The difference in the arrival of time between the two peaks of the signals was automatically estimated for the samples difference and time delay by cross-correlation function. Here, the cross-correlation function intensified the highest peak of both the signals at a lag of zero and shift for the estimation of delay.
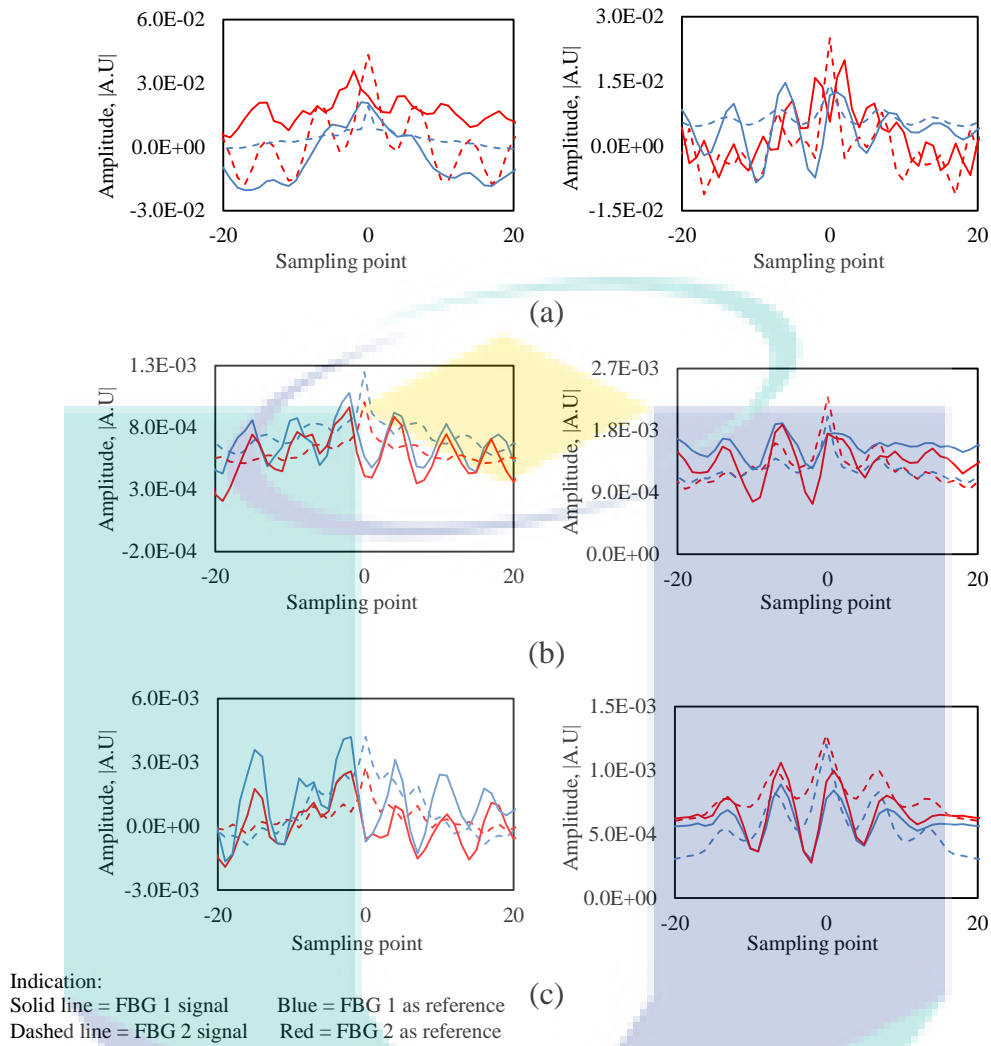
Figure 3.11   The cross-correlation signals for impact at point: (a) A, J and B, K (b) D and E (c) G and H.

Figure 3.11 shows the illustration of cross-correlation signals in estimating the delay for all the impact points. For a better illustration of the peak estimation, the sampling point of the cross-correlation signals have been reduced to the range of -20 to 20 samples. The blue colour mark indicated the cross-correlation signal when FBG 1 was utilised as the reference sensor while the red colour mark represented the signal when FBG 2 was set as the reference sensor.

From the results, it was clearly demonstrated that the cross-correlation amplified the peak of the raw signals to a sharp and pointed peak for the shift of delay estimation. In addition, it was clearly shown that when an impact was hit close to FBG 1, the arrival of the first peak for FBG 2 was certainly subsequent to FBG 1.

56

For all the trials made, the cross-correlation algorithm demonstrated consistency in estimating the sample difference of the peaks for all the impact points. Table 3.3 shows the summarisation of the samples difference and time delay for all the impact points estimated by the cross-correlation algorithm. A clear distinction can be observed for the samples difference and time delay between impact points that were made close to FBG 1 and impacts that were close to FBG 2. Larger samples difference and time delay were estimated for impacts made close to FBG 2 (points B, E, H and K) as compared to impacts that were close to FBG 1 (points A, D, G and J). This was due to the distance needed to be propagated by the signal. For instance, when the impact was made at point A, the signals needed to propagate for a distance of 9 cm to be captured by the FBG 1 and 21 cm to reach FBG 2. However, when the impact at point B was made 3 cm close to FBG 2, the signals were required to propagate 27 cm in order to reach FBG 1. This longer distance of propagation resulted in larger estimated time and samples difference. The highest time difference of 1.8 ms and 9 samples difference were estimated for impact at point H while the lowest time difference was 0.2 ms for impact at point G.

Table 3.3   The summarisation of the samples difference and time delay for all the impact points

Reference sensor	Impact point	Samples difference, $D(s)$ (samples)	Time difference, Δt (ms)
FBG 1	A	2	0.4
	B	4	0.8
	D	2	0.4
	E	3	0.6
	G	1	0.2
	H	9	1.8
FBG 2	J	3	0.6
	K	6	1.2
	D	2	0.4
	E	5	1.0
	G	2	0.4
	H	7	1.4

The values of the time difference estimation were strongly dependent on the sampling frequency. A high sampling frequency will give a higher resolution with more a detailed time of arrival whereas a low sampling frequency will give a larger time difference due to the signal aliasing phenomena. Very good reliability and consistency were exhibited by the cross-correlation function where all trials for all the impact points permitted similar repeatable results.

The FBG sensor has also demonstrated to be an excellent dynamic strain measuring device in capturing frequency response, better than the conventional AE sensor due to its dominant working principle and selective directional property. Figure 3.12 shows the comparison of frequency spectrum between FBG and AE sensors at impact point C, for a frequency range below 500 Hz and 500 to 1000 Hz. Obviously, the trend of curves from the FBG sensor was similar to AE sensor for both of the frequency ranges. However, the frequency spectrum picked up by AE sensor had higher amplitude compared to FBG sensor. This phenomenon can be explained by the aspects of sensor attachment of both the sensors itself. Surface-attached AE sensor will experience more turbulent wave propagation as compared to the embedded FBG sensor inside the composites. Tao Fu et al. have performed a study of embedded and unembedded fibre optic acoustic emission sensors (FOAES) in identifying the impact source on carbon fibre reinforced polymer (CFRP) plate. (Fu et al., 2014) The outcome of the frequency response results showed that the unembedded FOAES had higher amplitude than the embedded one. Furthermore, the studies by Ling et al. (Ling et al., 2006) and Moyo et al. (Moyo et al., 2005) in comparing the frequency spectrum captured by surface mounted strain gauge and embedded FBG sensor showed that the embedded FBG had smaller amplitude. However, for BVID flaw determination, it is crucial for the signal to pass through the internal defect and be captured by the sensor positioned as close as possible to the crack for true detection.

Indication:
Solid line = FBG sensor
Dashed line = AE sensor

(a)   (b)
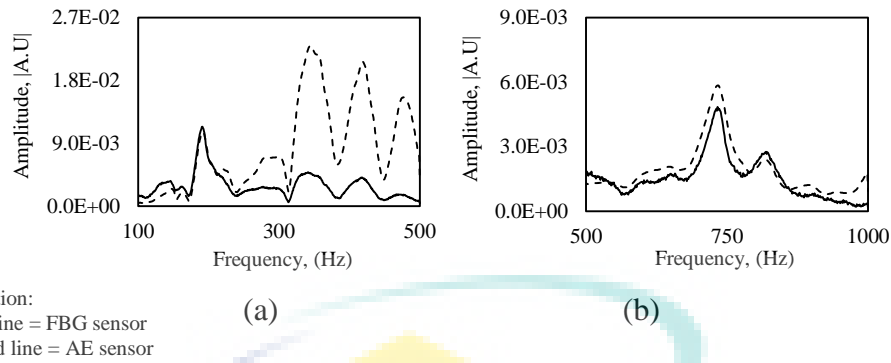
Figure 3.12   The comparison of frequency spectrum between FBG and AE sensor at point C for a frequency range of (a) below 500 Hz (b) 500 to 1000 Hz.

When a perpendicular left and right impact was induced at points F and I, the frequency response picked up by the FBG sensor was exceptionally low in amplitude and barely sensitive. Figure 3.13 shows the frequency response comparison between FBG and AE sensors at impact point F. This was due to the selective directional property of the FBG sensor. Since the embedded FBG was in a direction a parallel to the beam, it was more sensitive to the transverse and longitudinal waves that were in parallel direction with the sensor as compared to the perpendicular wave. However, AE sensor was capable in capturing the frequency response significantly without any loss of amplitude.

This was due to the working principle of the AE sensor that is independent on the direction of wave propagation. In the review by Balaji et al., (Balaji et al., 2016) the authors performed a study on the capability of the transverse and radial pasted orientation of FBG sensor in capturing the elastic wave. The results revealed that different orientations of FBG sensor captured the propagated wave mode differently. The authors also emphasised that due to this certain wave picked up by the FBG sensor, it is desirable and useful in detecting defects in structures.(Balaji et al., 2016)

Indication:
Solid line = FBG sensor
Dashed line = AE sensor

(a)   (b)
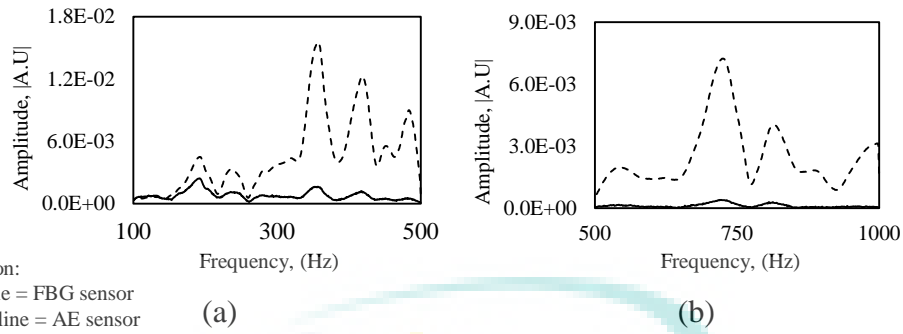
Figure 3.13   The comparison of frequency spectrum between FBG and AE sensor at point F for the frequency range of (a) below 500 Hz (b) 500 to 1000 Hz

(a)   (b)

Indication:
.... Trial 1   Blue = FBG 1 as reference
- - - - - - Trial 2   Red = FBG 2 as reference
_____ Trial 3
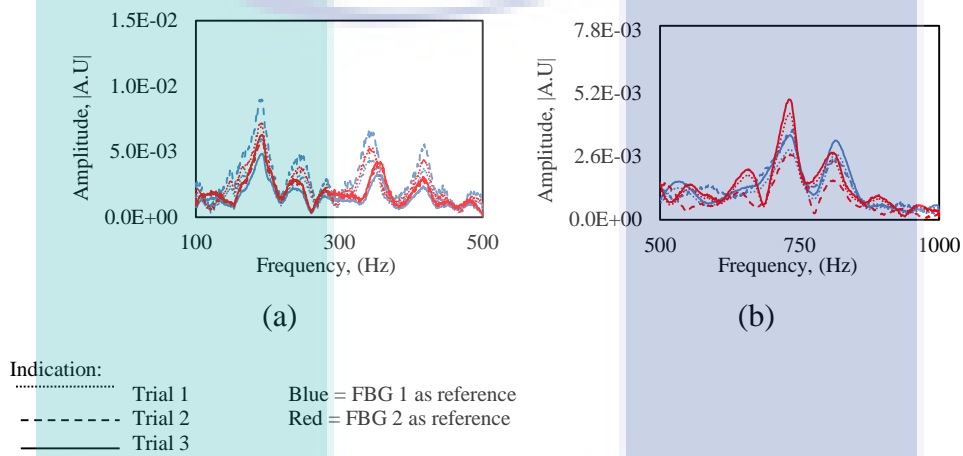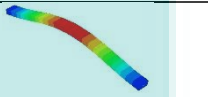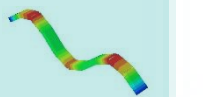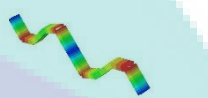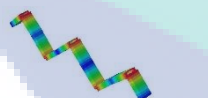
Figure 3.14   The overlay of frequency response captured by FBG sensor for impact at point C and L for frequency range of: (a) below 500 Hz (b) 500 to 1000 Hz

Figure 3.14 shows the example of three trials of frequency response captured by the FBG sensor for points C and L located at the top and bottom surface of the beam which resulted in parallel wave propagation when transverse impacts were induced. Point C was hit when FBG 1 was set as the reference sensor denoted with the blue colour line while point L denoted in the red colour was hit when FBG 2 was set as the reference sensor. From the overlay, the capability of FBG sensor in capturing the frequency response repeatedly and consistently is clearly shown, giving the average frequency values of the first mode as 191.3 Hz, and 347.3 Hz, 415.8 Hz, 736.4 Hz, and 837.9 Hz for the second, third, fourth and fifth mode respectively. The frequency response shows a sharp and pointed peak at the normal mode vibration referred to the mode shape 1, 2, 3, 4 and 5 of the natural frequencies. Table 3.4 shows the validation with FEA analysis for simulated mode shape and natural frequency values. FEA analysis simulated the first

natural frequency values as 187.22 Hz, and 350.46 Hz, 427.02 Hz, 702.31 Hz, and 909.16 Hz for the second, third, fourth and fifth mode respectively.

From the experimental validation, it was decided that the first natural frequency value of the beam was taken as 191.3 Hz and from the interpolation of group velocity curve as in Figure 3.14, giving the C_g as 221.5 ms^{-1}. Substitution of C_g, and Δt from cross-correlation into Eq. 19 summarised the linear source impact location as in Table 3.5.

Table 3.4   The comparison between FEA analysis, FBG sensor, and AE sensor natural frequency values

Mode shape	FEA simulation	Average natural frequency (Hz)		
		FEA	FBG	AE
1		187.22	191.3	192.2
2		350.46	347.3	346.9
3		427.02	415.8	419.5
4		702.31	736.4	735.3
5		909.16	837.9	839.7

Since cross-correlation function estimated a constant time difference for all sets of trials, a persistently measured distance was obtained for all the impact points. From the results, the estimation of impact points was close to the actual hit when FBG 2 was utilised as a reference sensor with the highest relative error of only 1.97%. A slightly greater absolute error was obtained when FBG 1 was set as the reference sensor as compared to FBG 2. The highest relative error was 4.21% with the absolute error of 5.35 cm away from the actual distance. All of the actual and estimated distance was measured from the position of FBG 1.

However, the estimation was still close to the actual hit, even though the top and bottom embedment of the sensors presented a difficulty in impact estimation due to different wave propagations. All of the results revealed that it fell in the acceptable range of relative percentage of error which was below 10%. The relative error was calculated with respect to the total length, L of the beam, expressed as:

$$Relative\ error\ (\%) = \frac{(Estimated+L)-(Actual+L)}{Actual+L} \qquad (22)$$

Table 3.5   The summarisation of linear source impact location results

Reference sensor	Impact point	Actual (cm)	Estimated (cm)	Absolute error (cm)	Relative error (%)
FBG 1	A	9	10.57	1.57	1.44
	B	27	23.86	3.14	2.47
	D	9	10.57	1.57	1.44
	E	27	21.65	5.35	4.21
	G	9	12. 79	3.79	3.48
	H	27	25.07	1.93	1.52
FBG 2	J	9	8.36	0.64	0.59
	K	27	28.29	1.29	1.02
	D	9	10.57	1.57	1.44
	E	27	26.10	0.9	0.71
	G	9	10.57	1.57	1.44
	H	27	29.50	2.50	1.97

For a clear illustration of the estimated impacts, an interpretation of all the discrepancies between all the actual points and estimated points is as in Figure 3.15. The triangular marker represents points A, J, D and G while the circular marker represents point B, K, E and H. The actual points were filled with black colour while the estimated points when FBG 1 was utilised as the reference sensor were denoted in blue colour. The red colour marker represented the estimated points when FBG 2 was utilised as the reference sensor. From the illustration, it was clearly shown that all the estimated hits were close to the actual locations. Thus, the results certainly verified that the CC-LSL algorithm is capable of estimating the impact location on a linear structure.
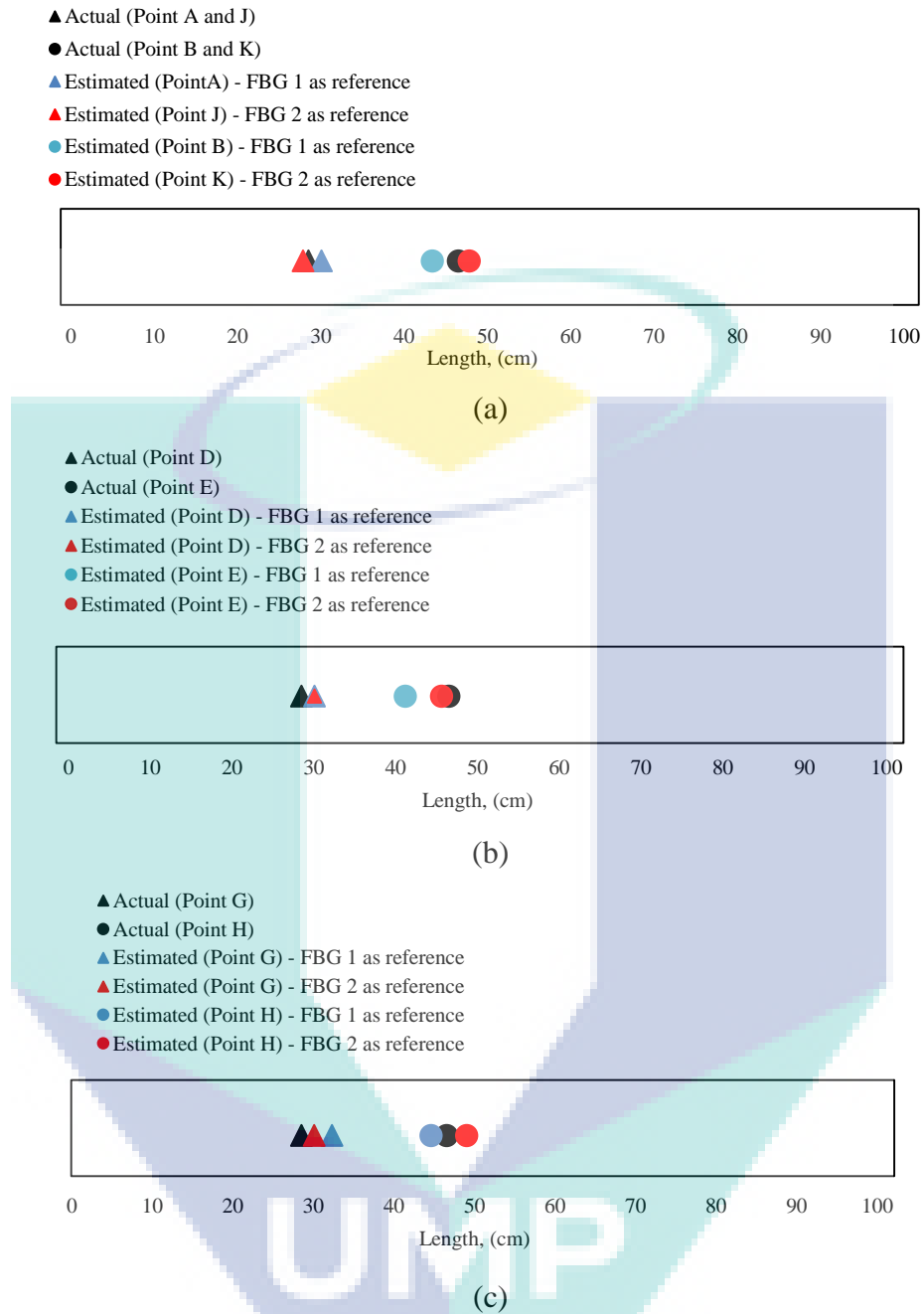
Figure 3.15   The illustration of discrepancies between actual and estimated impact points for: (a) Top and bottom surface (b) Left surface (c) Right surface

3.10   Chapter conclusion

In this chapter, cross-correlation with linear source location (CC-LSL) algorithm to determine the impact location on GFRP beam has been presented. The feasibility of cross-correlation function in estimating the time delay between two signals showed good accuracy, repeatability and consistency in the results, making the estimation near its source of impact with a relative percentage of error less than 10%. The CC-LSL algorithm

is suitable for determining impact location on a linear structure such as beams, pipes, rods and struts on truss bridges. In fact, this algorithm possesses a faster processing time and instantly through the MATLAB GUI real-time monitoring system, hence bringing the FBG monitoring system to approach the idealised key-concept of the smart structure.
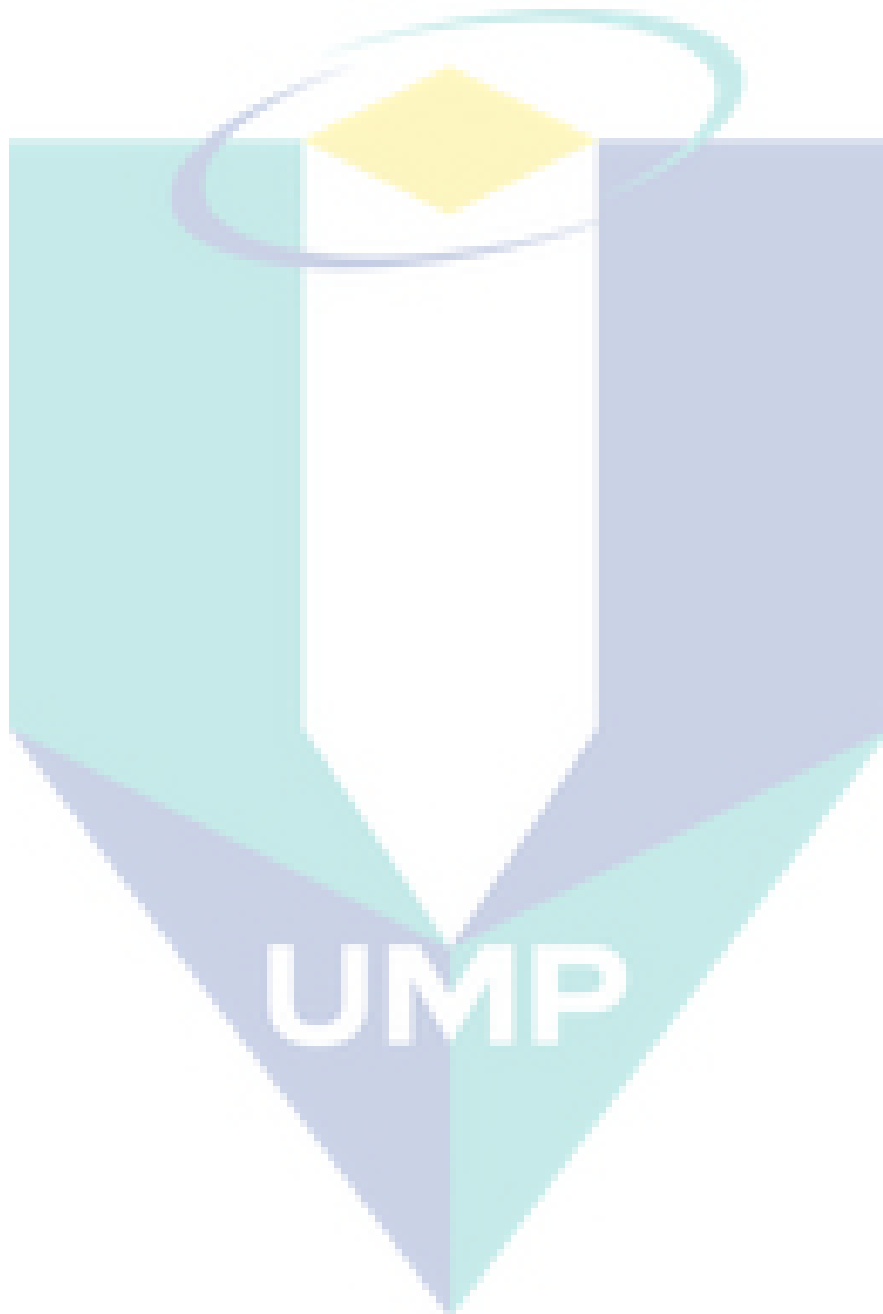
CHAPTER 4

DAMAGE DETECTION OF THE COMPOSITE PLATE USING MATCHED FILTERING OF CENTER OF ENERGY

4.1 Introduction

Fiber reinforced polymer (FRP) composites are becoming the preferred material system in a variety of industrial applications, such as aeronautical and aerospace structures, ship hulls in naval engineering, automotive structural parts, micro-electromechanical systems, civil structures for strengthening concrete members and also in rail transport (Lu et al., 2015). The increased strength and stiffness for a given weight, increased toughness, increased mechanical damping, increased chemical and corrosion resistance in comparison to conventional metallic materials and potential for structural tailoring are some of the factors that have contributed to the advancement of FRP composites (Rezayat et al., 2016).

However, FRP composites materials may suffer harsh environmental conditions when it is in service, such as extreme temperature, stress concentration and impact (Gayan C. KAHANDAWA, 2012). This type of factor will contribute to the delamination. Hidden from superficial visual inspection, delamination often lies buried between the layers, and can begin to grow in response to an appropriate mode of loading, drastically reducing the stiffness of the structure and thus the life of the structure (Gayan C. Kahandawa et al., 2013). Delamination also has a tendency to propagate during cyclic loading and can potentially grow unstably until failure (Kardomateas et al., 1995). Barely visible, makes the structural prediction of delamination is difficult by using surface mounted sensors. To address this issue, embedded sensors must be used.

The fiber Bragg grating (FBG) sensor are a new type of sensing technology, compared with the traditional electrical measuring sensor is one of the most suitable sensors for the above issue since it can embed between the layers of the composites (Innes et al., 2017). It can be embedded in composites during the manufacturing of the composites part with no effect on the strength of the part since the size of the sensor is

diminutive (Martelli et al., 2007). Other than that, FBG has better stability, low interference and high durability, geometrical versatility, corrosion resistance, low weight and anti-interference. Furthermore, hundreds of FBG sensors can be set up in one optical fiber which means that FBG sensors are very suitable to all types of engineering structure or component including slender engineering structures (Zhu et al., 2017).

The application of the FBG sensors in composite materials was started in 1990 when they are embedded into the epoxy resin for the first time and then it was embedded into the concrete for the first time in 1992 for the durability assessment. The problem arise when the embedment process give an effect to the cross sectional of the FBG sensors. One of the most critical is comes from curing process of the matrix (resin)(Fernando et al., 2017). This phenomenon gave a great effect to the damage delamination analysis. Thus, there are many researchers work on this matter.

Based on the aforementioned, one method will be developed for the damage assessment using embedded FBG sensors. This method will implement matched filtering of center of energy (MFCE) method to detect damage of the FRP composites. The pioneer of this method is Chai et al. (2016) (F. W. Lee, Chai, et al., 2016). He used this method to determine and extract the Rayleigh-waves for concrete cracks. From the outcome, this method was able to characterize depth of concrete cracks. Motivated from the similar material group, that is composite, MFCE method will be a promising method to solve the damage detection problems for embedded FRP composite.

4.2   Literature review

The fiber Bragg grating (FBG) sensor is one of the most suitable sensors for the SHM of the FRP composite structures. A FBG sensor consists of regular and periodic changes of the refractive index along the optical fiber core. When the broadband light source is transmitted through a FBG, a narrow-band of the incident light is reflected back. The wavelength of the reflected light, λ_B depends on the effective refractive index of the fiber core, n_{eff}, and the grating period, Λ, (Geng et al., 2017):

$$\lambda_B = 2n_{eff}\Lambda \tag{23}$$

The relative shift in the Bragg wavelength, $\Delta\lambda B$ for an applied strain along the fiber axis by ε under a constant temperature condition is given by

$$\Delta\lambda_B = 0.787\lambda_B \varepsilon \qquad (24)$$

The shift in the Bragg wavelength is positive when the FBG expands. Conversely, the Bragg wavelength shifts to negative when the FBG contracts.

Its capability to detect stress gradients along its length can be used to identify the stress variations in the FRP composites by means of chirp in the reflected spectra of the FBG sensor. This phenomenon can be used to detect damage in the composite structures. The changes of the form of the spectrum can used as an indicator the presence of the flaw. But it was reported that the chirp of the FBG spectrum was not limited to stress concentrations (Guojun et al., 2014). There are other causes of chirp, and it is necessary to eliminate such effects to identify damage accurately.

The nature effect of the embedded FBG sensors is from curing process of the matrix (resin). During the curing process, the FRP composites are subject to shrinkage. The shrinkage depends on the resin used and the fiber fraction (Guojun et al., 2014). The shrinkage applies a compressive loading on the FBG sensor, causes the peak of the FBG sensor has moved to a new peak location after cured.

Other than that, the loading effect also contributes to the distortion of the FBG spectrum. FBG sensors are suitable for strain measurement, and the linear unidirectional sensitivity in the axial direction of the sensor is desirable for accurate and reliable strain readings. In such applications, the FBG sensor undergoes pure elongation or contraction, and hence, the cross section always remains in circular shape. In multidirectional loading cases, the FBG sensor may be subject to torsional deformation other than linear elongation or contraction. For example, when a torque is applied to a composite sample which has an embedded FBG sensor, it undergoes a twist which may cause changes to its cross section. These changes in the cross section of the FBG lead to changes in the refractive index of the core material of the sensor. Since the changes are not uniform along the grating length, the refractive index of the sensor unevenly varies along the grating length of the sensor causing distortion to the FBG spectra. As such, it is obvious that the distortion of FBG sensors is depending on the type of the loading. The change in section geometry of the FBG sensor could lead to the variation of the refractive index of the FBG core material which will cause distortion to FBG response.

The above discussion strongly suggests there is need to develop new method for the post-processing of the dynamics strain signals obtained from embedded FBG sensors.

4.2.1 Lamb wave

Lamb waves are elastic perturbations propagating in a thin solid plate with free boundaries, for which the displacements occur both in the direction of wave propagation and perpendicular to it (Pant et al., 2015). Lamb waves are superposition of longitudinal waves (P-waves) and shear waves (S-waves) and can exist simultaneously in two independent modes, which are symmetric (Sn) and anti-symmetric (An). However, for most practical applications, input signals that excite the fundamental anti-symmetric (Ao) and symmetric (So) Lamb waves are usually considered (Weber et al., 2012). These modes differ from one another by their phase and group velocities as well as their distribution of the displacements and stresses through the plate thickness.

A lot of researches have been carried out on structural damage evaluation in composite and metallic structures using Lamb wave because it has several advantages of application (Carboni et al., 2015). Lamb wave methods need little power for exciting transducers and are suitable for large plate-like structures because of its characteristic of the long-range propagation. Also this technique reduces signal processing time to extract damage information from the sensor signals because it does not require continuous monitoring during operations unlike other piezo-based methods. However, the sensor signals are very complex and difficult to interpret because Lamb wave has multiple modes and the individual modes are usually dispersive.

Solving the Lamb wave equations generates the dispersion curves. Damage can be detected by analysing the difference between the phase or group velocity and the loss of amplitude of Lamb waves on damaged versus un-damaged specimens (Baochun et al., 2015). For an isotropic material, Lamb wave-front is assumed to be circular, which is not the case for composite. Due to mismatch in elastic stiffness between different layers and orientation, Lamb wave propagate differently in different direction (Zeng et al., 2017), (Baid et al., 2015). Therefore, new signal processing technique will be proposed for the damage detection of the composites.

4.2.2 Lamb waves propagation

Lamb wave is one of the guided waves which are induced by free surfaces of plate, shell and tube, and propagates along the directions of length and width. Distinctive features of Lamb wave are that the propagation velocity varies with the exciting frequency times thickness and that there are symmetric and antisymmetric Lamb wave modes in the same frequency. Also, each mode has several orders in some frequency ranges. The propagation velocity of Lamb wave is calculated with Rayleigh–Lamb frequency relation derived from the displacement potential of an elastic body and Newton's equations of motion. Equation 25 is for the symmetric Lamb wave mode in which the particle motion of the plate occurs symmetrically about the symmetric axis of the plate. Equation 26 is for the antisymmetric Lamb wave mode in which the particle motion occurs asymmetrically about the symmetric axis of the plate (Ben et al., 2013).

$$\frac{\tan(qh)}{\tan(ph)} + \frac{4k^2pq}{(q^2-k)^2} = 0 \tag{25}$$

$$\frac{\tan(qh)}{\tan(ph)} + \frac{(q^2-k)^2}{4k^2pq} = 0 \tag{26}$$

where the parameters p and q are defined as follows:

$$p^2 = \frac{\varpi^2}{c_L^2} - k^2, q^2 = \frac{\varpi^2}{c_T^2} - k^2, h = {t}/{2}$$

where ϖ is circular wave frequency, C_L and C_T are the propagation velocities of bulk waves and wavenumber $k = \varpi/C_P$.

4.3   Methodology

A fiber glass reinforced polymer (FRP) composite plate will be fabricated using a woven fiber glass and epoxy resin as shown in Figure 4.1 (a) and (b). Plate structure is considered because many engineering structures are composed of large area of plate. Eight layers of the fiber glass will be used and they will be stack up together with parallel stacking sequence of 0° using hand lay-up method. The parallel sequence of 0° is chosen because of the intention to reduce the parameter that will be considered during analysis in order to obtain more accurate result. The plate size of 80 cm x 12 cm and the thickness

is 0.8 cm will be considered as shown in Figure 4.2. The main reason of interest to that size is to ensure the plate specimen is under thin plate characteristic for the propagating of Lamb waves. Plate theory takes advantage to reduce the full three-dimensional solid mechanics problem to a two-dimensional problem.

Then, an artificial delamination will be created using aluminum sheet metal. Three FBG sensors with wavelength of 1550nm will be bonded on the plate surface by using an epoxy adhesive. Figure 4.3 shows the 1550nm FBG sensor that will be paste on the surface plate.

(a)   (b)

Figure 4.1   Specimen fabrication materials: (a) Fibreglass woven (b) Epoxy and hardener Equations

4.3.1   Impact test

To measure the Lamb wave propagation, the impact tests will be carried out by a 25 g steel ball impacting the plate at point A and B with the form of free fall. This test will be performed separately for impact point A and B. Sensor of FBG 1, FBG 2 and FBG 3 then will measured the propagation of Lamb wave or dynamic strain signal from the impacted ball. Schematic diagram for the impact test experiment set up can be referred to Figure 4.4.
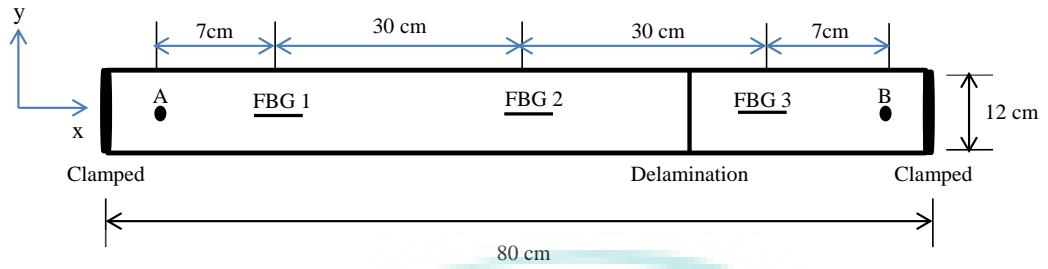
Figure 4.2   A schematic diagram for the fabrication process

Figure 4.3   The FBG of wavelength 1550 nm for the dynamics strain signal measurement
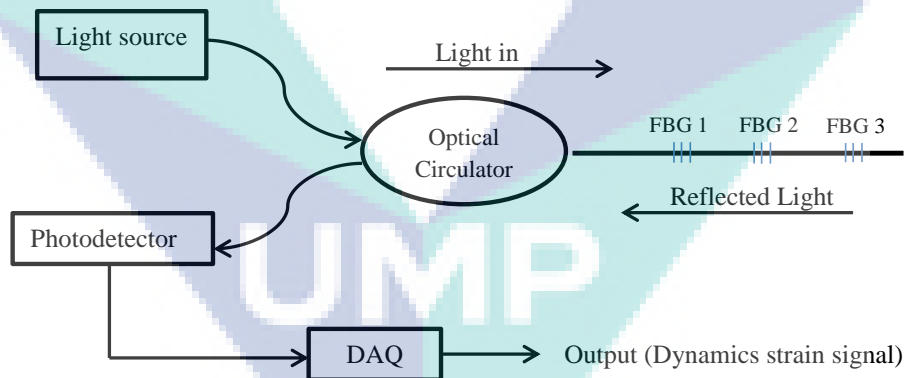
Figure 4.4   FBG interrogation system for the experiment set up

4.3.2   Damage Detection Algorithm

The first stage of the analysis is to determine the type of waves that exist in the dynamics strain signal collected form the FBGs. Theoretically, some type of waves will be induced during the impact testing such as Primary waves (P waves) and Secondary wave (S wave) and Lamb waves (Habib et al., 2013; Martínez-Jequier et al., 2015). Since the FRP composite plate is a thin plate, it is strongly believed that the Lamb waves will be the

dominant wave that is induced during the testing. Therefore, Lamb waves will be used as a subject for this research. The other two waves are assumed to be neglected since Lamb wave is a dominant waves or the largest constituent in the thin plate waveform.

From the literature, Lamb waves are considerably easy to be detected since their arrival is manifested by a strong peak in amplitude (Cho, 2003; Diligent, 2003). Hence, the Lamb peaks can be distinguished from the bulk waves with good confidence even after the waves are blocked, scattered and diffracted by inhomogeneity, e.g. in the form of a surface delamination in FRP composite plate. Normally, Lamb wave peaks could be identified without much difficulty especially in the case for homogeneous medium. However, in a heterogeneous medium, i.e. composite containing a delamination, diffraction and delay in wave propagation occur, resulting in Lamb waves being converged with subsequent body waves, distorted waves and reflected components. This may result in existence of multiple peaks that do not provide significant difference in their respective amplitudes, thus making proper identification for Lamb peaks highly challenging. Thus, the second stage of the developing algorithm is to separate Lamb waves from other wave component.

This study develops the use of a matched filtering of center of energy (MFCE) technique to determine and extract the Lamb waves from the bulk waves. Previously, this method is very successful for the Raleigh waves propagating in a concrete structure (F. W. Lee, Lim, et al., 2016). There is several stages for implemented this technique. Detected signal at sensor i is addressed as S_i (t). To locate the centre of energy of the received signals, the following signal processing has been performed:

$$\frac{t_{c=} \int_{-\infty}^{\infty} t |S_i(t)|^2 \, dt}{\int_{-\infty}^{\infty} |S_i(t)|^2 \, dt} \tag{27}$$

It has been mentioned that the Lamb wave is the largest constituent in the waveform among the other waves. The power of two in the expression is to discriminate the wave components (P-waves and S -waves) in the waveform and help locate the position of the center of energy for Lamb wave. It is undesirable that the energy of the other two wave components, namely P- and S-waves are to affect the accuracy of the proposed algorithm. This can be improved by increasing the power factor. However, for the current study, a power factor of two was found to be sufficient in obtaining the desired

outputs. After acquiring the time position of center of energy for Lamb wave, windowing on the selected portion of signal was performed to eliminate the undesired tail or echo of the signal.

$$w(t) = \begin{cases} 0, & |t| > \sigma \\ 1, & |t| \leq \sigma \end{cases} \tag{28}$$

where σ is the window and the windowed signal is expressed as follows:

$$S_{w,i}(t) = w(t - t_c)S_i(t) \tag{29}$$

Lastly, matched filtering on each processed signal [Sw,i(t)] was performed with the processed signal acquired from the first sensor [Sw,1(t)]. Hence:

$$C(t) = \int_{-\sigma}^{\sigma} Sw_{,i}(\tau).S_{w,1}(t - \tau)d\tau, i = 1 \; to \; 3 \tag{30}$$

$$t = t_{peak,i,} \text{ when C(t) is maximum} \tag{31}$$

The matched filtering helps eliminate noises in the signal and tpeak marks the position where the matching of Sw,1(t) is optimum. $t_{peak} = 0$ is the result of autocorrelation and it is used as the reference to locate the time position for the other signals. The damage of the composite will be traced by the delay in peak time (t_{peak}) from the plotted graph frequency versus t_{peak}.

4.4   Results and Discussion

Time domain signal of the wave propagation measured from the impact test can be referred to Figure 4.5. It can be seen that the signal from Figure 4.5 (a) and (b) shows an identical signal profile. Whereas, signal measured from delamination area present a different signal profile. The waveform of Lamb wave for delamination distorted or slightly change compared to the healthy area. Other than that, the amplitude for delamination is also decreased compared with healthy area.
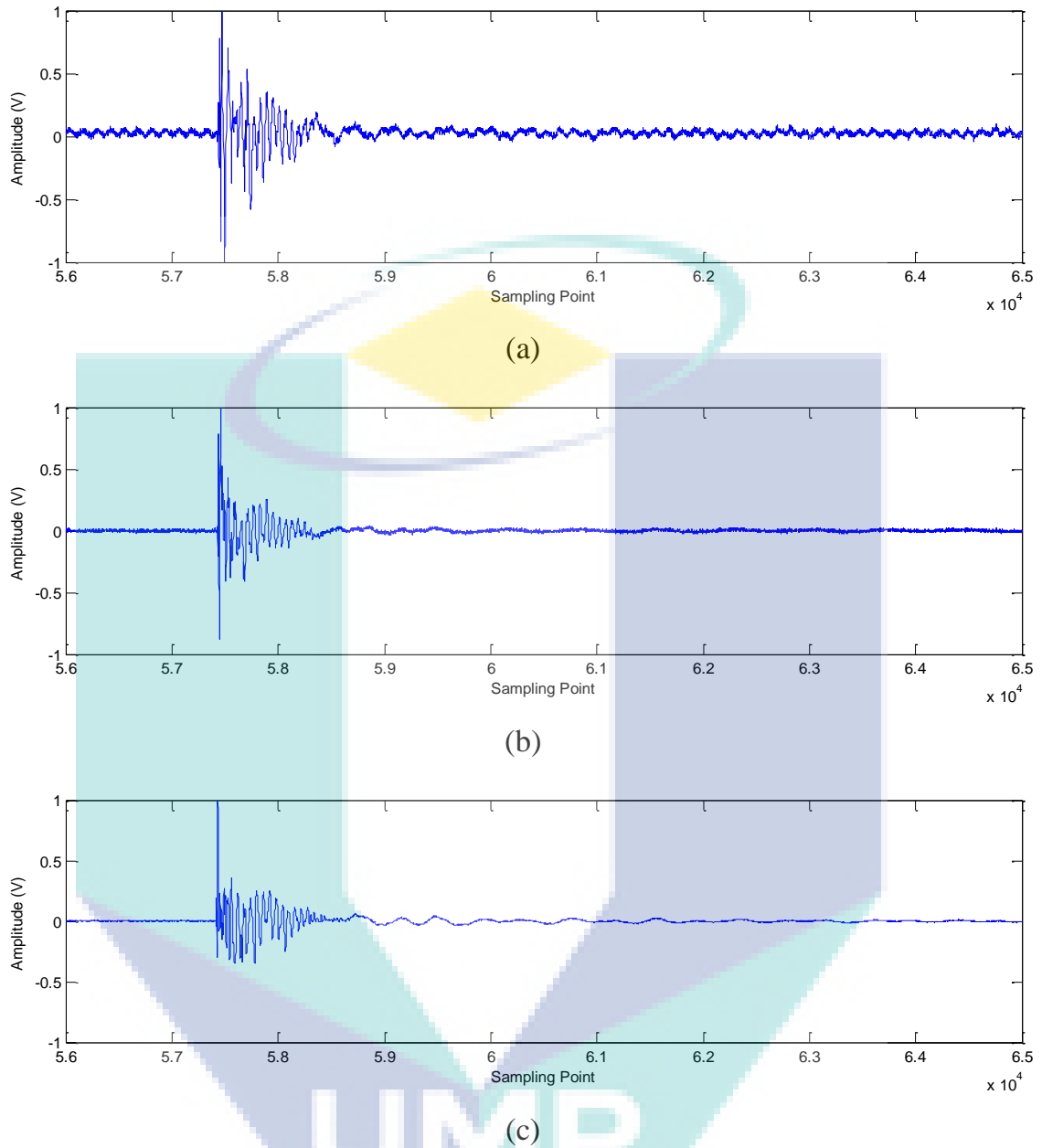
Figure 4.5   The strain signal measured from three FBGs for impact test at point A;
(a) Reference signal, (b) Healthy signal and (c) Delamination signal

Then the signal was analysed using the developed algorithm for the time of arrival
of the wave. Figure 4.6 (b) shows there is a delay about 1.3ms for the wave travel from
the acoustic source to the FBG 2 and FBG 3. From this delay of time of arrival, it proved
that this method can determine the delamination presence in the FRP composite.
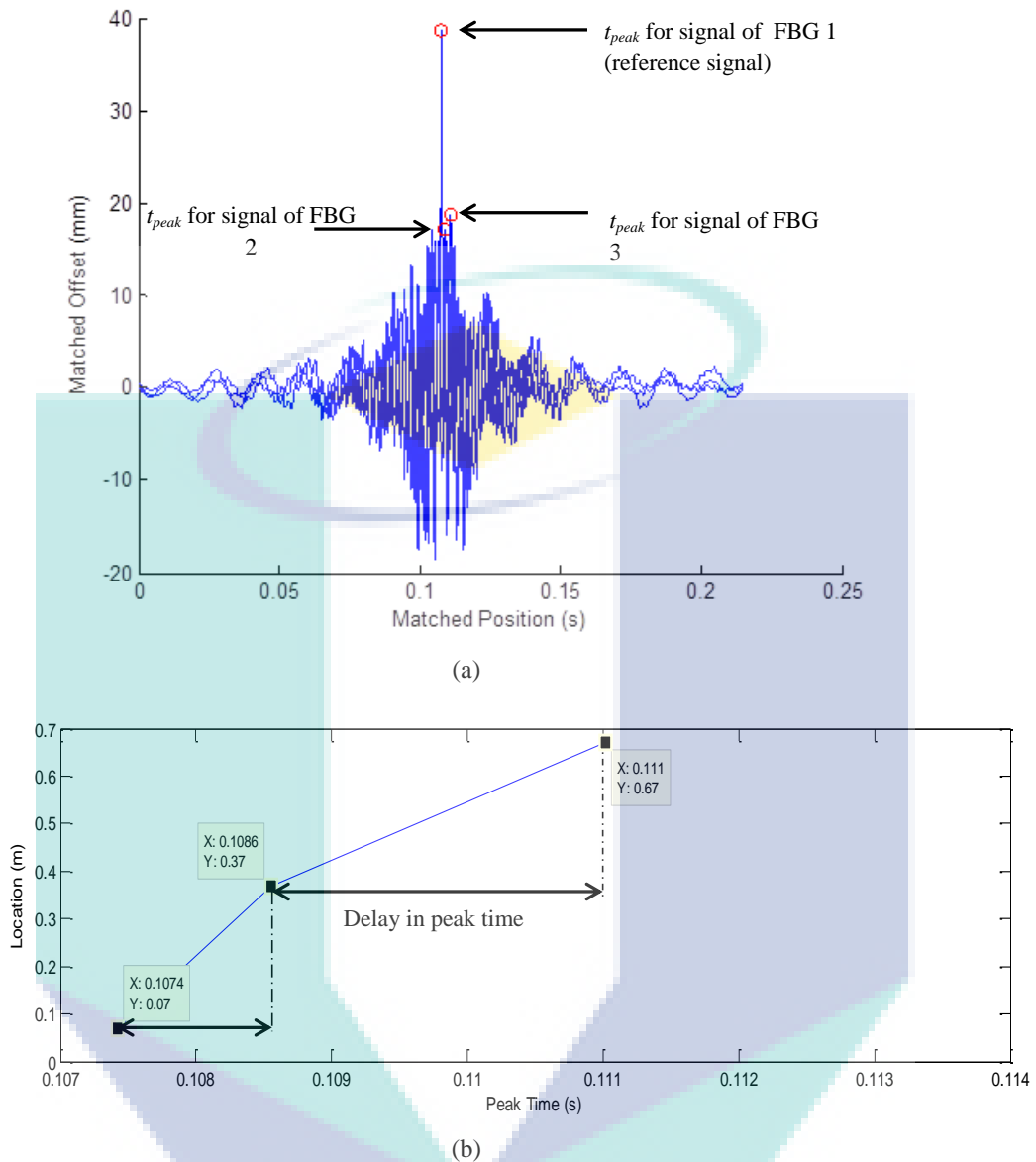
Figure 4.6   The expected result from the matched filtering of maximum of energy;
(a) Autocorrelation between reference signal and healthy and delamination, (b) plotted
graph of location versus peak time

4.5   Chapter conclusion

One post-processing analysis was developed to solve the damage detection in the FRP composite by using matched filtering of centre of energy method. The time of arrival of the wave is used as an indicator for the condition of the structure. The delay in time shows that there is flaw in the composite structure. Thus, it was proved that this method can be used to detect damage in FRP composite quantitatively.

CHAPTER 5

INTERACTIONS OF LAMB WAVES WITH DEFECTS IN A THIN METALLIC PLATE

5.1   Introduction

Structural health monitoring (SHM) has gained more attention among researcher due to its ability to allow a continuous supervision of the structural integrity of any operational systems. Among the various developed techniques, Lamb waves have shown capability to be utilised as one of the SHM approaches. The principle advantage of this method is performing the inspection over long distances from a single probe position. They are very sensitive to any changes of the structural properties even at a tiny scale or underneath structural surfaces and able to detect any types and sizes of defects (Khalili et al., 2016; Worden, Farrar, Manson, et al., 2007). Moreover, they feature prominent merits like low attenuation, low energy consumption and convenience in actuation or acquisition. These characteristics make Lamb waves as one of the promising diagnostic tool. However, there are several challenges when utilising Lamb wave method in the SHM system. Multimodal and dispersive nature makes the Lamb waves interpretation difficult. Multimodal property refers to the existence of at least two modes that coexist at any given frequency, which leads to multiple wave packets in the acquired signal. On top of that, other wave characteristics such as wave dispersion, which is associated with the velocity of each mode which, varies with respect to its frequency (Alleyne et al., 1992) have added complexity to the analysis of the signal. This complexity may lead to the wrong diagnosis and false alarm in the inspection. Thus, the understanding of Lamb waves propagation plays an important role in the successful application of Lamb waves for damage

detection. The aim of this paper is to simulate the wave propagation of the Lamb waves in the aluminium plate and its interaction with the damage slot defects.

Time domain analysis including time of arrival (TOA) and signal attenuation were performed in order to study in details the effect of defects to the Lamb waves propagation. The changes of these parameters may be used as an indicator for the existence of damage. Finally, a short-time Fourier transformation (STFT) is applied to observe any changes of the frequency content. All the extracted features can be used as the defects signature for the SHM diagnostic system.

5.2   Simulation of Lamb waves

Lamb waves are ultrasonic guided waves which are induced by free surfaces of plate, shell and tube, and propagates along the directions of length and width. They made up of a superposition of longitudinal can be classified as symmetric and anti-symmetric mode, which is exist simultaneously and propagate independently of each other. The symmetric modes are symmetric with respect to the mid-plane of the plate and are noted S_i, where i is the order or number of the mode. The anti-symmetric modes are anti-symmetric with respect to the mid-plane of the plate and are noted A_i. Fundamental symmetrical, S_0 and anti-symmetrical, A_0 mode is the lowest order of the mode and followed by and A_1, A_2, A_3, …. A_∞, respectively. Symmetric mode having symmetric deformation about the mid-plane and the particles inside the plate primarily have in-plane motions. The displacements in x direction are larger than the displacements in y direction. Particles at the top and at the bottom experiencing the same direction of displacements in the x component and opposite direction in the y component as illustrated in Figure 5.1 (a).

For the A mode, the deformation of the plate is anti-symmetric and the particles inside the plate have out-of-plane motions. The displacements in y direction are larger than x direction. The displacements for y direction are in the same direction and x component in the opposite directions for particles at the top and bottom (Graham Wild et al., 2008) as shown in Figure 5.1 (b).

(a)   (b)
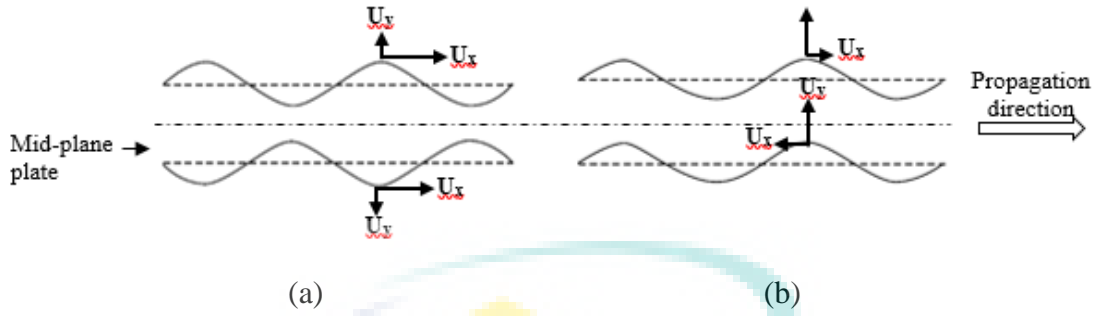
Figure 5.1   Propagation of the (a) symmetric mode and (b) anti-symmetric mode

The number of existing modes for a plate structure depends on the product of excitation frequency and thickness (*fd*). An excitation frequency must be decided properly before performing any analysis regarding Lamb waves propagation in order to minimize the number of generated modes. For signals simplification, it is a common practice to apply low excitation frequencies, so that only fundamental modes (S_0 and A_0) exist. The reference for the appropriate excitation frequency can be referred to theoretical dispersion curve and it was generated using Equation (1) and (2). Referring to that equations, different material with different plate thickness will produce different dispersion curves. Figure 5.2 is the dispersion curve for group velocity dedicated for this present study, which is using aluminium plate with thickness of 2 mm. This curve is generated using PACshare Dispersion Curves software. It can be seen that the number of modes increases with the excitation frequency. Thus, infinite number of symmetric and anti-symmetric modes can exist. Referring to that figure, excitation frequency more than 800 kHz can generate more than two modes which leads to complexity of the recorded signals. For this study, the excitation frequency of 200 kHz as shown in Figure 5.3 is chosen for the Lamb waves actuation. Thus only two modes exist that is S_0 and A_0. The characteristics of these two modes was studied in detail for a better understanding of their interactions with defects. The existing feature signatures influenced by the defects were extracted for further studies.

$$\frac{\tan qh}{\tan ph} + \frac{4k^2 pq}{\left(q^2 - k^2\right)^2} = 0 \tag{32}$$

$$\frac{\tan qh}{\tan ph} + \frac{\left(q^2 - k^2\right)^2}{4k^2 pq} = 0 \tag{33}$$

where the parameters p and q are defined as follows:

$$p^2 = \frac{\omega^2}{c_L^2} - k^2 , q^2 = \frac{\omega^2}{c_T^2} - k^2 , h = \frac{d}{2} \text{ and } k = \frac{\omega}{c_p},$$ where ω is circular wave frequency, k

is wavenumber, c_p is phase velocity, c_L and c_T are the propagation velocies of bulk waves. From Equation (32) and Equation (33), the phase velocity, c_p dispersion curves can be plotted. The other useful plot is group velocity dispersion curves which can be derived from the phase velocity curves using Equation (34). The c_p is propagating velocity of the wave with a single frequency and c_g is the propagation velocity of the wave packet with adjacent multi frequencies.

$$c_g = \frac{d(kc_p)}{dk} = c_p + k \frac{dc_p}{dk} \tag{34}$$
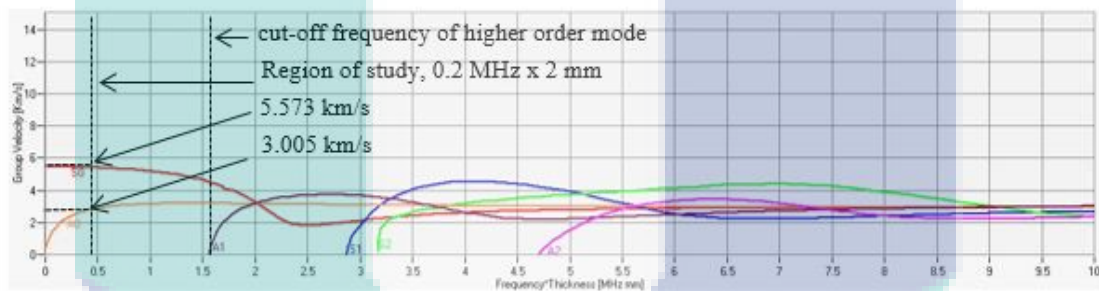
Figure 5.2   Theoretical dispersion curve of group velocity against frequency for aluminium plate with thickness of 2 mm
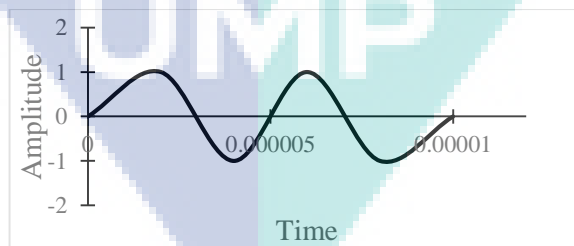
Figure 5.3   A two-cycle sinusoidal impulse for excitation input

5.3   Finite element modelling

A 3D FE method was used to simulate the interaction of the Lamb waves with defects in an aluminium plate specimen. A commercial finite element software package was used to model the geometry, generate the meshing and perform the dynamics simulation of the

Lamb waves propagation. Attention should be paid to two main parameters for dynamic analysis of Lamb waves propagation, i.e. element edge length, L_{min} and time step, must be chosen in order to obtain a good convergence of the numerical solution (Leng et al., 2003; Rosenthal et al., 2011). A quadrilateral mesh with the L_{min} of 0.8 mm is used in this study to satisfy the criteria that there are at least 10 elements across the smallest wavelength, λ_{min} of interest (Tsuda et al., 2010). This value ensures that the propagating waves are spatially resolved. By using the that parameter, 3800000 elements were produced. Δt with value of 5 ns is used in order to meet the criteria that at least 20 time steps during the cycle of a wave at the highest frequency. Choosing an adequate integration time step is very important for the accuracy of the solution The mentioned criterion can be referred to the condition (35) and (36) (A. Wada et al., 2012).

$$L_e \langle \frac{\lambda_{min}}{10} \tag{35}$$

$$\Delta t \langle \frac{1}{20 f_{max}} \tag{36}$$

5.3.1 Healthy plate simulation

Simulation of the healthy plate was performed in order to obtain the baseline signals that will be used as the reference for the comparison analysis for damaged plate. The interaction of the Lamb waves with the defects was extracted by using this baseline signals. The sensor was placed at distance of 10 cm from the actuation point to avoid the superimposed between S_0 and A_0 mode as discussed in section 2.0. It was observed that there is sufficient time for mode separation at this distance. The sensor was placed at ten different distances for the wave velocity calculation, which is varied, from 10 cm to 28 cm with graduation of 2 cm, as shown in Figure 5.4 (a). Figure 5.5 shows the recorded signals at ten different distances. Two main wave packets were observed in each of the displacement time domain. The velocity of each of the wave packet was used as the indicator for the type of mode determination and it is depicted in Figure 5.6. It was calculated that the velocity of the first wave packet is 5573 m/s and for the second wave packet is 3005 m/s. Referring to the theoretical dispersion curve, the first wave packet is the S_0 and the second wave packet is the A_0.

(a)

(b)
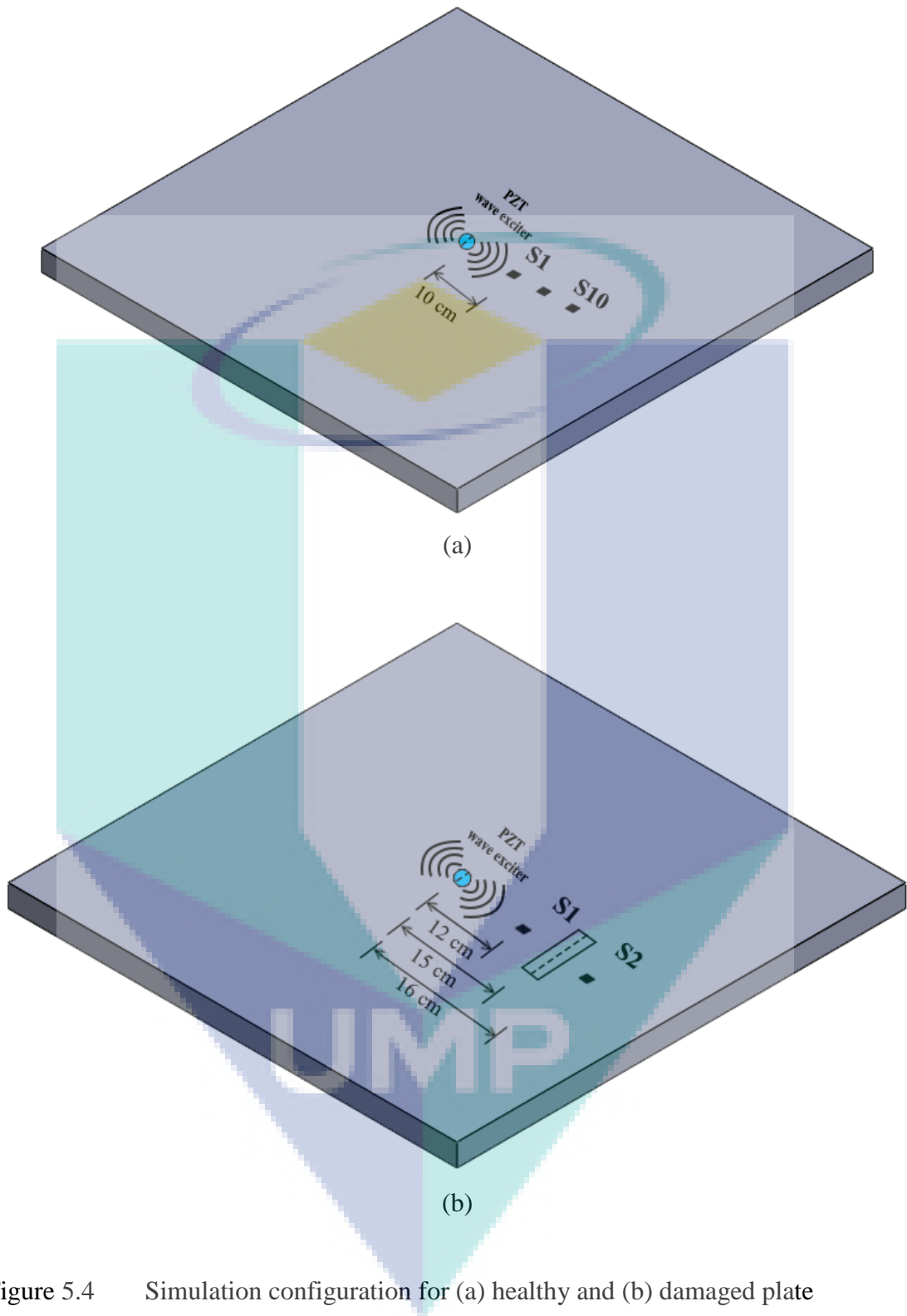
Figure 5.4   Simulation configuration for (a) healthy and (b) damaged plate
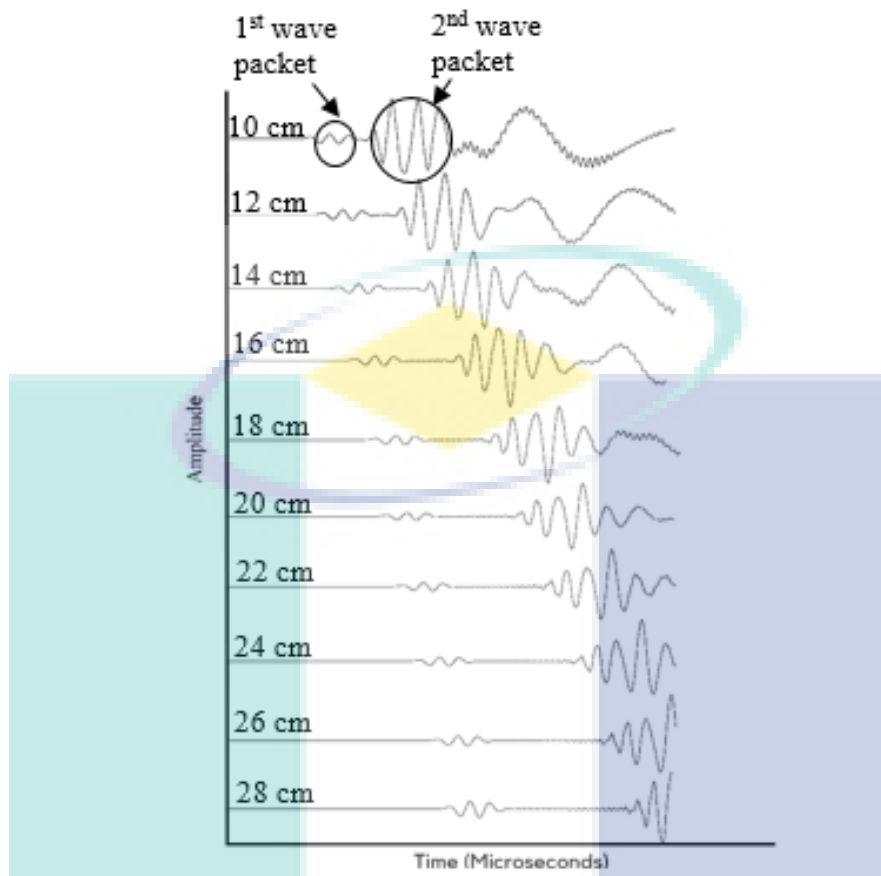
Figure 5.5   Displacement signals at ten different position
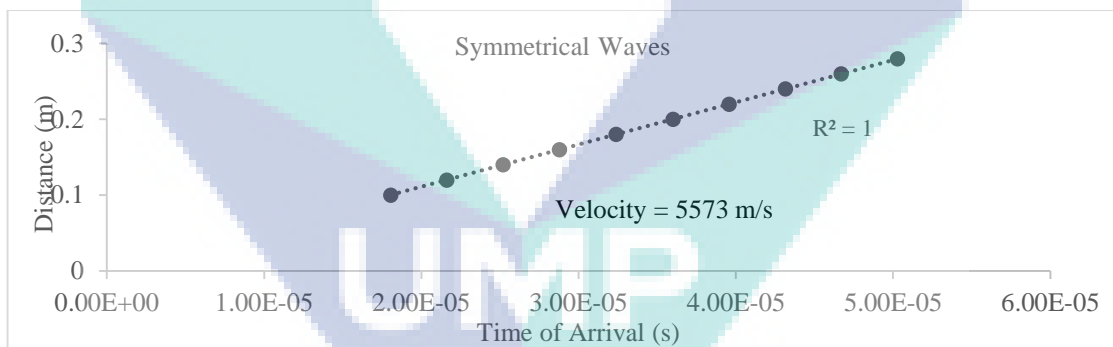
(a)
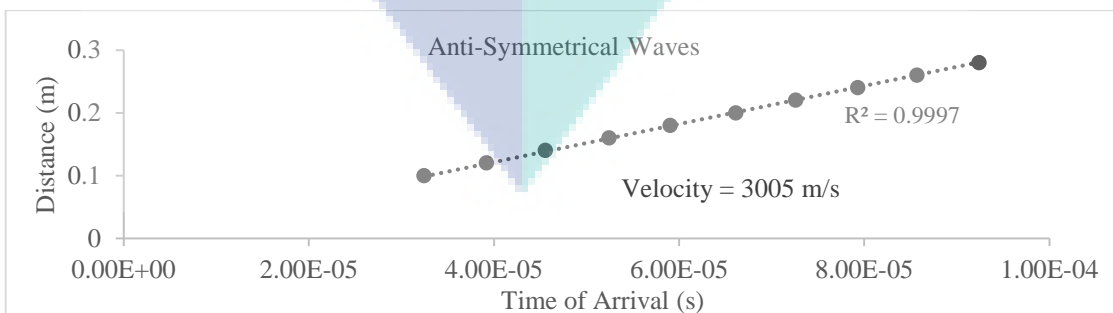
(b)

Figure 5.6   The group velocity of (a) symmetrical mode and (b) anti-symmetrical mode

82

Other than time domain signals, visualisation of the wave propagation also generated for this simulation study. Healthy plate shows a smooth contour as presented in Figure 5.7 (a). *So* mode was obviously moving faster than *Ao* mode. This wave visualisation is in well agreement with the calculated group velocity.

(a)   (b)

(c)
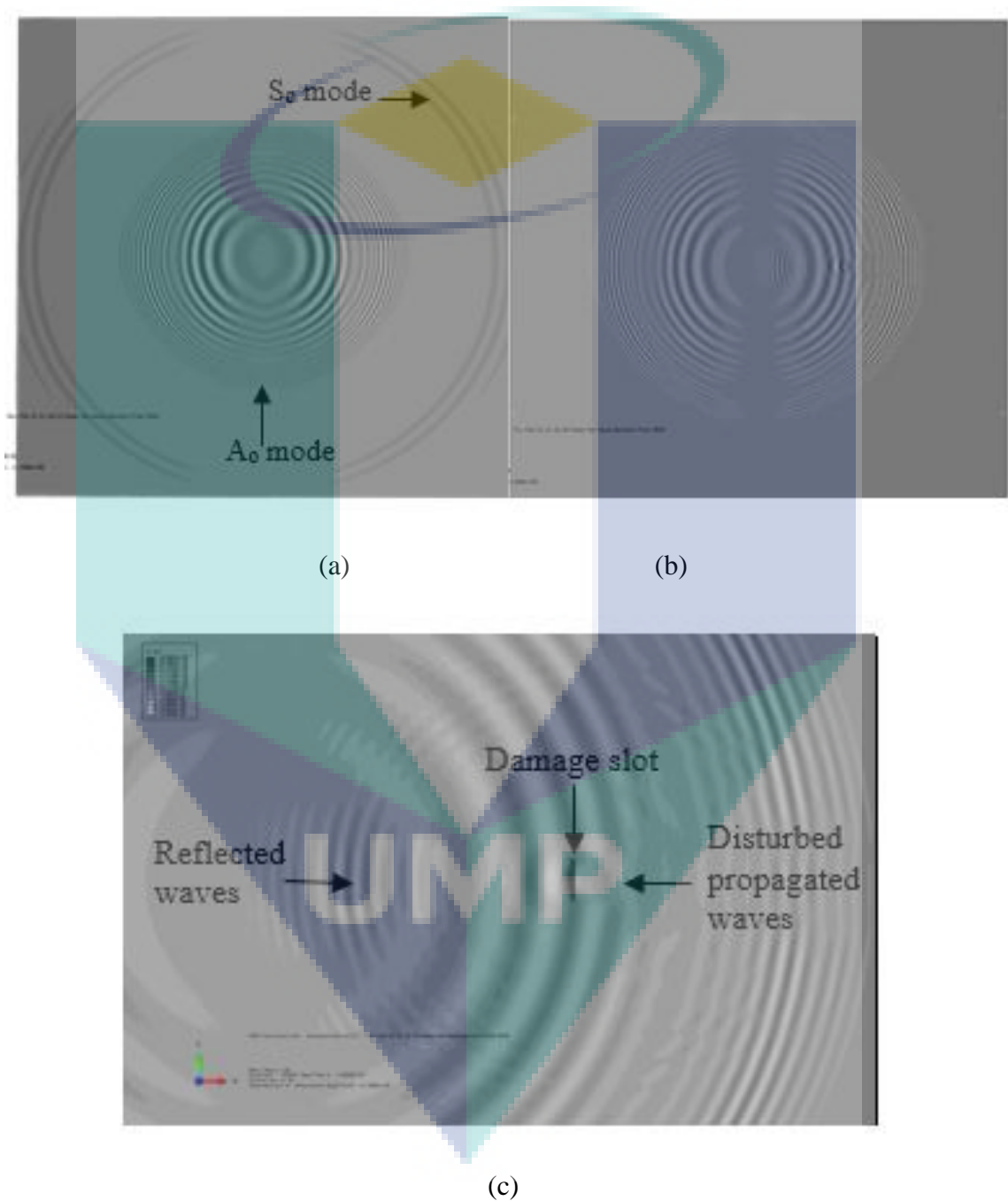
Figure 5.7   Visualisation of the wave propagation for (a) intact plate, (b) damaged plate and (c) close-up of the disturbed propagated wave for damaged plate

5.3.2 Damaged slot plate simulation

Through damaged slot with size of 2 x 0.2 cm was introduced at distance of 15 cm from the wave exciter. The same simulation set up was applied for damaged plate simulation. Two sensors were placed at the position for the pulse-echo and pitch-catch method and the arrangement of the sensors is shown in Figure 5.4 (b). The obtained time domain signals show a high degree of difference compared to the healthy plate for both configurations. Pulse-echo method shows the existing of one additional wave packet it is clearly shown in Figure 5.8 (a). It was assumed that the additional wave packet was resulted from the damaged slot reflection. The propagated waves were reflected back when they reached the damage slot. Figure 5.7 (c) clearly visualises this phenomenon. The velocity of the reflection waves was calculated and given as 2703 m/s, which is slower than the waves before reaching the defects. Short-time Fourier Transform (STFT) was implemented in order to study in detail of the waves interaction with defects. One additional contour was appeared right after the A_0 mode when comparing with spectrogram of the healthy plate, Figure 5.9 (a) with (b). This additional contour having the same value of frequency (200 kHz) with the A_0 mode. Thus, it is assumed that the reflection waves from the damage slot is also A_0 mode. Due to its nature which is mainly in-plane motion, the energy of S_o mode is fully attenuates when passing by the damage slot. It also effected by the large differences in mechanical impedances between the air and the solid due to through hole defects.

Different case for the pitch-catch method. The transmitted waves which is recorded by the sensor placed after the defects show an identical pattern with the healthy plate, but with a significant decrement of amplitude after propagating across the through hole defects. In addition, the delay for time of arrival (ToA) of the signals also affected by the introduction of defects for about 1.1 μs as presented in Figure 5.8 (b). This is due to the scattering of the waves around the defect. Spectrogram results in Figure 5.9 (c) also presents the delay of TOA for both modes. This is agreed with the time domain signal.

(a)

(b)
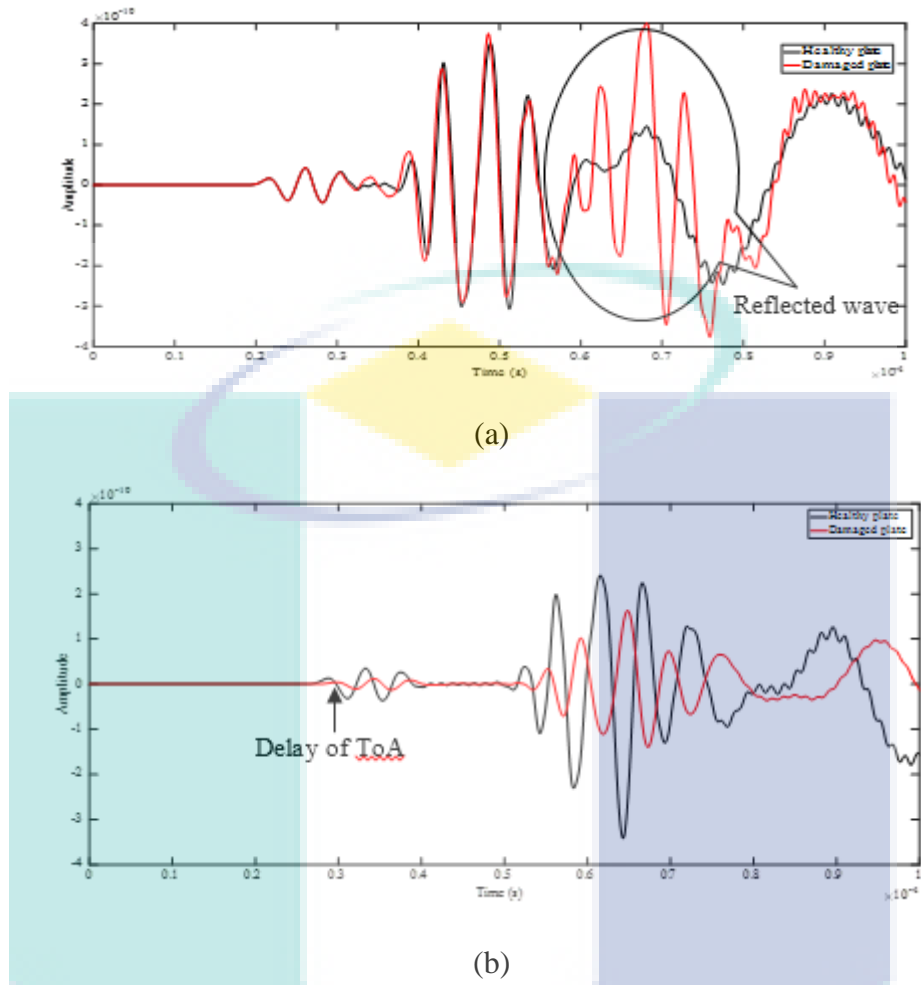
Figure 5.8   Direct comparison between healthy plate and damaged plate for (a) pulse-echo and (b) pitch-catch method

(a)

(b)

(c)
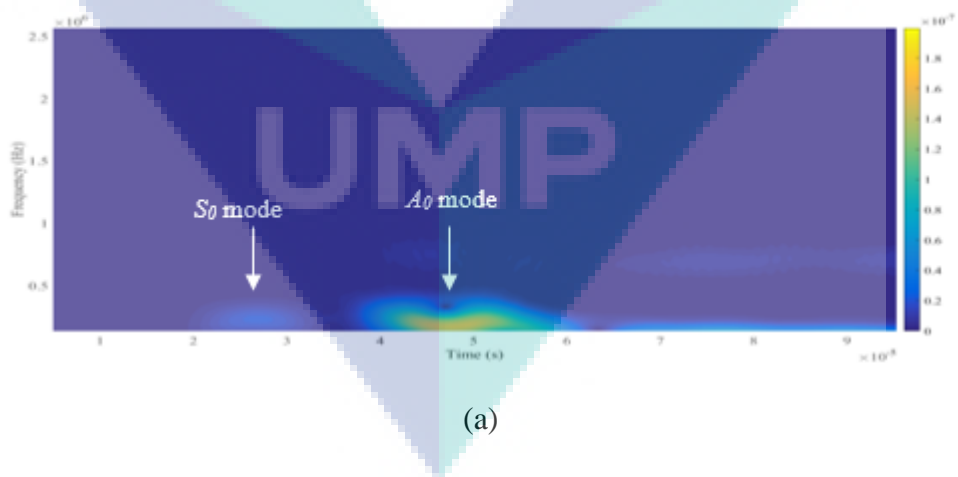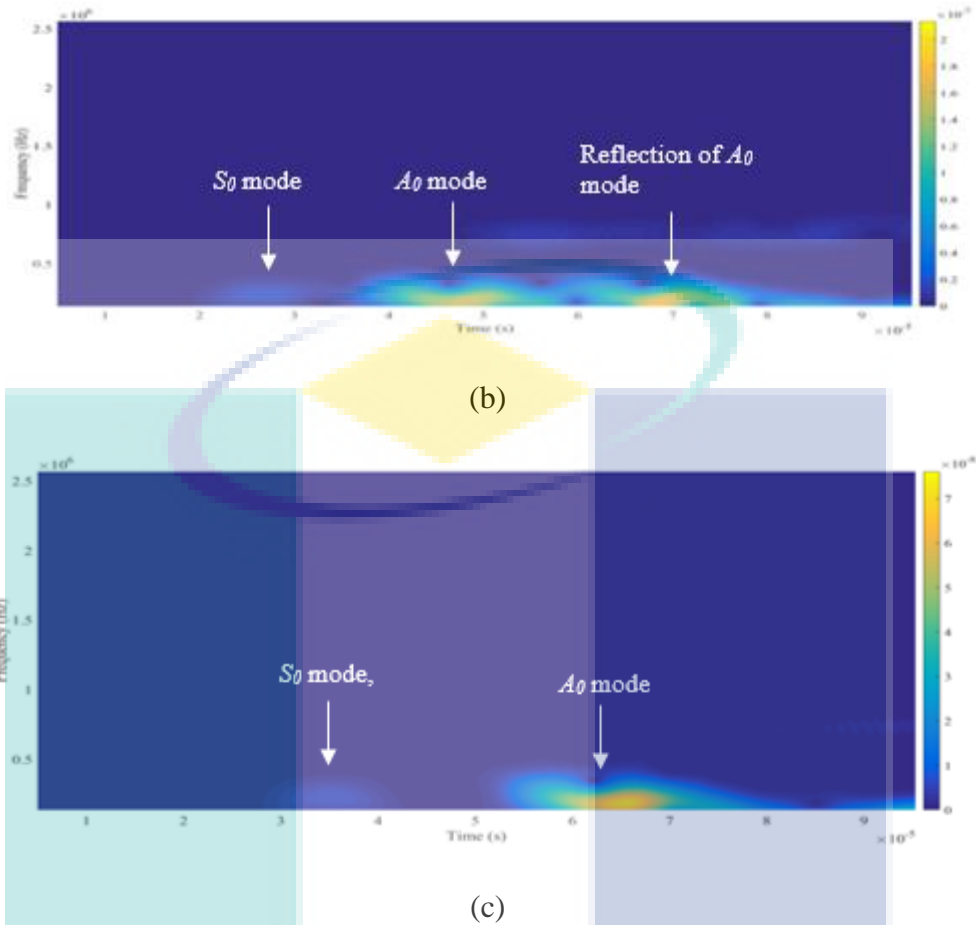
Figure 5.9   Spectrogram result for (a) healthy plate, (b) pulse-echo and (c) pitch-catch method

5.4   Chapter conclusions

Lamb waves was attracted by many researchers due to their advantages. However due to multimode and dispersive nature, well understanding of their behaviour is crucial for acquiring accurate results for SHM. Simulation work was performed in this present work for a better understanding of its interaction with the defects. It can be concluded that Lamb waves is one of the promising tool for the diagnostic analysis due to their sensitivity to any changes of the structural properties. Several types of signature can be extracted from the analysed signals which is can be used as an indicator for the condition monitoring of the structure. The additional wave packet is the main feature for the pulse-echo method. The attenuation in signal amplitude and delay of ToA are the features for the pitch-catch method. These defect signatures can be used as the diagnostic parameter for the metallic SHM system.

<center>**CHAPTER 6**</center>

<center>**FIBER BRAGG GRATING-BASED FABRY-PEROT INTERFEROMETER SENSOR FOR THE DETECTION OF DAMAGE IN THIN ALUMINUM PLATE**</center>

6.1   Introduction

Structural Health Monitoring (SHM) is definitely demanded to keep safely use of the structures during in service condition. It can be used to identify, locate and quantify the damage in engineering structures before the occurrence of failure (Worden, Farrar & Manson, 2007). Pulse-echo damage detection technique is one of SHM method, which utilized the understanding of Lamb waves propagation on thin structures. This method is a promising tool due to its advantages such as would be able to cover large areas from one single location (Khalili et al., 2016). Such systems would be cost-effective and efficient (SeJin Han, 2007). Besides that, the Lamb waves provide through-the-thickness interrogation which allows for internal defect detections in thin structures (Alleyne et al., 1992). A Piezoceramic Lead Zirconate Titanate (PZT) is a common actuator that is use to generate and receive Lamb waves.

In this research work, we utilize the combination of PZT and the Fiber Bragg Grating-based Fabry-Perot interferometer (FBG-FPI) for the acoustic pulse-echo Lamb waves measurement system. The FBG-FPIs were employed as edge filter with tunable laser source for Lamb wave detection (Rosenthal et al., 2011; Tsuda et al., 2010; Graham Wild et al., 2008). FBG-FPI offers several advantages such as such greater sensitivity, rapid response, small size, light weight, unperturbed by an electromagnetic interference, since the fiber is not electrically conductive and ease in implementing multiplexed or distributed sensors (Guangmin et al., 2017; B. Lee, 2003; Leng et al., 2003; Joseph L.

<center>87</center>

Rose et al., 2018; Vilchis-Rodriguez et al., 2014; A. Wada et al., 2012; G. Wild et al., 2008; Q. Zhang et al., 2017). Moreover, the physical structure of this sensor makes it suitable for embedment or surface mount installation. These advantages make FBG-FPI sensors ideal for the SHM evaluation.

6.2   Fiber Bragg grating-based intrinsic fabry-perot interferometer (**FBG-FPI**) sensor for dynamic strain sensing

Intrinsic FBG-FPI sensors are formed by using two identical FBG reflectors act as a parallel surface, perpendicular to the outer surfaces of the fiber. These two FBG reflectors are separated by a short local cavity at a determined distance. These reflectors lead to interference phenomenon due to multiple superposition of both reflected and transmitted beams (Vaughan, 2017). In this work, the FBG reflectors were fabricated by using phase mask technique with UV excimer laser. A photomask with two narrow slits was used to shape the laser beam to produce two short uniform gratings.

As illustrated in Figure 6.1 (a), the FBG-FPI comprises of two short uniform gratings, each grating had a length of 1 mm with a cavity length of 10 mm. Variations in the cavity longitudinal dimension, due to the applied strains, modify the cavity characteristics, which generates a broadband spectral variation with a periodic pattern, known as reflection spectrum. Changes in the cavity can be deduced by analyzing the reflected wavelength variation, and therefore, the strain arising from the Lamb wave can be determined.

Figure 6.1 (b) shows the reflection spectrum of the FBG-FPI sensor used in this study. The measured free spectral range (FSR) of the interference spectrum, 84 pm is in good agreement with the estimated FSR, 83 pm calculated using:

$$FSR = \frac{\lambda^2}{2nL} \tag{37}$$

in which λ is the central wavelength of the interferometric signal peak, n is the refractive index of the optical fiber with value of 1.444 and L is the cavity length. When the axial strain (ε) is applied to the fiber, the cavity length will change, therefore the FSR will change according to (57). Additionally, the central peak, λ will shift, according to:

$$\Delta\lambda = \beta\varepsilon\lambda \qquad\qquad (38)$$

where β is related to the stress optical effect.

Figure 6.1 (c) shows the shifted central peak when longitudinal strain is applied to the FPI-FBG sensor. As described by the equation, the FSR is inversely proportional to the cavity length. With a smaller FSR, the slope of every fringe edge is higher and hence the FBG-FPI is more sensitive to elastic wave (Atsushi Wada et al., 2009).

The gradient of the reflection curve plays an important role in the elastic wave detection. By launching a laser wavelength coincides with an edge of one of the interference fringes (See Figure 6.1 (b)), the reflected laser intensity will be modulated by impinging elastic wave on the sensor. Figure 6.1 (d) shows the calculated curve gradient in nm^{-1} based on the reflection curve in Figure 6.1 (b). Higher sensitivity can be achieved by aligning the laser to wavelength position with high curve gradient. The highest curve gradient is found to ~80nm^{-1} which is three times higher than that of a uniform grating sensor (Islam et al., 2015).

(a)

(b)

(c)

(d)
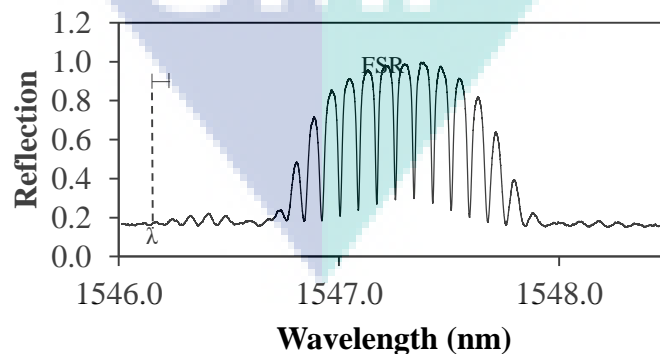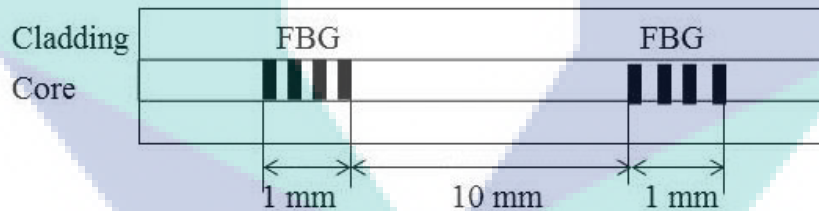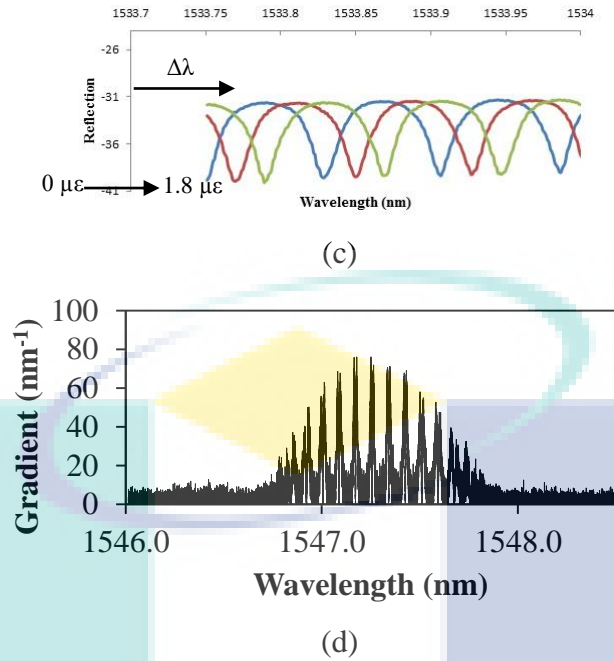
Figure 6.1   (a) Illustrative diagram, (b) reflection spectrum of the FBG-FPI sensor (c) the shifted of the reflection spectrum due to the longitudinal strain and (d) the calculated curve gradient of the FBG-FPI sensor.

6.3   Experimental setup

Experiment testing system for the proposed FBG-FPI sensor is shown in Figure 6.2. In this experiment, an aluminium plate with a dimension of 90 cm × 90 cm × 0.2 cm was used as the subject in this study. The mechanical properties of the plate are listed in Table 6.1. The plate was placed on styrofoam to produce stress-free boundary conditions. A 15 mm diameter of PZT actuator was positioned at the origin of the plate coordinate (0,0,0) as shown in Figure 6.2 (a). The excitation signal is generated by a digital function/arbitrary waveform generator. The excitation wave is a 6 kHz sine-burst wave with a peak-to-peak amplitude of 20 V. The excitation frequency of 6 kHz was chosen because it was very close to the resonant frequency of PZT actuator and therefore maximize the signal-to-noise ratio and increase the wave propagation range. The actuated Lamb wave has induced the strain when propagating through the plate specimen. The tunable laser source was launched concurrently for the strain sensing by the two FBG-FPI sensors (T1 and T2) which is mounted at x_1= 8 cm and x_2= 23 cm, respectively. This configuration is illustrated in Figure 6.2 (a). The reflected optical signal is then converted into an electrical signal by a photodetector and recorded using a digital oscilloscope at the sampling frequency of 125 kHz. The schematic diagram for the generation, reception and measurement is shown in Figure 6.2 (b).

Table 6.1   Mechanical properties of the aluminum plate

Density (kg/m^3)	Young's Modulus, E (GPa)	Poisson's ratio
2580	72.7	0.33

(a)

(b)
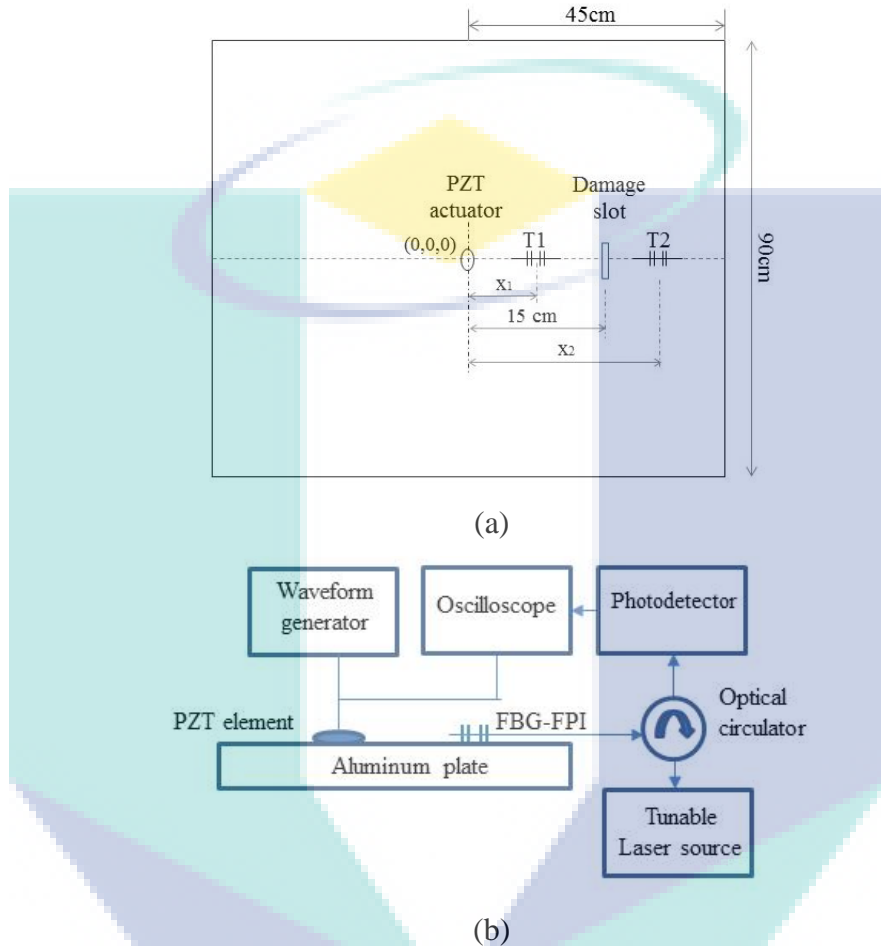
Figure 6.2   Schematic diagram of the (a) aluminum plate with the damage slot and (b) proposed diagnostic system.

The same plate was used in this comparative test for intact and damage conditions to prove the applicability of the FBG-FPI in acoustic pulse-echo Lamb wave technique. The Lamb wave signals were measured at two conditions: (i) on the intact area, as reference; and (ii) on the damaged area. The same FBG-FPI sensors were used for all measurements throughout the experiment. The waveform measurement on an undamaged aluminum plate was performed first before the damage slot was created. The damage is introduced in the form of a through rectangular slot, size of 2 cm × 0.2 cm at a distance of 15 cm from the actuator.

6.4 Results and discussion

The excitation signal is shown in Figure 6.3 (a) and its short-time Fourier transform (STFT) spectrogram is depicted in Figure 6.3 (b). It shows that the central frequency of the excitation signal is at 6 kHz. Meanwhile, the measured responses from the intact area by FBG-FPI sensors are presented in Figure 6.4. The signal characteristic of the intact plate was used as baseline data for damage identification procedure. Detail analysis for reference signals is necessary to avoid false alarm in damage detection.
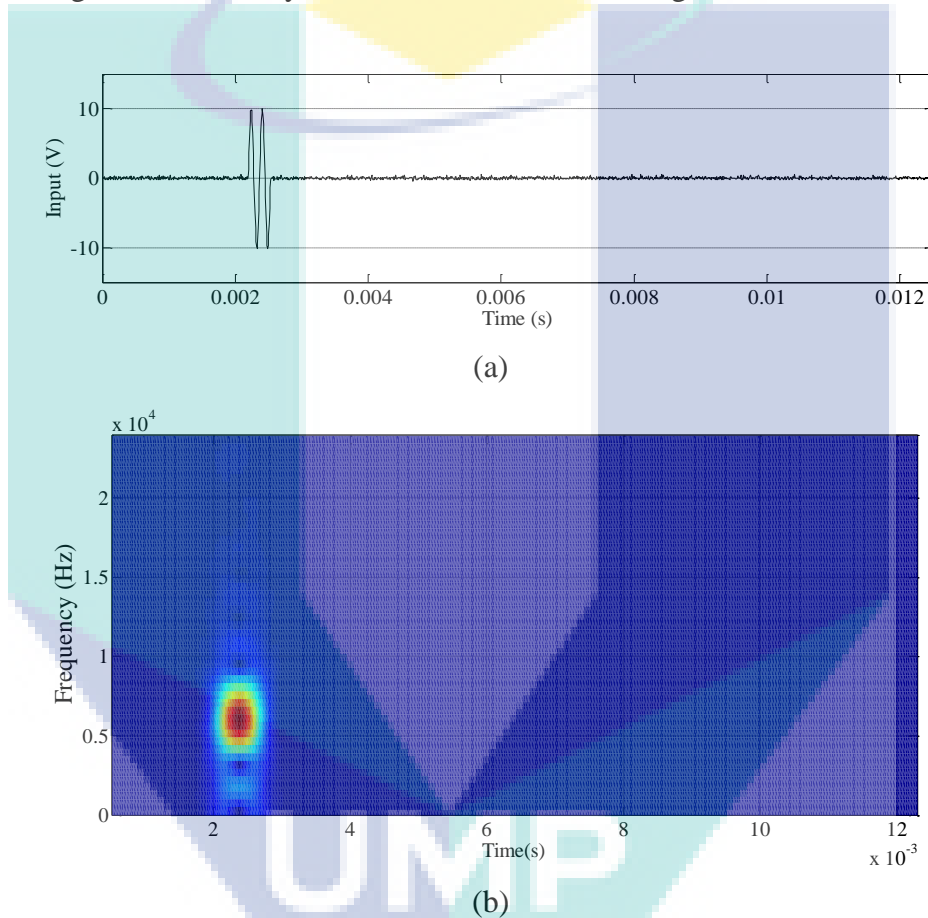
Figure 6.3   (a) Two-cycle sine-burst input signal and (b) STFT spectrogram of the input signal

Time domain signal acquired by T1 sensor indicates only one major wave packet as presented in Figure 6.4 (a). This is due to the fact that no reflection from all of the edges since the distance of the edges were far enough from the T1 sensor. On the other hand, the time domain recorded by T2 sensor appeared differently as presented in Figure 6.4 (b). One additional wave packet was observed after the major wave packet. That additional wave packet was resulting from the reflection of the edge boundary. The short

distance away from one of the edge boundary at about 22 cm makes this reflected wave detected by the T2 sensor.
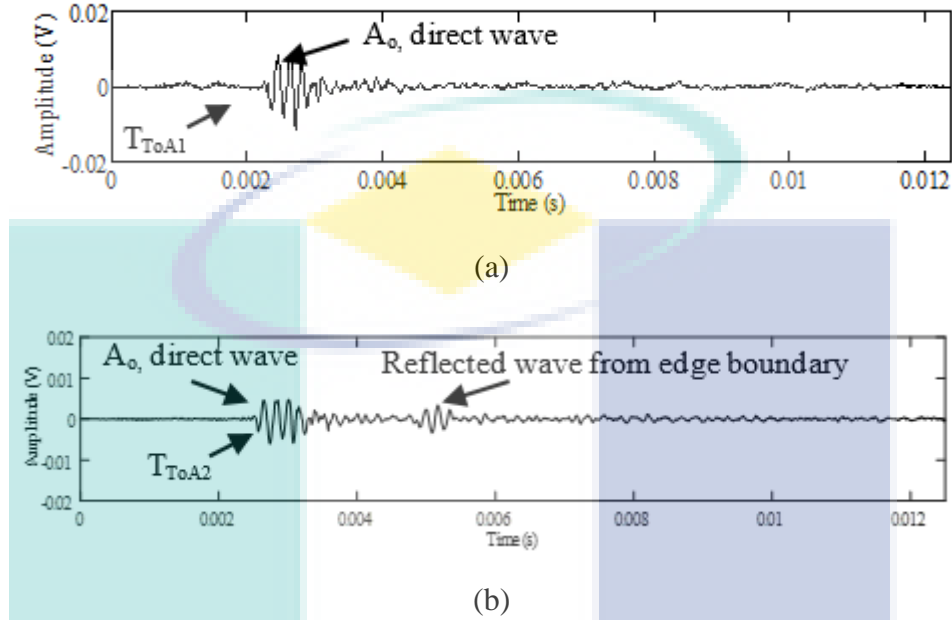
Figure 6.4   The detected signal for an intact plate measured by (a) T1 at x_1=8 cm and (b) T2 at x_2=23 cm

In order to identify the correct excited modes of Lamb wave in the aluminum plate, dispersion curve was generated. For this study, we use PACshare Dispersion Curve. Figure 6.5 (a) shows the calculated dispersion curves of all the excited modes in a 2 mm-thick aluminum plate. Group velocity (c_g) and frequency are two important parameters in identifying the types of excited modes during the experimentation. In the experiment, the actuation frequency was 6 kHz and the corresponding group velocity of the wave can be empirically determined from the distance between the two sensors (d) and time of flight (ToF). Here, time of flight, T_{ToF} is given by

$$T_{ToF} = T_{ToA2} - T_{ToA1}$$ (39)

where T_{TOA2} and T_{TOA1} is the time of arrival of the waves at sensor T2 and T1, respectively. For the data in Figure. 6.4, the T_{ToF} is 0.2 ms and the associated velocity of the wave that had travelled for a distance of 15 cm (x_2-x_1) is 0.75 km/s. With referral to the theoretical dispersion curve in Figure 6.5 (b), it coincides with A_o mode curve. It can be concluded that the direct wave actuated by the PZT actuator was dominantly A_o mode.

(a)

(b)
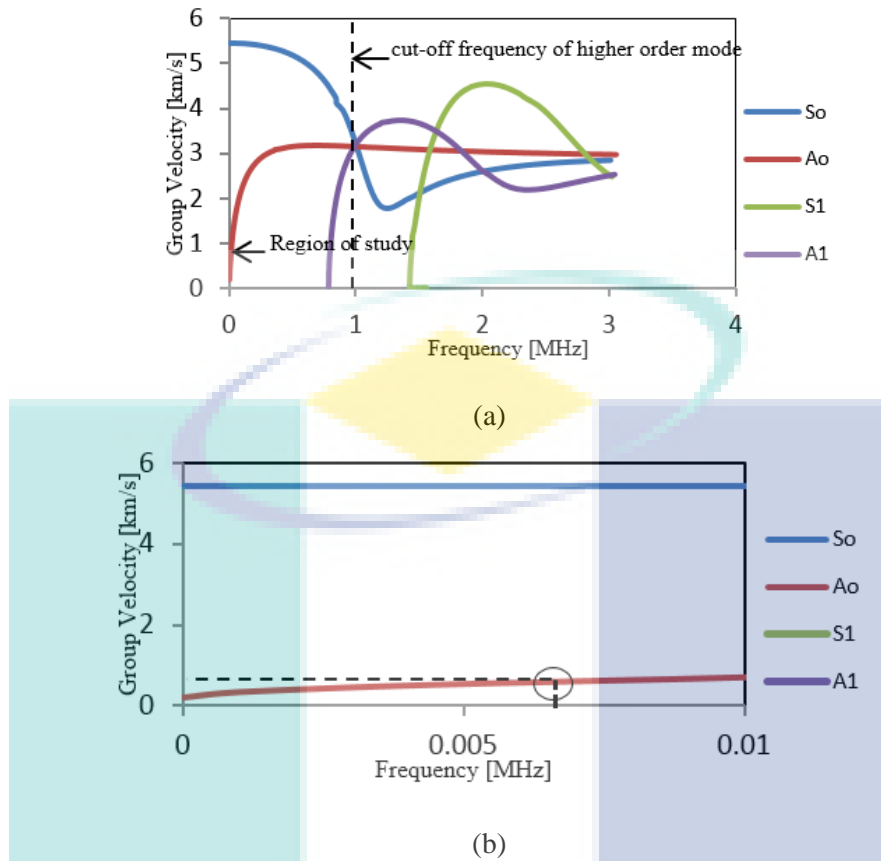
Figure 6.5   Theoretical dispersion curve of group velocity against frequency in aluminum plate with thickness of 2 mm (a) for all modes and (b) selected range of the present study.

When the same actuation is applied to the damaged plate, the A_0 wave propagates crossing entire plate before reaching the damage slot. The T1 sensor has successfully detected the reflected wave packet due to damage, while the rest of the wave was transmitted passing the damage before acquired by T2 sensor. The corresponding responses are shown in

Figure 6.6 (a) and (b), respectively.

Figure 6.6 (a) shows the additional of a new wave packet due to damage reflection started at about 3.15 ms which occurred after the direct wave packet.

On the contrary for waveform measured at T2. Only one wave packet was appeared for the damaged plate. There is no wave passing through the damage slot in the perpendicular direction due to large impedance mismatch between the air and the solid

media which led to difficulty for the wave to propagate .The wave was scattered around the damage slot before reaching T2 sensor as shown in

Figure 6.6 (c). This phenomenon weakens the transmitted wave and produces no edge boundary reflection as recorded at intact plate. Based on the ToF calculation, the wave travelled on damaged plate was delayed by ~64 μs compared to intact plate due to disturbance at the defect.

From the above findings, it is interesting to note that the FBG-FPI sensor is capable in detecting Lamb waves for the damage detection. It can be concluded that there are Any changes of the structural properties affected the propagation of the Lamb waves and the proposed FBG-FPI sensor was able to detect and measure that information. This is based on a high degree of visible correlation for intact and damaged plate waveforms.

(a)

(b)

(c)
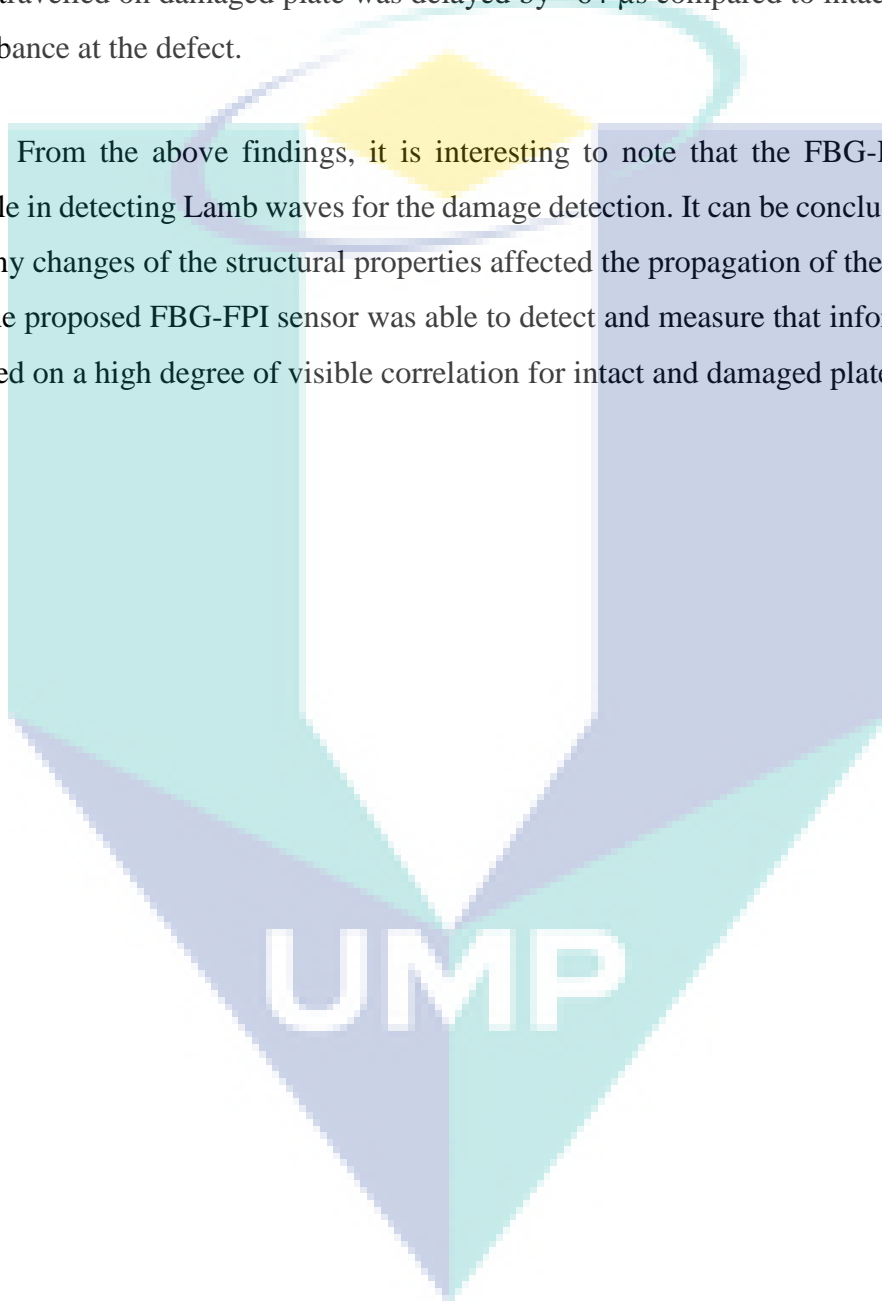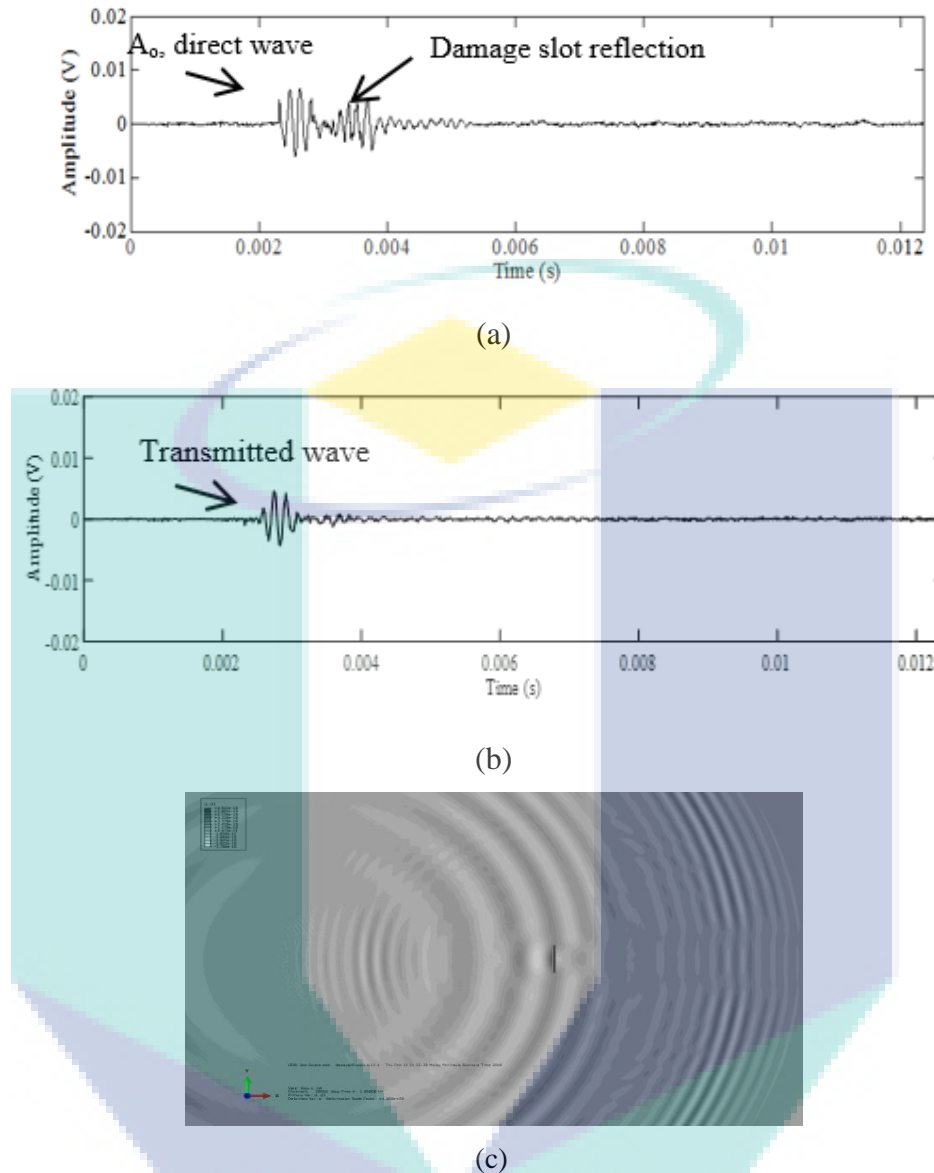
Figure 6.6   The detected signal for a damaged plate by (a) T1 at x_1=8 cm and (b) T2 at x_2=23 cm and (c) close-up simulation result for the scattered wave around the defect

The above time domain waveform was then analysed using STFT analysis in order to study in details the effect of damage slot to the Lamb waves propagation using FBG-FPI sensor. STFT, making use of a Gaussian function with time duration of 1 ms as the window function, is applied to map these signals into the time-frequency domain. The associated spectrograms are shown in Figure 6.7 and Figure 6.8. Based on STFT results of the intact plate, upon actuation, a direct wave at the actuating frequency is induced by the PZT and it propagates along the plate and received by S1 as depicted in Figure 6.7

(a). The wave continues its propagation until it reaches S2 before the edge of the plate and reflected back as the reflection wave. The result is presented in Figure 6.7 (b).

The spectrogram provides a better visualisaton of the signal for the damaged lot as presented in Figure 6.8 (a). An additional wave packet as presented in Figure 6.8 (a). It is validated that from the reflection of the damage slot since having an identical frequency to the direct wave. Moreover, according to the theoretical group velocity dispersion curves as presented in Figure 6.5 (b), the gradient of the curve is almost constant which indicate the extremely low dispersion of the A_0 in selected frequency region. It is therefore proven that the additional wave packet exist in the measured signal is the reflected wave from the damaged slot area, not from the dispersion effects. Mode conversion phenomenon is not happened at this propagation path.

Other than that, it was observed that the intensity of the second wave packet was lower compared to direct wave. This can be attributed to the attenuation loss and low wave reflectance from the damage area. Figure 6.8 (b) is the spectrogram for the waveform measured at S2. Only one wave packet was appeared due to energy loss after scattering around the defects.
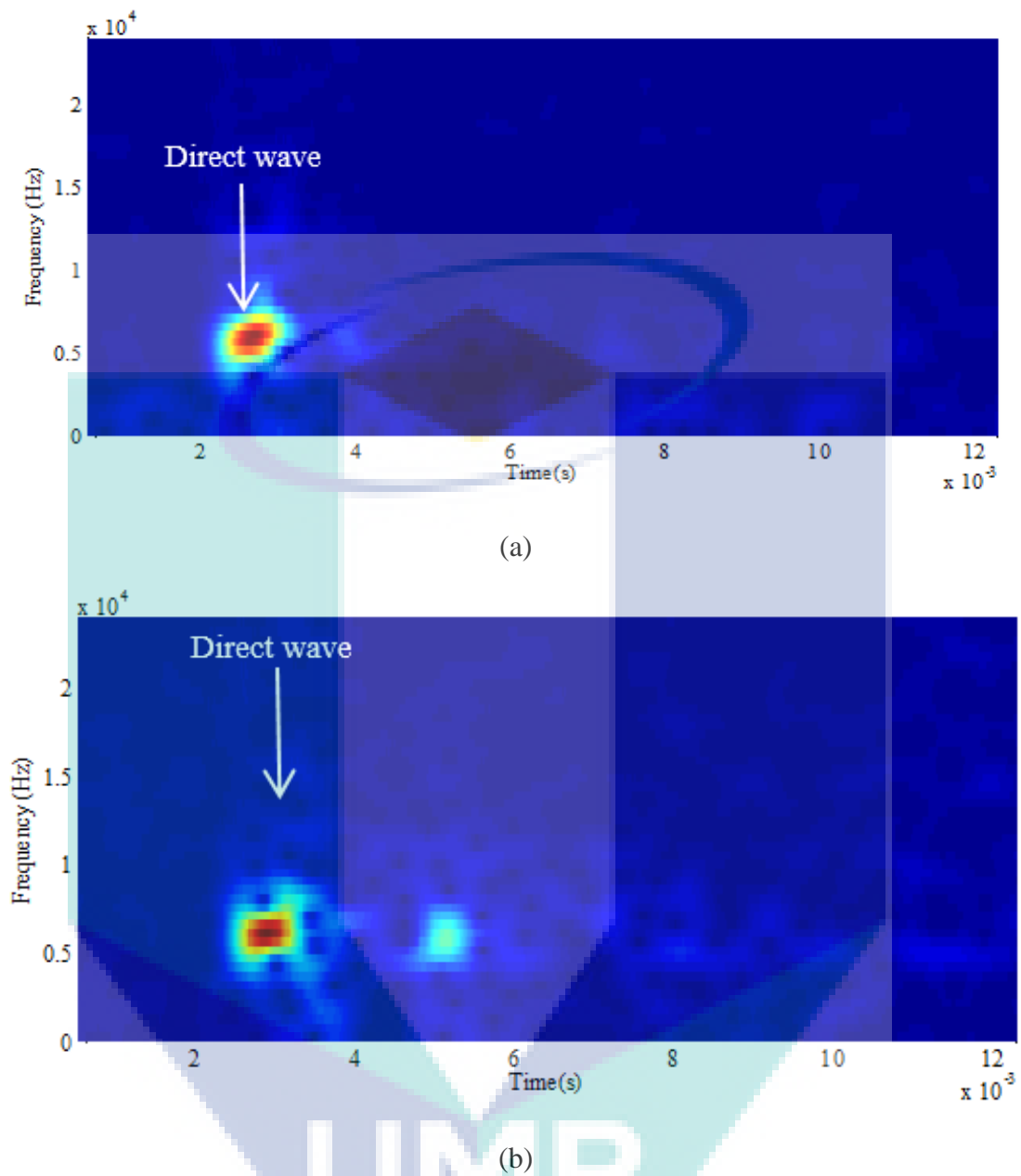
Figure 6.7   STFT spectrogram results for intact area measured by (a) S1 at x_1=8 cm and (b) S2 at x_2=23 cm
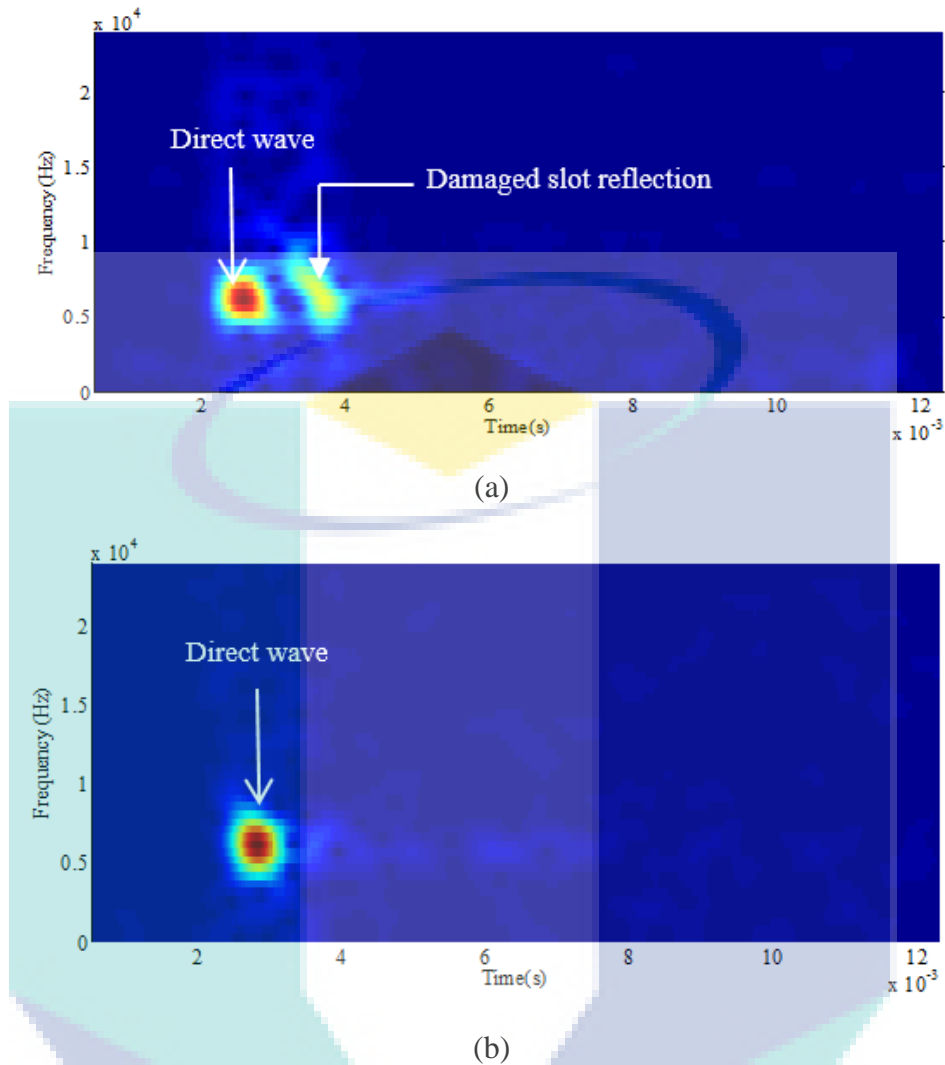
Figure 6.8　　STFT spectrogram results for damaged area measured by (a) S1 at x_1=8 cm and (b) S2 at x_2=23 cm

　　　　Further attempt was made to validate the reflected wave from the damage slot. The validation analysis is just adjusting the position of the S1 at two different distance that is x_1=2 cm and 5 cm while maintaining the same position for S2 at x_2=23 cm. The associated time-domain waveform and STFT spectrogram are presented in Figure 6.9 and Figure 6.10, respectively.

　　　　Similarly, an additional wave packet is observed due to the existence of damage slot. This appearance is strongly believe due to the superimposed effect. The propagation time is too short for mode separation due to the short distance between actuator and the S1 sensor. All the time-domain and time-frequency domain results for this study are in accordance to each other and it has proved that the strain induced in the plate by the Lamb waves was successfully measured by the proposed FBG-FPI sensors.
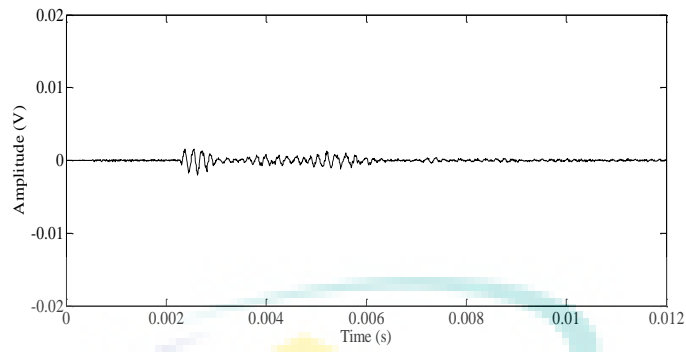
(a)

Figure 6.9   Detected signal for damaged area by S1 at two different positions (a) x_1=2 cm and (b) x_1=5 cm
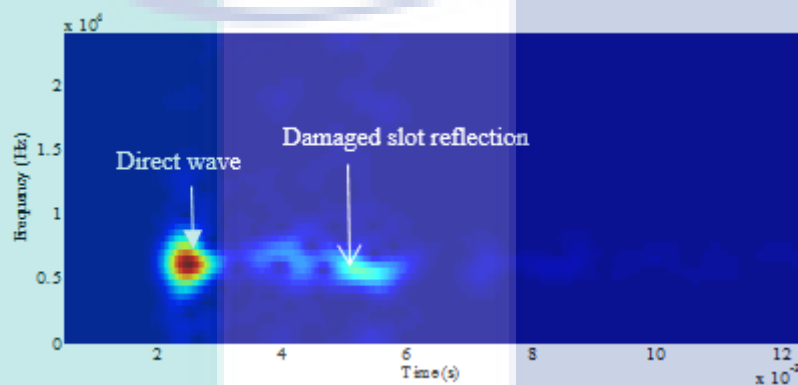
(a)
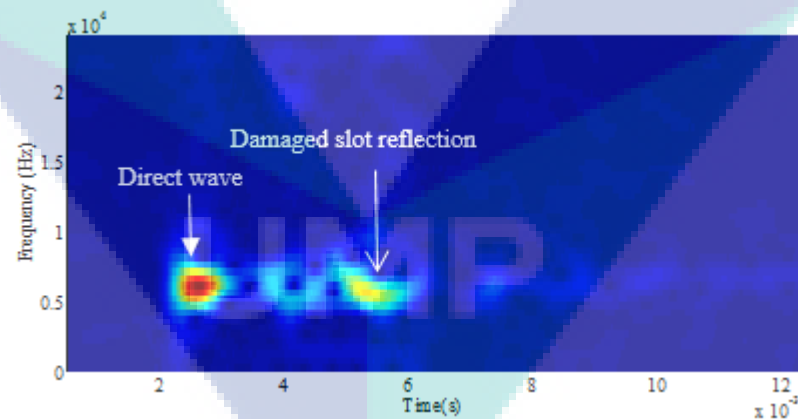
(b)

Figure 6.10   STFT spectrogram results for damaged area measured by S1 at two different positions (a) x_1=2 cm and (b) x_1=5 cm

6.5   Chapter conclusion

A diagnostic system is developed using FBG-FPI sensor for damage detection of an aluminium plate. The healthy waveforms were used as the reference waveforms for the health status analysis. Additional wave packet, reduction in amplitude and delay in time

of arrival are the main parameters that were extracted from the comparison analysis between healthy and damaged area waveforms. These findings are in accordance with the time-frequency analysis. In conclusion, our finding indicates that the FBG-FPI system is an effective tool for damage detection in metallic structure over traditional sensor types. It is very sensitive, highly reliable, fast response and applicable for structural health monitoring. Their unique advantages will encourage their use in challenging inspection problems in the future.
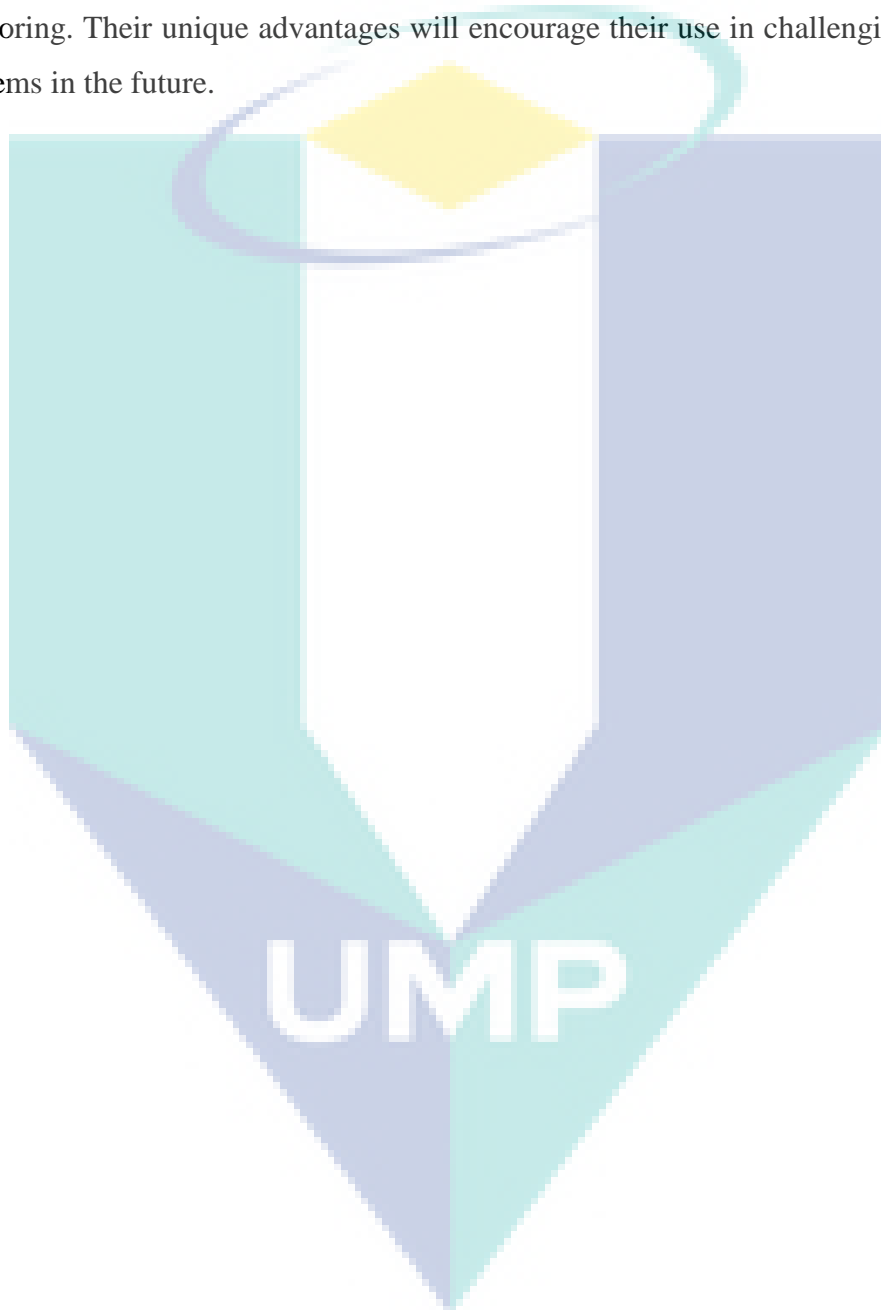
CHAPTER 7

CONCLUSION

This project has been successfully done within the given time frame. Throughout the project period, several output has been achieved, which is; 4 publications, 2 papers for conferences, 1 filed patent, 3 awards for innovations and 2 postgraduate students (1 graduated Master and 1 final semester Ph.D.).

In the meantime, all objectives for the project have been achieved. The first and second objective, which is the study of the damage growth inside a thin-walled composite structure and; the correlation of the progressive damages progress with the signals from the FBG spectra and AE signal parameters, have been explained thoroughly in chapter 5 and 6. The investigation were focused on the simulation of lamb wave propagation and its relation to the damages in this structures. Several experiments also have been conducted in order to validate the findings. The outcome gives us better understanding of the signal characteristics of the lamb waves, prior to the application of FBG sensor network for the structural health monitoring procedures. Meanwhile, the FBG-FPI system has shown significant sensitivity for detecting cracks in thin structure.

The third objective of the project, that is the algorithm development has been explained in details, in chapters 3 and 4. The CC-LSL algorithm has been proved to give the result below 5% error. Meanwhile, a post-processing analysis was also developed to solve the damage detection in the FRP composite by using matched filtering of centre of energy method. The time of arrival of the wave is used as an indicator for the condition of the structure. The delay in time significantly indicated that there is flaw in a thin composite structure.

REFERENCES

Abdo, M. (2014). *Structural Health Monitoring, History, Applications and Future. A Review Book.*

Ahmad, Z. A. (2011). *Numerical Simulations of Lamb Waves in Plates Using a Semi-Analytical Finite Element Method.* (PhD).

Aljets, D., Chong, A., Wilcox, S., & Holford, K. (2010). Acoustic emission source location in plate-like structures using a closely arranged triangular sensor array. *Journal of Acoustic Emission, 28*, 85-98.

Alleyne, D. N., & Cawley, P. (1992). The interaction of Lamb waves with defects. *IEEE Transactions on Ultrasonics, Ferroelectrics, and Frequency Control, 39*(3), 381-397.

Allwood, G., Wild, G., Lubansky, A., & Hinckley, S. (2015). A highly sensitive fiber Bragg grating diaphragm pressure transducer. *Optical Fiber Technology, 25*, 25-32.

Ambrozinski, L., Stepinski, T., Packo, P., & Uhl, T. (2012). Self-focusing Lamb waves based on the decomposition of the time-reversal operator using time–frequency representation. *Mechanical Systems and Signal Processing, 27*, 337-349.

Askins, C. G., Putnam, M. A., & Friebele, E. J. (1995). *Instrumentation for interrogating many element fiber bragg grating arrays.* Paper presented at the Smart Structures & Materials' 95.

Baid, H., Schaal, C., Samajder, H., & Mal, A. (2015). Dispersion of Lamb waves in a honeycomb composite sandwich panel. *Ultrasonics, 56*, 409-416.

Baker, A. A. (2004). *Composite materials for aircraft structures*: AIAA.

Balaji, R., & Sasikumar, M. (2016). Structural health monitoring (SHM) system for polymer composites: A review. *Indian Journal of Science and Technology; Volume 9, Issue 41, November 2016.*

Baochun, X., Shenfang, Y., Mulan, W., & Lei, Q. (2015). Determining impact induced damage by lamb wave mode extracted by EMD method. *Measurement, 65*, 120-128.

Ben, B. S., Ben, B. A., Vikram, K. A., & Yang, S. H. (2013). Damage identification in composite materials using ultrasonic based Lamb wave method. *Measurement, 46*(2), 904-912.

Carboni, M., Gianneo, A., & Giglio, M. (2015). A Lamb waves based statistical approach to structural health monitoring of carbon fibre reinforced polymer composites. *Ultrasonics, 60*, 51-64.

Castaings, M., & Cawley, P. (1996). The generation, propagation, and detection of Lamb waves in plates using air‐coupled ultrasonic transducers. *The Journal of the Acoustical Society of America, 100*(5), 3070-3077.

Caucheteur, C., Chah, K., Lhommé, F., Blondel, M., & Mégret, P. (2004). Autocorrelation demodulation technique for fiber Bragg grating sensor. *IEEE Photonics Technology Letters, 16*(10), 2320-2322.

Chen, F., Guo, L., Xiao, L., & Liu, L. (2010). *The principle and application of the laser ultrasound non-destructive testing technology.* Paper presented at the SPIE 7749, 2010 International Conference on Display and Photonics.

Chen, W., & Dong, X. (2012). Modification of the wavelength-strain coefficient of FBG for the prediction of steel bar corrosion embedded in concrete. *Optical Fiber Technology, 18*(1), 47-50.

Cho, Y. S. (2003). Non-destructive testing of high strength concrete using spectral analysis of surface waves. *NDT & E International, 36*(4), 229-235.

Croxford, A. J., Wilcox, P. D., Drinkwater, B. W., & Konstantinidis, G. (2007). Strategies for guided-wave structural health monitoring. *Proceedings of the Royal Society A: Mathematical, Physical and Engineering Science, 463*(2087), 2961.

De Pauw, B., Goossens, S., Geernaert, T., Habas, D., Thienpont, H., & Berghmans, F. (2017). Fibre Bragg Gratings in Embedded Microstructured Optical Fibres Allow Distinguishing between Symmetric and Anti-Symmetric Lamb Waves in Carbon Fibre Reinforced Composites. *Sensors (Basel), 17*(9).

Di Sante, R. (2015). Fibre optic sensors for structural health monitoring of aircraft composite structures: Recent advances and applications. *Sensors, 15*(8), 18666-18713.

Diligent, O. (2003). *Interaction Bewtween Fundamental Lamb Modes and Defects in Plates.* Imrerial College London.

Eaton, M. J., Pullin, R., & Holford, K. M. (2012). Acoustic emission source location in composite materials using Delta T Mapping. *Composites Part A: Applied Science and Manufacturing, 43*(6), 856-863.

Ezbiri, A., Kanellopoulos, S., & Handerek, V. (1998). High resolution instrumentation system for fibre-Bragg grating aerospace sensors. *Optics communications, 150*(1), 43-48.

Fedorov, A., Lazarev, V., Makhrov, I., Pozhar, N., Anufriev, M., Pnev, A., & Karasik, V. (2015). *Structural monitoring system with fiber Bragg grating sensors: implementation and software solution.* Paper presented at the Journal of Physics: Conference Series.

Fernando, C., Bernier, A., Banerjee, S., Kahandawa, G. G., & Epparchchi, J. (2017). An Investigation of the Use of Embedded FBG Sensors to Measure Temperature and Strain Inside a Concrete Beam During the Curing Period and Strain Measurements under Operational Loading. *Procedia Engineering, 188*, 393-399.

Frieden, J., Cugnoni, J., Botsis, J., & Gmur, T. (2012). Low energy impact damage monitoring of composites using dynamic strain signals from FBG sensors-Part I: Impact detection and localization. *Composite Structures, 94*(2), 438-445.

Fu, T., Liu, Y., Lau, K. T., & Leng, J. (2014). Impact source identification in a carbon fiber reinforced polymer plate by using embedded fiber optic acoustic emission sensors. *Composites Part B: Engineering, 66*, 420-429.

Gayan C. KAHANDAWA, J. E., Hao WANG, and K. T. LAU. (2012). Use of FBG Sensors for SHM in Aerospace Structures *Photonic Sensors, Vol. 2*(No. 3).

Geng, X., Jiang, M., Gao, L., Wang, Q., Jia, Y., Sui, Q., . . . Li, D. (2017). Sensing characteristics of FBG sensor embedded in CFRP laminate. *Measurement, 98*, 199-204.

Ghosh, T., Kundu, T., & Karpur, P. (1998). Efficient use of Lamb modes for detecting defects in large plates. *Ultrasonics, 36*(7), 791-801.

Giurgiutiu, V. (2005). Tuned Lamb Wave Excitation and Detection with Piezoelectric Wafer Active Sensors for Structural Health Monitoring. *Journal of Intelligent Material Systems and Structures, 16*(4), 291-305.

Giurgiutiu, V. (2014). *Structural Health Monitoring with Piezoelectric Wafer Active Sensors* (2nd ed.): Academic Press.

Gregory, R. (2001). *Laser shearography inspection for aircraft and space structures* (Vol. 43).

Grondel, S., Paget, C., Delebarre, C., Assaad, J., & Levin, K. (2002). Design of optimal configuration for generating A0 Lamb mode in a composite plate using piezoceramic transducers. *The Journal of the Acoustical Society of America, 112*(1), 84-90.

Guangmin, Z., Weihang, G., Gangbing, S., & Yue, S. (2017). An imaging algorithm for damage detection with dispersion compensation using piezoceramic induced lamb waves. *Smart Materials and Structures, 26*(2), 025017.

Guo, N., & Cawley, P. (1993a). The interaction of Lamb waves with delaminations in composite laminates. *The Journal of the Acoustical Society of America, 94*(4), 2240-2246.

Guo, N., & Cawley, P. (1993b). Lamb wave propagation in composite laminates and its relationship with acousto-ultrasonics. *NDT & E International, 26*(2), 75-84.

Guo, Z., Achenbach, J. D., & Krishnaswamy, S. (1997). EMAT generation and laser detection of single lamb wave modes. *Ultrasonics, 35*(6), 423-429.

Guojun, H., Changben, W., Shiyuan, C., & Guowei, Y. (2014). Reconstruction of structural damage based on reflection intensity spectra of fiber Bragg gratings. *Measurement Science and Technology, 25*(12), 125109.

Gutkin, R., Green, C., Vangrattanachai, S., Pinho, S., Robinson, P., & Curtis, P. (2011). On acoustic emission for failure investigation in CFRP: Pattern recognition and peak frequency analyses. *Mechanical systems and signal processing, 25*(4), 1393-1407.

H Díaz Valdés, S., & Soutis, C. (2002). *Real-time non-destructive evaluation of fibre composite laminates using low-frequency Lamb waves* (Vol. 111).

Habib, F., Martinez, M., Artemev, A., & Brothers, M. (2013). Structural health monitoring of bonded composite repairs – A critical comparison between ultrasonic Lamb wave approach and surface mounted crack sensor approach. *Composites Part B: Engineering, 47*, 26-34.

Hafizi, Z., & Epaarachchi, J. (2015). *Dynamic response and signal to noise ratio investigation of nir-fbg dynamic sensing system for monitoring thin-walled composite plate.* Paper presented at the IOP Conference Series: Materials Science and Engineering.

Hafizi, Z. M., Epaarachchi, J., & Lau, K. T. (2015). Impact location determination on thin laminated composite plates using an NIR-FBG sensor system. *Measurement, 61*, 51-57.

Hailu, B., Gachacan, A., Hayward, G., & McNab, A. (1999, 17-20 Oct. 1999). *Embedded piezoelectric transducers for structural health monitoring.* Paper presented at the 1999 IEEE Ultrasonics Symposium. Proceedings. International Symposium (Cat. No.99CH37027).

Hayashi, T., & Kawashima, K. (2003). Single Mode Extraction from Multiple Modes of Lamb Wave and Its Application to Defect Detection. *JSME International Journal Series A Solid Mechanics and Material Engineering, 46*(4), 620-626.

Haywood, J., Coverley, P. T., Staszewski, W. J., & Worden, K. (2005). An automatic impact monitor for a composite panel employing smart sensor technology. *Smart Materials and Structures, 14*(1), 265.

Hiroshi, T., Nobuyuki, T., Kei, U., & Junji, T. (2004). Impact damage detection in CFRP using fiber Bragg gratings. *Smart Materials and Structures, 13*(4), 719.

Hoon, S., Gyuhae, P., Jeannette, R. W., Nathan, P. L., & Charles, R. F. (2004). Wavelet-based active sensing for delamination detection in composite structures. *Smart Materials and Structures, 13*(1), 153.

Horace Lamb, F. R. S. (1917). On waves in an elastic plate. *Proceedings of the Royal Society of London. Series A, 93*(648), 114.

Hosten, B., Castaings, M., Tretout, H., & Voillaume, H. (2001). Identification of composite materials elastic moduli from Lamb wave velocities measured with single sided, contactless ultrasonic method. *AIP Conference Proceedings, 557*(1), 1023-1030.

Hu, N., Shimomukai, T., Fukunaga, H., & Su, Z. (2008). Damage Identification of Metallic Structures Using A0 Mode of Lamb Waves. *Structural Health Monitoring, 7*(3), 271-285.

Huang, Jing, W., Liu, K., Zhang, Y., & Peng, G. (2007). Demodulation of fiber Bragg grating sensor using cross-correlation algorithm. *IEEE Photonics Technology Letters, 19*(9/12), 707-707.

Huang, Zhang, W., Zhen, T., Zhang, F., & Li, F. (2014). A cross-correlation method in wavelet domain for demodulation of FBG-FP static strain sensors. *IEEE Photonics Technology Letters, 26*(16), 1597-1600.

Iacoviello, F., Reis, L., Fonte, M., Freitas, M., Infante, V., & Gholizadeh, S. (2016). A review of non-destructive testing methods of composite materials. *Procedia Structural Integrity, 1*, 50-57.

Ianniello, J. (1982). Time delay estimation via cross-correlation in the presence of large estimation errors. *IEEE Transactions on Acoustics, Speech, and Signal Processing, 30*(6), 998-1003.

Innes, M., Davis, C., Rosalie, C., Norman, P., & Rajic, N. (2017). Acoustic Emission Detection and Characterisation Using Networked FBG Sensors. *Procedia Engineering, 188*, 440-447.

Islam, M. R., Ali, M. M., Lai, M., Lim, K., Gunawardena, D. S., Machavaram, V. R., & Ahmad, H. (2015). Wide-range in-fibre Fabry-Perot resonator for ultrasonic sensing. *IET Optoelectronics, 9*(3), 136-140.

Jayaraman, C., Krishnamurthy, C. V., & Balasubramaniam, K. (2009). Higher Order Modes Cluster (HOMC) Guided Waves—A New Technique For NDT Inspection. *AIP Conference Proceedings, 1096*(1), 121-128.

Jha, R., Kim, I., & Widana-Gamage, D. (2010). Investigation of Incident Lamb Wave Parameters on Detection of Composite Delamination. (44168), 675-683.

Jia, X. (1997). Modal analysis of Lamb wave generation in elastic plates by liquid wedge transducers. *The Journal of the Acoustical Society of America, 101*(2), 834-842.

Joseph, L. R. (2011, 15 April 2011). *The upcoming revolution in ultrasonic guided waves In: Nondestructive characterization for composite materials, aerospace engineering, civil infrastructure, and homeland security.* Paper presented at the SPIE Smart Structures and Materials + Nondestructive Evaluation and Health Monitoring,, San Diego.

Kahandawa, G. C., Epaarachchi, J., Wang, H., Canning, J., & Lau, K. T. (2013). Extraction and processing of real time strain of embedded FBG sensors using a fixed filter FBG circuit and an artificial neural network. *Measurement, 46*(10), 4045-4051.

Kahandawa, G. C., Epaarachchi, J., Wang, H., & Lau, K. T. (2012). Use of FBG sensors for SHM in aerospace structures. *Photonic Sensors, 2*(3), 203-214.

Kahandawa, G. C., Epaarachchi, J. A., Wang, H., & Canning, J. (2010). *Effects of the self distortions of embedded FBG sensors on spectral response due to torsional and combined loads.* Paper presented at the Proceedings of the 3rd Asia-Pacific Workshop on Structural Health Monitoring (APWSHM 2010).

Kahandawa, G. C., Epaarachchi, J. A., Wang, H., Followell, D., & Birt, P. (2013). Use of fixed wavelength fibre Bragg grating (FBG) filters to capture time domain data from the distorted spectrum of an embedded FBG sensor to estimate strain with an artificial neural network. *Sensors and Actuators A: Physical, 194*, 1-7.

Kardomateas, G. A., Pelegri, A. A., & Malik, B. (1995). Growth of internal delaminations under cyclic compression in composite plates. *Journal of the Mechanics and Physics of Solids, 43*(6), 847-868.

Khalili, P., & Cawley, P. (2016). Excitation of Single-Mode Lamb Waves at High-Frequency-Thickness Products. *IEEE Transactions on Ultrasonics, Ferroelectrics, and Frequency Control, 63*(2), 303-312.

Khan, M. T. I., Sunichi, N., & Hasan, M. (2014). Structural damage localization by linear technique of acoustic emission. *Open Journal of Fluid Dynamics, 4*(05), 425-425.

Kim, S. W., Kim, E. H., Jeong, M. S., & Lee, I. (2015). Damage evaluation and strain monitoring for composite cylinders using tin-coated FBG sensors under low-velocity impacts. *Composites Part B: Engineering, 74*, 13-22.

Kim, Y.-H., Kim, D.-H., Han, J.-H., & Kim, C.-G. (2007). Damage assessment in layered composites using spectral analysis and Lamb wave. *Composites Part B: Engineering, 38*(7), 800-809.

Koyama, K., Hoshikawa, H., & Kojima, G. (2013). Eddy current nondestructive testing for carbon fiber-reinforced composites. *Journal of Pressure Vessel Technology, 135*(4), 041501-041501.

Kundu, T., Das, S., & Jata, K. V. (2007). Point of impact prediction in isotropic and anisotropic plates from the acoustic emission data. *The Journal of the Acoustical Society of America, 122*(4), 2057-2066.

Lam, P.-M., Lau, K.-T., Ling, H.-Y., Su, Z., & Tam, H.-Y. (2009). Acousto-ultrasonic sensing for delaminated GFRP composites using an embedded FBG sensor. *Optics and Lasers in Engineering, 47*(10), 1049-1055.

Lee, B. (2003). Review of the present status of optical fiber sensors. *Optical fiber technology, 9*(2), 57-79.

Lee, F. W., Chai, H. K., & Lim, K. S. (2016). Assessment of Reinforced Concrete Surface Breaking Crack Using Rayleigh Wave Measurement. *Sensors, 16*(3), 337.

Lee, F. W., Lim, K. S., & Chai, H. K. (2016). Determination and extraction of Rayleigh-waves for concrete cracks characterization based on matched filtering of center of energy. *Journal of Sound and Vibration, 363*, 303-315.

Leng, J., & Asundi, A. (2003). Structural Helath Monitoring of Smart Composite Materials by Using EFPI and FBG Sensors. *Sensors and Actuators A: Physical, 103*, 330-340.

Li, J., & Rose, J. L. (2001). Implementing guided wave mode control by use of a phased transducer array. *IEEE Transactions on Ultrasonics, Ferroelectrics, and Frequency Control, 48*(3), 761-768.

Li, Y., Liu, W., Feng, Y., & Zhang, H. (2012). Ultrasonic embedding of nickel-coated fiber Bragg grating in aluminum and associated sensing characteristics. *Optical Fiber Technology, 18*(1), 7-13.

Lin, X., & Yuan, F. G. (2001). Diagnostic Lamb waves in an integrated piezoelectric sensor/actuator plate: analytical and experimental studies. *Smart Materials and Structures, 10*(5), 907.

Ling, H. Y., Lau, K. T., Cheng, L., & Jin, W. (2006). Viability of using an embedded FBG sensor in a composite structure for dynamic strain measurement. *Measurement, 39*(4), 328-334.

Liu, S., Zhang, Y., Zhang, C., & Yang, Q. (2017). *Finite element analysis for the inhibition of electromagnetic acoustic testing (EMAT) Lamb waves multi-modes* (Vol. 1806).

Liu, T., Veidt, M., & Kitipornchai, S. (2002). Single mode Lamb waves in composite laminated plates generated by piezoelectric transducers. *Composite Structures, 58*(3), 381-396.

Lu, S., Jiang, M., Sui, Q., Sai, Y., & Jia, L. (2015). Damage identification system of CFRP using fiber Bragg grating sensors. *Composite Structures, 125*, 400-406.

Majumder, M., Gangopadhyay, T. K., Chakraborty, A. K., Dasgupta, K., & Bhattacharya, D. K. (2008). Fibre Bragg gratings in structural health monitoring - Present status and applications. *Sensors and Actuators A: Physical, 147*(1), 150-164.

Mańka, M., Rosiek, M., Martowicz, A., Stepinski, T., & Uhl, T. (2013). Lamb wave transducers made of piezoelectric macro-fiber composite. *Structural Control and Health Monitoring, 20*(8), 1138-1158.

Marks, R., Clarke, A., Featherston, C., Paget, C., & Pullin, R. (2016). Lamb Wave Interaction with Adhesively Bonded Stiffeners and Disbonds Using 3D Vibrometry. *Applied Sciences, 6*(1), 12.

Martelli, C., Canning, J., Gibson, B., & Huntington, S. (2007). Bend loss in structured optical fibres. *Opt. Express, 15*(26), 17639-17644.

Martínez-Jequier, J., Gallego, A., Suárez, E., Juanes, F. J., & Valea, Á. (2015). Real-time damage mechanisms assessment in CFRP samples via acoustic emission Lamb wave modal analysis. *Composites Part B: Engineering, 68*, 317-326.

Meyendorf, N. G. H., Nagy, P. B., & Rokhlin, S. (2013). *Nondestructive materials characterization: with applications to aerospace materials* (Vol. 67): Springer Science & Business Media.

Michał, M., Mateusz, R., Adam, M., Tadeusz, S., & Tadeusz, U. (2013). Lamb wave transducers made of piezoelectric macro-fiber composite. *Structural Control and Health Monitoring, 20*(8), 1138-1158.

Monkhouse, R. S. C., Wilcox, P. D., & Cawley, P. (1997). Flexible interdigital PVDF transducers for the generation of Lamb waves in structures. *Ultrasonics, 35*(7), 489-498.

Moulin, E., Assaad, J., Delebarre, C., Kaczmarek, H., & Balageas, D. (1997). Piezoelectric transducer embedded in a composite plate: Application to Lamb wave generation. *Journal of Applied Physics, 82*(5), 2049-2055.

Moyo, P., Brownjohn, J. M. W., Suresh, R., & Tjin, S. C. (2005). Development of fiber Bragg grating sensors for monitoring civil infrastructure. *Engineering Structures, 27*(12), 1828-1834.

Murat, B. I. S. (2015). *Propagation and Scattering of Guided Waves in Composite Plates with Defects.* (Doctor of Philosophy), University College London.

Murayama, R., & Mizutani, K. (2002). Conventional electromagnetic acoustic transducer development for optimum Lamb wave modes. *Ultrasonics, 40*(1), 491-495.

Pant, S., Laliberte, J., Martinez, M., Rocha, B., & Ancrum, D. (2015). Effects of composite lamina properties on fundamental Lamb wave mode dispersion characteristics. *Composite Structures, 124*, 236-252.

Park, J. M., Lee, S. I., Kwon, O. Y., Choi, H. S., & Lee, J. H. (2003). Comparison of nondestructive microfailure evaluation of fiber-optic Bragg grating and acoustic emission piezoelectric sensors using fragmentation test. *Composites Part A: Applied Science and Manufacturing, 34*(3), 203-216.

Qingwen, L., Tokunaga, T., & He, Z. (2011). Ultra high resolution large dynamic range optical fiber static strain sensor using Pound Drever Hall technique. *Optics letters, 36*(20), 4044-4046.

Ramlogun, R., Picoux, B., Ulmet, L., & Petit, C. (2005). *An Evaluation of the Application of Infrared Thermography in the Diagnosis of Civil Engineering Structures*.

Ren, L., Jia, Z. G., Li, H. N., & Song, G. (2014). Design and experimental study on FBG hoop-strain sensor in pipeline monitoring. *Optical Fiber Technology, 20*(1), 15-23.

Rezayat, A., Pauw, B. D., Lamberti, A., El-Kafafy, M., Nassiri, V., Ertveldt, J., . . . Guillaume, P. (2016). Reconstruction of impacts on a composite plate using fiber Bragg gratings (FBG) and inverse methods. *Composite Structures, 149*, 1-10.

Rose, J. L. (2014). *Ultrasonic Guided Waves in Solid Media*: Cambridge University Press.

Rose, J. L., Pelts, S. P., & Quarry, M. J. (1997, 5-8 Oct 1997). *A comb transducer for mode control in guided wave NDE.* Paper presented at the 1997 IEEE Ultrasonics Symposium Proceedings. An International Symposium (Cat. No.97CH36118).

Rose, J. L., Philtron, J., Liu, G., Zhu, Y., & Han, M. (2018). A Hybrid Ultrasonic Guided Wave-Fiber Optic System for Flaw Detection in Pipe. *Applied Sciences, 8*(5), 727.

Rosenthal, A., Razansky, D., & Ntziachristos, V. (2011). High-sensitivity compact ultrasonic detector based on a pi-phase-shifted fiber Bragg grating. *Optics letters, 36*(10), 1833-1835.

Royer, D., & Dieulesaint, E. (2000). *Elastic Waves in Solids I* (Morgan, D. P., Trans.): Springer-Verlag Berlin Heidelberg.

Sai, Y., Jiang, M., Sui, Q., Lu, S., & Jia, L. (2015). Composite plate low energy impact localization system based on FBG sensing network and hybrid algorithm. *Optical Fiber Technology, 24*, 84-88.

Santoni, G. B., Yu, L., Xu, B., & Giurgiutiu, V. (2007). Lamb Wave-Mode Tuning of Piezoelectric Wafer Active Sensors for Structural Health Monitoring. *J. Vib. Acoust, 129*(6), 11.

Schmidt, D., Sinapius, M., & Wierach, P. (2013). Design of mode selective actuators for Lamb wave excitation in composite plates. *CEAS Aeronaut J*.

Scholey, J. J., Wilcox, P. D., Wisnom, M. R., & Friswell, M. I. (2010). Quantitative experimental measurements of matrix cracking and delamination using acoustic emission. *Composites Part A: Applied Science and Manufacturing, 41*(5), 612-623.

SeJin Han, B. (2007). *Finite Element Analysis of Lamb Waves Acting Within a Thin Aluminum Plate.* (Master of Science), Air Force Institute of Technology, Air University.

Seth, S. K., Spearing, S. M., & Constantinos, S. (2002). Damage detection in composite materials using Lamb wave methods. *Smart Materials and Structures, 11*(2), 269.

Shrestha, P., Kim, J.-H., Park, Y., & Kim, C.-G. (2015). Impact localization on composite wing using 1D array FBG sensor and RMS/correlation based reference database algorithm. *Composite Structures, 125*, 159-169.

Shrestha, P., Kim, J.-H., Park, Y., & Kim, C.-G. (2016). Impact localization on composite structure using FBG sensors and novel impact localization technique based on error outliers. *Composite Structures, 142*, 263-271.

Shrestha, P., Park, Y., & Kim, C.-G. (2017). Low velocity impact localization on composite wing structure using error outlier based algorithm and FBG sensors. *Composites Part B: Engineering, 116*, 298-312.

Si, L., & Baier, H. (2015). Real-time impact visualization inspection of aerospace composite structures with distributed sensors. *Sensors, 15*(7), 16536-16556.

SongSong, L., Xianjiu, G., & Xiaoming, C. (2010, 24-26 Aug.). *Optimum excitation of the Lamb wave modes in NDE.* Paper presented at the 2010 International Conference on Computer, Mechatronics, Control and Electronic Engineering.

Staszewski, W. J., Mahzan, S., & Traynor, R. (2009). Health monitoring of aerospace composite structures – Active and passive approach. *Composites Science and Technology, 69*(11), 1678-1685.

Su, Z., & Ye, L. (2004). Selective generation of Lamb wave modes and their propagation characteristics in defective composite laminates. *Proceedings of the Institution of*

Mechanical Engineers, Part L: Journal of Materials: Design and Applications, 218(2), 95-110.

Su, Z., Ye, L., & Lu, Y. (2006). Guided Lamb waves for identification of damage in composite structures: A review. *Journal of Sound and Vibration, 295*(3–5), 753-780.

Sun, H. M., Jia, R. S., Du, Q. Q., & Fu, Y. (2016). Cross-correlation analysis and time delay estimation of a homologous micro-seismic signal based on the Hilbert-Huang transform. *Computers & Geosciences, 91*, 98-104.

Tan, K. S., Guo, N., Wong, B. S., & Tui, C. G. (1995). Experimental evaluation of delaminations in composite plates by the use of Lamb waves. *Composites Science and Technology, 53*(1), 77-84.

Tan, K. T., Watanabe, N., & Iwahori, Y. (2011). X-ray radiography and micro-computed tomography examination of damage characteristics in stitched composites subjected to impact loading. *Composites Part B: Engineering, 42*(4), 874-884.

Trojanová, Z., Száraz, Z., Chmelík, F., & Lukáč, P. (2011). Acoustic emission from deformed magnesium alloy based composites. *Materials Science and Engineering: A, 528*(6), 2479-2483.

Tsuda, H. (2006). Ultrasound and damage detection in CFRP using fiber Bragg grating sensors. *Composites science and technology, 66*(5), 676-683.

Tsuda, H., Kumakura, K., & Ogihara, S. (2010). Ultrasonic sensitivity of strain-insensitive fiber Bragg grating sensors and evaluation of ultrasound-induced strain. *Sensors (Basel, Switzerland), 10*(12), 11248-11258.

Vaughan, M. (2017). *The Fabry-Perot Interferometer: History, Theory, Practice and Applications*: CRC Press.

Viktorov, I. A. (1967). *Rayleigh and Lamb Waves*: Springer US.

Vilchis-Rodriguez, D. S., Djurovic, S., Kung, P., Comanici, M. I., Scepanovic, S., Tshiloz, K., & Smith, A. C. (2014). *Wide band fiber Bragg grating accelerometer for rotating AC machinery condition monitoring* (Vol. 9288): SPIE.

Vorathin, E., Hafizi, Z. M., Ghani, S. A. C., & Lim, K. S. (2016). Real-time monitoring system of composite aircraft wings utilizing Fibre Bragg Grating sensor. *IOP Conference Series: Materials Science and Engineering, 152*(1), 012024-012024.

Wada, A., Tanaka, S., & Takahashi, N. (2009). *High-sensitivity vibration sensing using in-fiber Fabry-Perot interferometer with fiber-Bragg-grating reflectors* (Vol. 7503): SPIE.

Wada, A., Tanaka, S., & Takahashi, N. (2012). Optical Fiber Vibration Sensor Using FBG Fabry–Perot Interferometer With Wavelength Scanning and Fourier Analysis. *IEEE Sensors Journal, 12*(1), 225-229.

Wang, X., Lu, Y., & Tang, J. (2008). Damage detection using piezoelectric transducers and the Lamb wave approach: I. System analysis. *Smart Materials and Structures, 17*(2), 025033.

Wang, Y., Bartelt, H., Ecke, W., Willsch, R., Kobelke, J., Kautz, M., . . . Rothhardt, M. (2008). *Fiber Bragg gratings in small-core Ge-doped photonic crystal fibers.* Paper presented at the 2008 1st Asia-Pacific Optical Fiber Sensors Conference.

Weber, R., Hosseini, S. M. H., & Gabbert, U. (2012). Numerical simulation of the guided Lamb wave propagation in particle reinforced composites. *Composite Structures, 94*(10), 3064-3071.

Wenzhu, H., Zhen, T., Zhang, W., Zhang, F., & Li, F. (2015). A high resolution demodulation algorithm for FBG-FP static strain sensors based on the Hilbert transform and cross third order cumulant. *Sensors, 15*(5), 9928.

Wilcox, P., Lowe, M., & Cawley, P. (2001). The effect of dispersion on long-range inspection using ultrasonic guided waves. *NDT & E International, 34*(1), 1-9.

Wild, G., & Hinckley, S. (2007). *Fiber Bragg grating sensors for acoustic emission and transmission detection applied to robotic NDE in structural health monitoring.* Paper presented at the 2007 IEEE Sensors Applications Symposium.

Wild, G., & Hinckley, S. (2008). Acousto-Ultrasonic Optical Fiber Sensors: Overview and State-of-the-Art. *IEEE Sensors Journal, 8*(7), 1184-1193.

Wild, G., Hinckley, S., & Jansz, P. (2008). *A Transmit Reflect Detection System For Fiber Bragg Grating Photonic Sensors.*

Worden, K., Farrar, C., & Manson, G. (2007). *The Fundamental Axioms of Structural Health Monitoring* (Vol. 463).

Worden, K., Farrar, C. R., Manson, G., & Park, G. (2007). The fundamental axioms of structural health monitoring. *Proceedings of the Royal Society A: Mathematical, Physical and Engineering Sciences, 463*(2082), 1639-1664.

Xu, B., & Giurgiutiu, V. (2007). Single Mode Tuning Effects on Lamb Wave Time Reversal with Piezoelectric Wafer Active Sensors for Structural Health Monitoring. *Journal of Nondestructive Evaluation, 26*(2), 123-134.

Yang, B., Xuan, F.-Z., Chen, S., Zhou, S., Gao, Y., & Xiao, B. (2017). Damage localization and identification in WGF/epoxy composite laminates by using Lamb waves: Experiment and simulation. *Composite Structures, 165*, 138-147.

Yang, J., He, J., Guan, X., Wang, D., Chen, H., Zhang, W., & Liu, Y. (2016). A probabilistic crack size quantification method using in-situ Lamb wave test and Bayesian updating. *Mechanical Systems and Signal Processing, 78*, 118-133.

Yoji, O., Keiji, F., Mamoru, S., Hideki, S., & Toshimichi, O. (2010). Delamination detection in composite laminates using dispersion change based on mode conversion of Lamb waves. *Smart Materials and Structures, 19*(11), 115013.

Yu, L., Santoni-Bottai, G., Xu, B., Liu, W., & Giurgiutiu, V. (2008). Piezoelectric wafer active sensors for in situ ultrasonic‐guided wave SHM. *Fatigue & Fracture of Engineering Materials & Structures, 31*(8), 611-628.

Zeng, L., Lin, J., Bao, J., Joseph, R. P., & Huang, L. (2017). Spatial resolution improvement for Lamb wave-based damage detection using frequency dependency compensation. *Journal of Sound and Vibration, 394*, 130-145.

Zhai, G., Jiang, T., Kang, L., & Wang, S. (2010). Minimizing influence of multi-modes and dispersion of electromagnetic ultrasonic lamb waves. *IEEE Transactions on Ultrasonics, Ferroelectrics, and Frequency Control, 57*(12), 2725-2733.

Zhang, H.-Y., & Yu, J.-B. (2011). Piezoelectric transducer parameter selection for exciting a single mode from multiple modes of Lamb waves. *Chinese Physics B, 20*(9), 094301.

Zhang, J., Liu, Y., & Chen, Y. (2002). *X-ray radiography used for non-destructive testing on welds on steel bridge.* Paper presented at the Progress in Safety Science and Technology, Taian, China.

Zhang, Q., Zhu, Y., Luo, X., Liu, G., & Han, M. (2017). Acoustic emission sensor system using a chirped fiber-Bragg-grating Fabry–Perot interferometer and smart feedback control. *Optics Letters, 42*(3), 631-634.

Zhu, Q., Xu, C., & Yang, G. (2017). Experimental research on damage detecting in composite materials with FBG sensors under low frequency cycling. *International Journal of Fatigue, 101, Part 1*, 61-66.

Zohari, M. H., Epaarachchi, J. A., & Lau, K. (2013). *Modal acoustic emission investigation for progressive failure monitoring in thin composite plates under tensile test.* Paper presented at the Key Engineering Materials.

Zohari, M. H., Yusof, M. F., Siregar, J. P., & Lim, K. (2015). The applications of FBG sensor for realtime strain mapping of thin composite plate under point loading. *Journal of Electrical Systems, 2015*, 164-170.